Melanie Ostermann, BSc

Functionalisation and characterisation of nanoparticles for gene therapy

MASTER'S THESIS

to achieve the university degree of

Diplom-Ingenieurin

Master's degree programme: Technical Chemistry

submitted to

Graz University of Technology

Supervisor

Prof. Dr. Emmet Mc Cormack
Institute for Clinical Science, University of Bergen, Norway

and

Ao.Univ.-Prof.i.R. Dr.phil. Volker Ribitsch
Institute for Physical Chemistry, Karl-Franzens-University Graz, Austria

Graz, December 2014

UNIVERSITETET I BERGEN

AFFIDAVIT

I declare that I have authored this thesis independently, that I have not used other than the declared sources/resources, and that I have explicitly indicated all material which has been quoted either literally or by content from the sources used. The text document uploaded to TUGRAZonline is identical to the present master‘s thesis dissertation.

22.12.2014
Date

Melanie Gstrein
Signature

Acknowledgments

This diploma thesis and therefore the end of my studies are under the motto: 'A small step for the world, but a big step for me'. The last 2.5 years were like a rollercoaster: exciting, unexpected and with many ups and downs.

Foremost I would like to express my gratitude to my supervisor Emmet Mc Cormack and co-supervisor Veronika Mamaeva for their support, motivation, help and willingness to share their knowledge. I'm thankful to got the opportunity to work in his group. In addition, I would thank my Austrian supervisor Volker Ribitsch for his help and support.

Besides my supervisors, I would thank the entire group. The past 10 months I have spent with you has been a pleasure. Especially, a thank you to Mireia who spent a multitude of afternoons with me in the laboratory.

Outside our own group, I would like to thank Jessica Rosenholm and all her group members I had contact with during my research stay at Åbo Akademi Univserity, Turku, Finland.

I would also like to thank Lars Herfindal for his help with ζ-potential measurements. A special thank you goes to Mihaela Cimpan and Julia Schölermann for their advice and support during particle dispersion experiments.

I would like to thank Yrr Mørch for her support and help with polymeric nanoparticles.

Furthermore I would like to thank Tina Pavlin for helping with MR imaging *in vivo*.

I would thank Birgit Krenn and Elke Kraker for all their moral support and sharing tears and laughs. I wouldn't have managed it without you.

I would like to thank my family. Without the financial support of my parents I would have never had the chance to study or to go abroad. Thank you for encouraging me and even in the darkest moments dad's words could lift me up: "Los di net untakriagn, des wiart scha wida. Wia san fia di do". No words can express the gratitude I feel towards my parents.

Last but not least, I would like to thank my boyfriend Spiros. The last months were like a never ending nightmare for him. Thank you for supporting me and bringing me back to reality when I lost control.

Zusammenfassung

Zu den konventionellen und auch weitverbreitetsten Krebstherapien gehören die chirurgische Entfernung von Tumoren und die Chemotherapie. Die Chemotherapie basiert auf einem Zellgift, dass das schnelle Wachstum von Zellen verhindert bzw. sie zum Abstreben bringt. Durch die unspezifische Wirkung werden neben Krebszellen auch schnell wachsende Zellen wie Haut-, Haar-, und Blutzellen beeinträchtigt. Chemotherapeutische Medikamente werden oftmals wegen dem hohen interstitiellen Flüssigkeitsdruck in Tumoren nicht aufgenommen und verlieren ihre Wirkung. Grundsätzlich gilt, das eine frühzeitige Erkennung von Krebszellen die Heilungschance erhöht, wobei bisherige Diagnosemethoden beschränkt anwendbar und oftmals unspezifisch sind.

Bei der Weiterentwicklung der Krebsdiagnostik und Krebstherapie spielt besonders in den letzten Jahren die Nanotechnologie eine entscheidende Rolle. Durch die Anwendung von Nanomaterialien ergibt sich die Möglichkeit Limitierungen von herkömmlichen Behandlungs- und Diagnosemethoden zu umgehen und eine frühzeitige Erkennung und gezielte Therapie zu ermöglichen.

Diese Nanomaterialien bzw. Nanopartikel (NPs) können durch selektive Modifizierung an die jeweilige Anwendung angepasst werden. Das große Oberflächen zu Volumen Verhältnis und das veränderbare Porenvolumen ermöglichen eine Beladung von bis zu 50 Gew.%. Diese erhaltenen 'Bomben' können als effiziente und innovative Transportmittel in der Krebsmedizin verwendet werden.

In dieser Arbeit wurden mesoporöse Siliziumdioxid (MSNs) und Polymer-Nanopartikel (PNPs) auf ihr Potential als optische Krebszellendetektoren und als Medikamententransportmittel charakterisiert.

Oberflächenmodifizierte MSNs wurden auf ihre Stabilität als kolloidales System in der Gegenwart von bovinem Serumalbumin (BSA) getestet. Der hydrodynamische Radius wurde mittels dynamischer Lichtstreuung ermittelt und die Oberflächenladung, das ζ-Potential, wurde mit elektrophoretischer Lichtstreuung bestimmt. Oberflächenbeschichtung mit 1,2-Propylenglycol (PEG) führte zu verminderten Wechselwirkungen mit BSA, während Funktionalisierung mit Polyethylenimin zu einer positiven Oberflächenladung und damit zu ungewünschten Wechselwirkungen mit dem Protein führte.

Daraufhin wurde das Bioverhalten von anorganischen und organischen NPs *in vitro* untersucht. Ein Nahinfrarot-Farbstoff in gequenchter Form wurde hierfür an MSNs konjugiert oder in PNPs eingeschlossen. Nitroredcutase-transfizierte Zellen wurden mit diesen NPs inkubiert. Nitroreductase (NTR) reduziert die Nitrogruppen am

Farbstoff zu Hydroxylamin und ein Fluoreszenz Signal wird emittiert. Auf diese Weise kann das Eindringen der NPs in die Zelle mittels Fluoreszenz-Mikroskopie und Durchflusszytometrie detektiert werden. Zu einer passiven Anreicherung von NPs kommt es durch den erhöhten Permeabilitäts- und Retentionseffekt (EPR). Kein Fluoreszenz Signal wurde mit CytoCy5S konjugierten MSNs erhalten, während farbstoffbeladene PNPs ein Signal emittierten. Daraus ist zu schließen, dass die Einkapslung des Farbstoffes in PBCA erfolgreich war. Zusätzlich wurden Maus-fibroblasten mit zwei Cyanin-Farbstoff-modifizierten MSNs inkubiert und zelluläre Aufnahme wurde mittels Fluoreszenz-Mikroskopie bestätigt.

Weiters wurde der Einsatz von Gadolinium (Gd)-beladenen MSNs als innovatives Kontrastmittel *in vivo* für Magnetresonanz-Untersuchungen evaluiert, wobei funktionalisierte MSNs mit einem Standardkontrastmittel (Dotarem®) verglichen wurden. In diesem Pilotprojekt wurden geringe Änderungen des MR Signals erhalten, jedoch müssen weitere Versuche durchgeführt werden, um diese Ergebnisse zu bestätigen.

Diese Arbeit zeigt, dass organische und anorganische NPs ein großes Potential für personalisierte Medizin aufweisen. Entscheidend hierfür sind eine geeignete Oberflächenfunktionalisierung und –ladung, welche für eine optimale Wechselwirkung mit dem biologischen System ausschlaggebend sind.

Abstract

Conventional cancer treatment is often unspecific and limited due to induced systemic toxicities, *i.e.*, killing both healthy and unhealthy tissue. The traditional chemotherapeutics are not always effective due to the inability to reach the tumor as a result of poor pharmacokinetics and a high interstitial fluid pressure. Cancer imaging succumbs to the same limitations; where the imaging probes cannot reach the target tissue, have poor pharmacokinetics, and are often unspecific. The usage of nanotechnology has the potential to improve both cancer diagnosis and treatment offering some exciting possibilities, such as only killing tumor cells whereas healthy tissue remains unaffected. In addition, nanotechnology allows early state detection, which drastically improves the chances for effective therapy. In the past, organic and inorganic nanomaterials, such as nanoparticles, nanovesicles, and micelles have attracted the interest of the research community in chemistry, biology, physics, and medicine for use as novel theranostic agents.

Nanoparticles can be multifunctionalised regarding their desired properties. The large surface area, tunable pore size, high pore volume, and high drug loading capacities of up to 50 wt.%, makes them an ideal therapeutic agent carrier. The main advantage of polymeric nanoparticles when compared to inorganic ones is the biodegradation at a physiological pH. In addition, the biodegradation can be tuned by changing the monomers used.

In this work both mesoporous silica nanoparticles (MSNs) and polymeric nanoparticles (PNPs) were evaluated for their potential use as optical tracking and drug delivery systems.

The surface modified MSNs were assessed for their stability as colloidal systems in a physiological environment with bovine serum albumin as model protein. The hydrodynamic size of nanoparticles was characterised using dynamic light scattering and the ζ-potential was calculated using various electrophoretic mobility tests. Surface coating with an 'inert' material, such as polyethylene glycol (PEG) led to reduced interactions with the serum protein. Functionalisation with polyethylenimine (PEI) resulted in a highly positive surface charge, which led to the negative side-effect of increased protein binding.

Following these results, *in vitro* tests were performed to establish the biobehavior of organic and inorganic nanoparticles within different cell cultures. Previously, our group developed the quenched, near-infrared dye, CytoCy5S. The dye was either conjugated to MSNs or encapsulated in PNPs, and incubated with nitroreductase-transfected cells. Nitroreductase (NTR) unquenches the dye and emitted fluorescence can subsequently be detected. Cellular uptake of nanoparticles can occur due to the

enhanced permeability and retention (EPR) effect and was studied using fluorescence microscopy and flow cytometry. Whilst incubation with the MSNs resulted in no emitted fluorescence, the novel PNPs emitted fluorescence, which peaked after four hours. It was also shown, that the fluorescence intensity depended on the incubation time. In addition, internalisation of MSNs loaded with two different hydrophilic dyes was studied *in vitro* using fluorescence microscopy. The particles were mostly localized in the cytoplasm.

Furthermore, Gd-doped MSNs were evaluated as an innovative MRI contrast agent and compared to the clinically used MRI contrast agent, Dotarem®. In this pilot study minor changes in the MR signal with the used Gd-doped particles were obtained. Nevertheless, more experiments *in vivo* need to be performed to verify these results.

In conclusion, this work shows that both MSNs and PNPs have potential for theranostic applications. Nevertheless, the surface modification plays a crucial role for obtaining stable colloidal systems and avoiding protein adsorption.

Contents

1 Abbreviations

Abbreviation	Meaning
APTES	(3-Aminopropyl)triethoxysilane
BSA	Bovine serum albumin
BW	Body weight
$CHCl_3$	Chloroform
Cop 6, cop 50	Copolymer: Polyethylene glycol - Polyethylenimine
CSC	Cancer stem cell
CT	Computerised tomography
CTAB	Cetyltrimethylammonium bromide
DAPI	2-(4-Amidinophenyl)-1H-indole-6-carboxamidine
DiI	1,1'-Dioctadecyl-3,3,3'3'-tetramethylindocarbocyanine perchlorate
DiO	3,3'-Dioctadecyloxacarbocyanine perchlorate
DIPEA	N,N-diisopropylethylamine
DLS	Dynamic light scattering
DMF	Dimethylformamide
DMSO	Dimethyl sulfoxide
ELS	Electrophorectic light scattering
EMA	European Medicines Agenc
Eppi	Eppendorf® safe-lock tube
EPR	Enhanced permeability and retention
FAD	Flavin adenine dinucleotide
FITC	Fluorescein isothiocyanate
FMN	Flavin mononucleotide
FSC	Forward scatter
GDEPT	Gene-directed enzyme pro-drug therapy
GFP	Green Fluorescent Protein
HCl	Hydrochloric acid
HEPES	4-(2-hydroxyethyl)-1-piperazineethanesulfonic acid
HMDI	Hexamethylene diisocyanate
IC	Internal conversion
ISC	Intersystem crossing
Luc	Firefly luciferase
MDA-MB-231	Triple-negative breast cancer cell line

MFI	Median fluorescence intensity
mPEG	Poly(ethylene glycol) methyl ether
MRI	Magnetic resonance imaging
MSNs	Mesoporous silica nanoparticles
NADH	Nicotinamide adenine dinucleotide
NADPH	Nicotinamide adenine dinucleotide phosphate
$NaHCO_3$	Sodium bicarbonate
NHS	N-hydroxysuccinimide
NIR	Near-infrared
NPs	Nanoparticles
NTR	Nitroreductase
NTR^-	Nitroreductase negative cells
NTR^+	Nitroreductase positive cells
o/n	Over night
PBCA	Poly(butyl cyanoacrylate)
PBS	Phosphate buffered saline
PCA	Poly(cyanoacrylate)
PDI	Polydispersity index
PEG	Polyehtylene glycol
PEI	Polyethylenimine
PET	Positron emission tomography
PFA	Paraformaldehyde
PNPs	Polymeric nanoparticles
RF	Radio frequency
RFU	Relative fluorescence unit
ROI	Region of interest
RT	Room temperature
S_0	Ground state
SI	Signal intensity
S_n	Excited singlet state
SSC	Side scatter
T_1, T_2	Triplet state
TEOS	Tetraethylorthosilicate
Tris-HCl	2-Amino-2-hydroxymethyl-propane-1,3-diol, pH adjusted with 1 M HCl
UV	Ultraviolet light
Vis	Visible light

2 Introduction

According to World Health Organization, there are over 100 different types of cancers which led to a total of 8.2 million deaths in 2012. Cancer is characterised by uncontrollable cell proliferation, distinctive metabolic patterns and the ability to metastasise. Malignancies can affect every tissue and organ in the body [1, 2]. Almost half of all malignant lesions are diagnosed in adults between 50 to 74. Prostate and breast cancers are the most common types found in men and women, respectively [3]. Cancers of the blood and lymph system, such as leukemias and lymphomas, account for the half of all childhood malignancies. On average about 50 % of the patients diagnosed with cancer will die of their disease [4]. To increase the survival rate, new methods of early detection are crucial [5]. However, in the past 30 years the survival rate increased only for certain cancers such as breast and prostate, whereas the mortality rate for pancreatic or lung cancer has remained relatively unchanged since 1980s as shown in Figure 2.1.

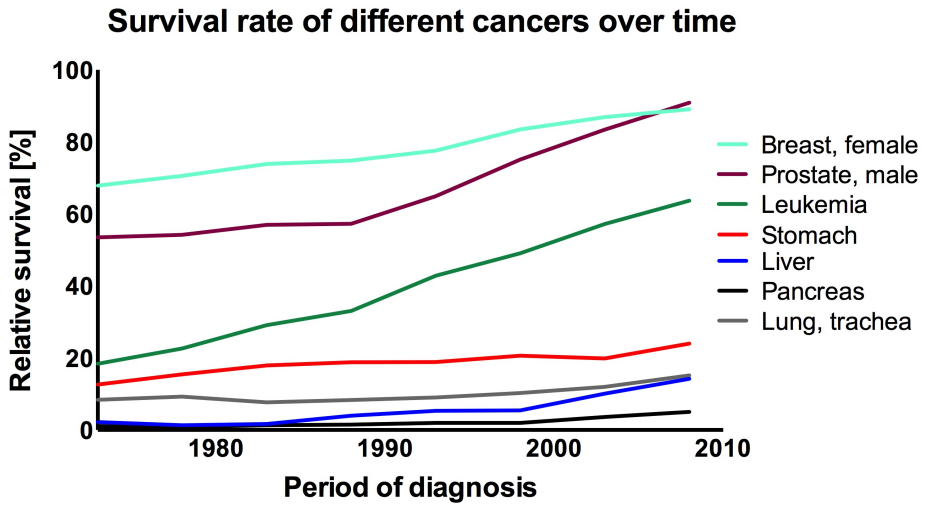

Figure 2.1: Graph depicting the cancer survival as a function of time. The survival rate of breast and prostate cancer, and leukemia has increased, whilst stomach, liver, pancreas, and lung cancer remained relatively unchanged the past 30 years [6].

Conventional cancer treatment strategies includes surgery, chemotherapy and local radiation therapy [7], whereas surgery is a local treatment. Chemotherapeutic drugs are often unspecific and affect beside tumor cells, also rapidly growing cells, such as blood and hair cells [8]. Solid tumors form a barrier due to a high interstitial fluid pressure, resulting in an inefficient chemotherapeutics uptake [9].

New treatment modalities such as nanoparticle carriers, are necessary to overcome limitations of conventional cancer treatment and diagnosis. Novel treatment techniques can contribute to more efficient chemotherapy by lowering dosages, reducing side effects and potentially allowing targeted delivery [10]. Nanotechnology has shown great potential for biomedical applications, especially in theranostics [5, 11]. The term "theranostics" is the combination of diagnostic and therapeutic modalities for personalised medicine [12].

Due to the unique specific properties of nanomaterials *e.g.*, high surface area to volume ratio, small size, and defined shape these materials opened new horizons in drug delivery [13]. They have longer blood circulation times and increased retention in target organs when compared with low molecular weight agents [14]. Currently nanoparticles are successfully used in several biological applications, where the surface charge and functional surface groups play a key role. Surface coating with hydrophilic polymers, such as polyethylene glycol (PEG), increases their half-life and avoids protein adsorption, followed by clearance with reticuloendothelial system [15]. The focus of this research is to functionalise nanoparticles for imaging applications. Results of these research can be used in further functionalisation and modification of nanoparticles for individual approaches.

Inorganic and organic nanoparticles were evaluated and functionalised for theranostic use. The work is structured in three main sections: **1)** Surface functionalisation of mesoporous silica nanoparticles (MSNs), **2)** poly(butyl cyanoacrylate) (PBCA) nanoparticles as optical imaging probes *in vitro*, and **3)** usage of MSN particles as imaging probes *in vitro* and *in vivo*.

Section one deals with the surface modification using different polymers where two methods were used for characterisation: electrophorectic light scattering (ELS) to determine the ζ-potential and dynamic light scattering (DLS) to measure the hydrodynamic particle size. The aim was to achieve a stable colloidal system either due to steric or electrostatic interactions.

In part two, polymeric nanoparticles with a near-infrared (NIR) dye encapsulated were characterised using flow cytometry and fluorescence microscopy *in vitro*. A spectrophotometric enzymatic assay was performed to identify if the dye was encapsulated in the unquenched state and to determine the rate of dye release.

The third part of this research evaluates the potential of functionalised MSN particles as imaging probes. Gadolinium doped MSN particles were used for magnetic resonance imaging (MRI) *in vivo*. Compared to pure gadolinium, Gd^{3+}-doped particles accumulate in tumor tissue due to the enhanced permeability and retention (EPR) effect [16, 17]. Furthermore, fluorescent-labeled MSNs were incubated with triple-negative breast cancer and mouse fibroblast cells. The cellular uptake and the fluorescence intensity were studied using fluorescence microscopy and flow cytometry.

3 Theoretical background

3.1 Cancer formation

The body is made of trillions of living cells. These cells grow, divide and when they become older or damaged, they die and are replaced with new cells. There are several theories of cancer origin. The stem cells theory supports the view of cancer development from a single cancer stem (CSC) cell, which undergoes uncontrollable proliferation and gives rise to other population of cancer stem cells as shown in Figure 3.1. The discovery *e.g.*, of leukemic stem cells prompted further research of this theory into other types of cancer [18].

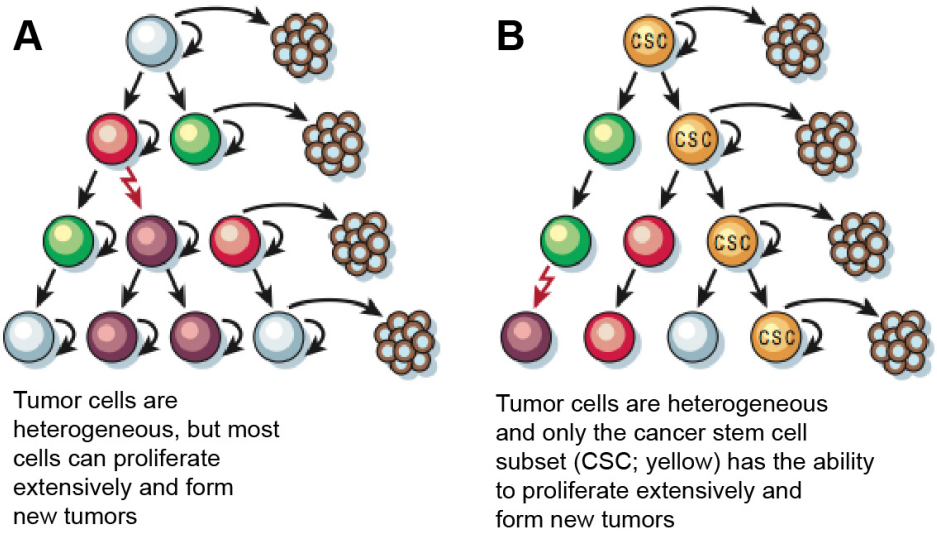

Figure 3.1: Two general models of cancer formation. **A** Different types of cells can proliferate. **B** Only CSCs proliferate and form new tumors [18].

CSCs undergo a sophisticated process called cancerogenesis, or oncogenesis involving formation of blood vessels, modifying stroma, growth and metastases [19]. Not every

cancer results in solid tumors *e.g.*, leukemia [20]. The cancers cells that are produced in the bone marrow, substitute healthy cells and therefore prevent them from fulfilling their functions such as oxygen-transport or resistance against infections [21].

3.2 Cancer detection and treatment

Cancer is mostly diagnosed on the basis of specific symptoms and syndromes followed by biochemical diagnosis of blood and urine. Next are non-invasive imaging methods such as ultrasound, X-rays, MRI, computerised tomography (CT), positron emission tomography (PET) or single photon emission computed tomography and then more invasive procedures such as biopsies *etc.* to confirm diagnosis. Depending on the cancer different methods, such as blood tests, ultrasound, or combination of CT/PET tomography are usually used to follow development. Most of chemotherapeutic drugs affect rapidly proliferating cells such as blood-, hair-, and intestine cells. Side effects are mostly blood toxicity, hair loss and intestinal disorders, other serious side effects are developing from general toxicity of chemotherapeutics on kidneys and liver [8].

Once cancer is diagnosed, a carefully selected treatment is required ranging from surgery, radiation, and chemotherapy, where radiotherapy and surgery are considered as local treatments and target the tumor directly. Chemotherapy on the other hand, is the only method for systematic treatment, which means the anti-cancer drug is distributed through the whole body [7]. Nevertheless, many tumors develop resistance to chemotherapy [22].

The goal in any modality is either to cure or control the disease, or at least to improve the patient quality of life. There are more than 100 different chemotherapeutic drugs available and approved by European Medicines Agency (EMA) such as paclitaxel albumin-stabilised nanoparticles (Abraxane®), docetaxel, paclitaxel, and gemcitabine hydrochloride (Gemzar®) [23]. These drugs differ in their chemical composition, types of cancer they target, and severity of side effects. To reduce side effects, it is sometimes better to use a combination of two or more chemotherapeutic drugs rather than one in high a dose. During treatment, the drug administration follows cyclic regimes, which involves periods of rest, leaving several days or weeks without treatment to give normal cells time to recover [1]. Consequently, toxicity and non-selectivity limits therapeutic efficiency [4, 24]. Among the recent advances in cancer treatment gene-directed enzyme pro-drug therapy (GDEPT) has been recently suggested.

Gene-directed enzyme pro-drug therapy
GDEPT is a two-step process, as shown in Figure 3.2, for solid tumors including a gene expressing an enzyme in cancer cells and a non-toxic pro-drug, which is converted into a cytotoxic compound by the enzyme [25, 26]. Since the gene is only delivered to tumor cells hence expression of the toxin is only carried out in this region, whole-body toxicity is reduced [27]. Important features of this concept are that the enzyme genes are exclusively or in higher abundance expressed in tumor cells compared to healthy tissue and that the catalytic activity of the enzyme is high toward the pro-drug [25].

A large number of suitable enzymes for GDEPT have been developed and undergone Phase II clinical trials, such as nitroreductase (NTR), which converts the pro-drug, CB1954 to a toxic bifunctional deoxyribonucleic acid-crosslinking agent. The toxin inhibits synthesis in this molecules and NTR produces compounds, which lead to controlled cell death [27, 28]. Another promising system is herpes simplex virus thymidine kinase, which converts a non-toxic pro-drug and subsequently kills dividing cells [29].

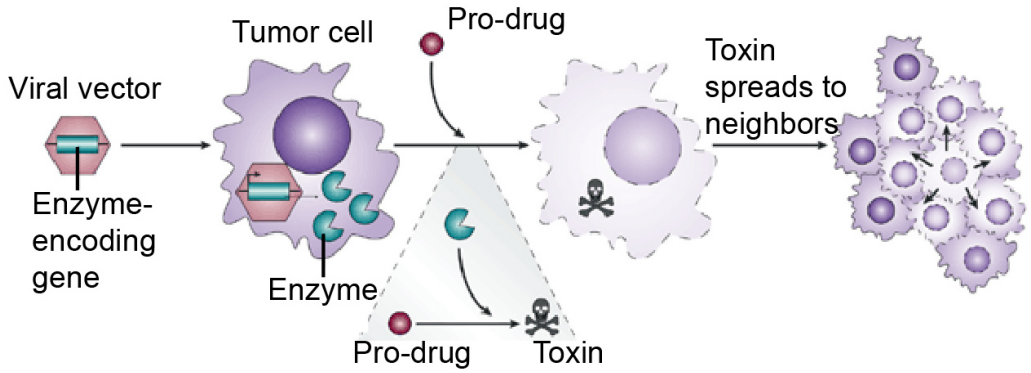

Figure 3.2: Illustration represents the sequence of GEDEPT. In the suicide gene therapy approach a vector delivers a gene containing an enzyme. The aim is to express the enzyme only in tumor cells. Next, a pro-drug is delivered and converted to a cytotoxic metabolite by the enzyme. The toxin spreads due to diffusion to neighbor cells [30].

A limitation of GDEPT is that not all tumor cells can be targeted by gene delivery systems. Therefore it is necessary that the toxin spreads out and destroy neighboring cells. This process is known as the bystander effect and results due to diffusion of the toxic metabolite from cell to cell [31].

GDEPT and imaging
Fluorescent and bioluminescent reporters are important for preclinical imaging methods. However, absorption of light and the autofluorescence of these probes, makes their usage limited [32]. NTR is an attractive enzyme for gene therapy systems as stated

earlier. Beside that, NTR shows a great potential for nanoimaging and can be used as a 'switch' to generate a fluorescent probe from a non-reactive (quenched) compound [33]. This NTR reporter gene method can be used as a novel visualisation method. Previously, our group has developed a NTR/NIR-substrate. The dye, CytoCy5S, is a cell permeable, quenched fluorescent probe, which is converted to a near-infrared fluorescent product by intracellular enzymatic reduction by Escherichia coli nitroreductase (NTR). CytoCy5S combined with NTR can be used for non-invasive monitoring in metastatic breast cancer, lung and leukemia [32].

NTR is a flavoprotein and depends on the tightly bonded cofactors flavin mononucleotide (FMN)- or flavin adenine dinucleotide (FAD). The reduction of nitroaromatic derivates is catalysed by NTR in the presence of nicotinamide adenine dinucleotide (NADH) and nicotinamide adenine dinucleotide phosphate (NADPH) which act as reducing agent as shown in Figure 3.3 [34].

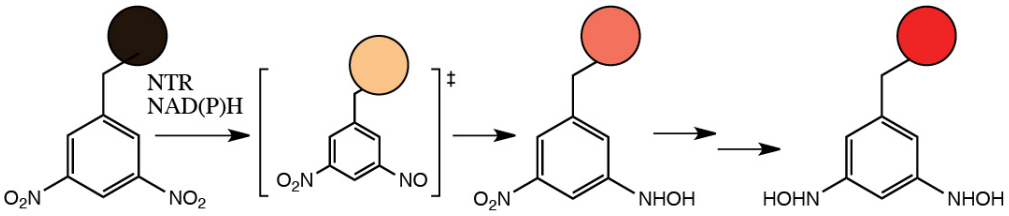

Figure 3.3: Reduction of a nitroaromatic compound in presence of NTR and NAD(P)H. The reduction involves a 2-electron transfer (ping-pong, bi-bi kinetic mechanism) from NAD(P)H to the nitro groups resulting in a hydoxylamine (-NHOH) compound via a nitroso (-NO) intermediate. The FMN (or FAD) group cycles between the oxidized and the reduced states. The second 2-electron transfer takes place faster due to the reactivity of the intermediate [34].

Furthermore, new imaging techniques such as guided imaging radiation therapy have gained attention. Here X-rays and ultrasound are used to direct the radiation during treatment. With this therapy the tumor can be accurately located and exposed, whereupon normal tissue is more protected [35]. Another promising method is drug delivery and gene therapy with the use of ultrasound. Microbubbles loaded with drugs or genes and functionalised with a targeting ligand such as an antibody are injected (intravenously) and the drug or gene is released during ultrasonication treatment. This method ensures local drug delivery and healthy tissue is preserved [36].

In the last years, nanotechnology and targeted approaches have earned more interest due to their unique physical and chemical properties and their interactions with the biological environment. Nanomaterials are used as drug carriers, sensors, and for imaging probes [37]. These little 'bombs' are studied by many research groups and might become the new solution for treatment of a wide range of diseases, such as cancer [38, 39], neurodegenerative diseases [40], and diabetes [41].

3.3 Nanomaterials and Nanomedicine

Formal definitions of nanotechnological devices states that they have components in the size range of 1 to 1 000 nm and that they are man-made [42]. Different research fields, such as chemistry, biology, physics, and medicine are involved. Nanomedcine is the biomedical application of nanomaterials and nanodevices, which are used for therapeutic, imaging, monitoring and diagnostic purposes [11, 17, 37]. These materials can be inorganic or organic like liposomes, polymeric micelles, gold nanoparticles (NPs), and silica NPs. The main features are their individual properties, such as small size, specific shape, long blood circulation time compared to small molecules and large surface to volume ratio, which makes nanomaterials very suitable for introducing new functions [11]. This flexibility includes biomarker-based targeting, cancer-specific delivery [42], and/or contrast agents for diagnostic imaging as shown in Figure 3.4.

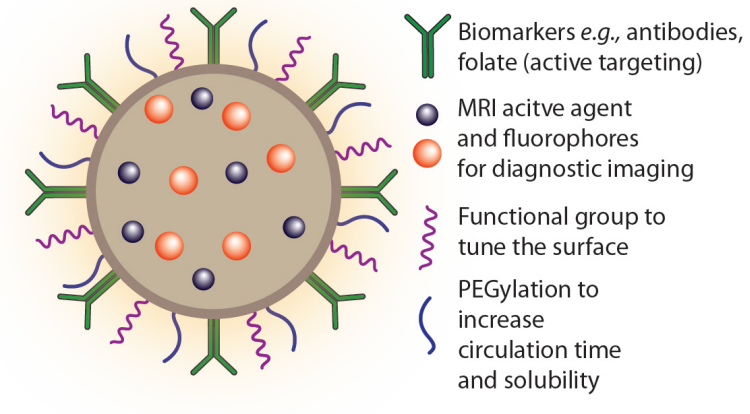

Figure 3.4: A multifunctional nanoparticle. The nanoparticle can be loaded with MRI contrast agents and fluorophores for optical imaging. Active targeting can be achieved by surface fuctionalisation with antibodies, enzymes or receptors *e.g.*, folate. Coating with functional groups such as PEG increases the circulation time and solubility. Due to this coating the particles are 'camouflaged' from the immune system. Functionalisation with polyethylenimine (PEI) leads to a positive surface charge of the particle, which influences the cellular uptake and interaction with the biological environment [43].

As previously mentioned, conventional anticancer chemotherapeutic agents lack tumor selectivity, as shown in Figure 3.5**A**. Modification of the NPs, as shown in Figure 3.4, enhances the intratumoral drug concentration, while limiting the toxicity to healthy tissue. Furthermore, those particles overcome limitations of free anticancer drugs, such as insolubility under aqueous conditions and rapid clearance [5]. Once close to the cell, nanoparticles can interact with the plasma membrane and can be uptaken through a process termed endocytosis [44].

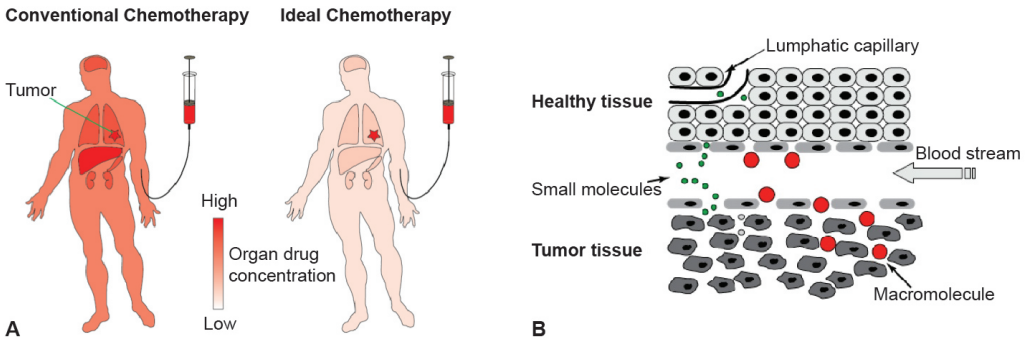

Figure 3.5: Figure showing difference between existing and ideal chemotherapy. **A**: During conventional chemotherapy the whole body is affected compared to ideal therapy, where only the tumor tissue is treated. This can be achieved by using drug loaded and surface modified nanocarriers. **B**: Small molecules can diffuse into the tumor tissue but due to circulation they are rinsed out again. Macromolecules, such as NPs stay in the tissue and selective treatment is possible [45].

Unique properties of these systems allows contrast agents and drugs within nano-sized materials to accumulate in cancer cells due to the EPR effect [16, 17]. Tumor vasculature is usually leaky with fenestrations of 100 nm to 2 µm, compared to healthy tissue, *c.f.*, 3.5**B** [5, 46]. The EPR effect, an important mechanism for passive targeting, enabling macromolecules and nanoparticles to diffuse and accumulate inside tumor tissue [5, 16, 47], whilst healthy tissue stays mostly unaffected [46]. However, tumor vessels are different in their degree of porosity and the EPR effect is therefore not feasible in all tumors [5].

This limitation can be overcome by surface modification and introducing targeting moieties, such as ligands or other biomarkers on the nanoparticle surface. This modification results in ligand-receptor-mediated endocytosis [5, 48]. A biomarker is an indicator of a biological condition [48] *e.g.*, a molecule with biologically important intra- or intercellular functions. Biomarkers include proteins or receptors such as antibodies, which are overexpressed on the surface of the cancer cell. [17]. Surface modification with these molecules leads to binding of the nanoparticle to the overexpressed receptor on tumor cells (active targeting) [5]. The concentrations of the biomarkers are very low, therefore detection of cancer is often difficult. A biosensor transducer is used to detect obtained signals [17].

Nanoparticles cover a broad field of possible materials and can be fabricated from inorganic (gold, iron, silica *etc.*) or organic materials (lipids, proteins, polymers *etc.*) [11, 17]. In the past years many different types of nanoparticles have been developed and improved as shown in Figure 3.6. Each of the carrier systems has its own advantages

and disadvantages.

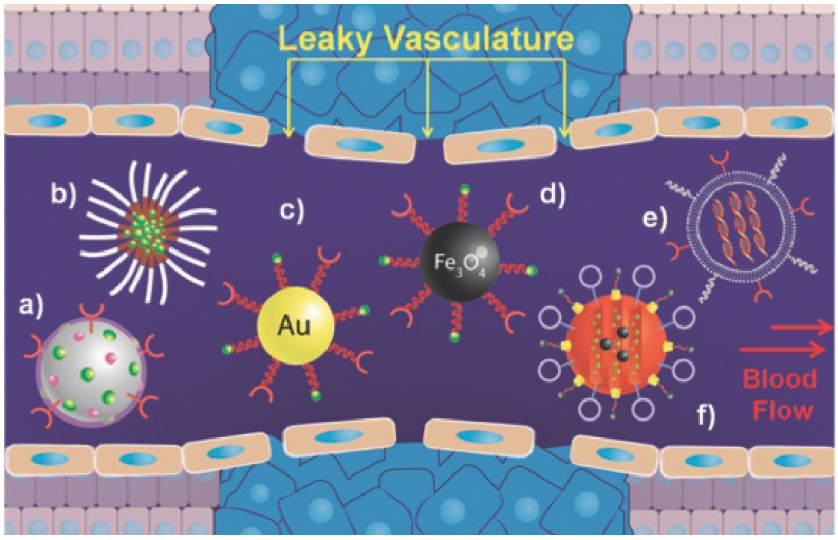

Figure 3.6: Illustration showing inorganic and organic multifunctionalised nanocarriers. Tumor tissue is permeable for various kinds of nanoparticles. In this scheme targeting ligands are indicated by circles and semicircles. The dots represent contrast reagents and loaded cargo on different nanomaterials: **a)** polymeric nanogel, **b)** polymeric micelle, **c)** gold nanoparticle, **d)** iron oxide nanoparticle **e)** siRNA encapuslated in a liposome **f)** multifunctionalised mesoporous silica nanoparticle [46].

The next pages are used to explain different nanomaterials in more detail. The focus will be on polymeric nanomaterials and mesoporous silica nanoparticles, since those have been used in this thesis.

3.3.1 Liposomes

Liposomes were first described in 1965 and soon after proposed as an efficient drug delivery tool [11, 49]. Liposomes are built up from natural phospholipids and are concentric bilayered vesicles [50]. The amphiphilic buidling blocks exhibit a hydrophobic and a hydrophilic part and align in such a way that the hydrophilic head faces the outside of the bilayer with sizes of 100–200 nm [46]. Both hydrophilic and hydrophobic drugs can be encapsulated, which makes liposomes attractive for co-delivery and they are easy to functionalise [11, 50]. Coatings with a polymeric layer, such as PEG increases the blood circulation time up to 80 hours [46]. Many lipidic NPs are in clinical development and several products have gained clinical acceptance and are EMA approved, such as AmBisome® and Doxil® [49].

3.3.2 Metal nanoparticles

Metals, metal oxides and sulfides can be used to produce nanomaterials with tunable pore size, porosity and shape [50]. The most studied metal nanomaterials are iron oxide NPs, gold NPs, and quantumn dots. Iron oxide nanoparticles are biocompatible and biodegradable and are widely used as contrast agents in MR imaging. These iron oxide NPs enhance the contrast, and real-time monitoring is possible [5]. To increase the stability and circulation half-life in biological systems, the particles are coated with PEG, dextran, or and polyethylene oxide [11, 51]. Quantum dots are inorganic luminescent NPs in the size range of a few nanometers (< 10 nm) and are typically used for optical imaging in biological systems. Quantum dots are semiconductors of the elements Cd, Zn, Se, Te, In, P, and As and their absorption and emission spectra can be tuned by varying their size. Adding terminal carboxyl groups (-COOH) on the particle surface increase their hydrophilicity [51]. Gold NPs are excellent candidates for optical imaging, drug carriers, and contrast agents [52]. The particles show higher intensity in absorbing and scattering light compared to organic dyes. Interaction with light results in heat followed by emission of light in the NIR spectrum [51]. Reduced uptake by reticuloendothelial system is achieved by PEGylation of the different nanoparticles, where PEG forms a 'barrier' and prevents attachment of phagocytes [52].

3.3.3 Polymeric nanomaterials

Polymeric micelles

Biocompatible and biodegradable polymeric micelles have gained great attention due to their ability to carry hydrophobic payloads and release them over time [11, 50]. The micelles are characterised by a core-shell structure and are build up from amphiphilic polymer buidling blocks (AB block polymer) [53]. During synthesis amphiphilic molecules self-assemble when the critical micelle concentration (cmc) is reached. Below the cmc, only single chains of the polymer exists. At the cmc, the equilibrium will favor micelles formation and the polymer chains associate. Depending on the solvent *i.e.*, in water the hydrophobic part will form the core to avoid further contact with the aqueous solvent [11, 53, 54].

The morphology of the obtained polymeric structure depends on the packing parameter and the relative volume ratio of the different blocks as shown in Figure 3.7.

The packing parameter can be calculated with following Equation 3.1:

$$P = \frac{V}{l \cdot a_0}, \tag{3.1}$$

where P is the surfactant packing parameter, V is the hydrophobic volume, l the length of the hydrophobic chain and a_0 is the effective area of hydrophilic head group.

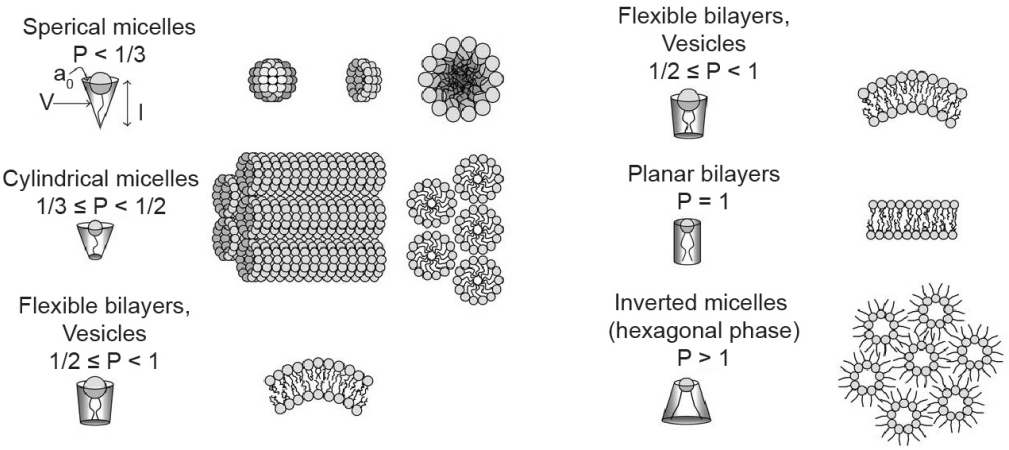

Figure 3.7: Influence of the packing parameter on the shape of the nanomaterial. Energetically favorable aggregates are formed and the packing parameter can be used to suggest the shape. Here, the AB block polymers self-assemble into cylindrical micelles, polymeric membranes, inversed micelles, bilayers and vesicles [55].

The polymeric structures are in a size range of 10–100 nm and PEGylation ensure a longer circulation time [46]. Drugs can be incorporated either by chemical conjugation or by physical procedures (emulsification or dialysis). The drug loaded micelles accumulate to a greater extent in tumor tissue when compared to free drugs due to the EPR effect [55]. Over the past few decades researchers tried to modify and functionalise the surface with PEG and folic acid, peptides and sugars to achieve active targeting [46]. A drawback of this system is the physical instability *in vivo* and the rapid release of the drug [55].

Polymeric nanoparticles

The majority of polymeric NPs are made of poly (D,L-lactide), poly (lactic acid), poly (D,L-glycolide) and poly (cyanoacrylate) PCA or are based on chitosan, gelatin, and other hydrophilic/biodegradable polymers [56]. These nanoparticles can be prepared by salting out, solvent evaporation, and nanoprecipication of preformed polymers or by emulsion and surfactant-free polymerisation emulsions, micro- and mini-emulision using monomers [57].

For the preparation of poly (lactic acid) or poly (D,L-glycolide) nanoparticles, the prepolymer and drug are dissolved in an organic solvent, such as chloroform and emulsified into an aqueous solution yielding a stable oil/water emulsion. Often a surfactant *e.g.*, poly(vinyl)alcohol is added. The organic surfactant is then removed by increasing the temperature/pressure or by continuous stirring.

One method to obtain PCA nanoparticles is via anionic polymerisation of the monomer in an aqueous acidic medium and in the presence of a surfactant. The polymerisation is shown in Figure 3.8 and is carried out under vigorous stirring at room temperature (RT). The particles are purified by ultracentfriguation or re-dispersion in a surfactant-free medium. However, a drawback of these particles is the fast degradation at physiological pH and usage at low pH [56]. To avoid rapid degradation in biological environments, the length of the alkyl group can be varied (*e.g.*, poly(octadecyl cyanoacrylate) and poly(butyl cyanoacrylate) have a longer life-time compared to poly(methyl cyanoacrylate) [58]).

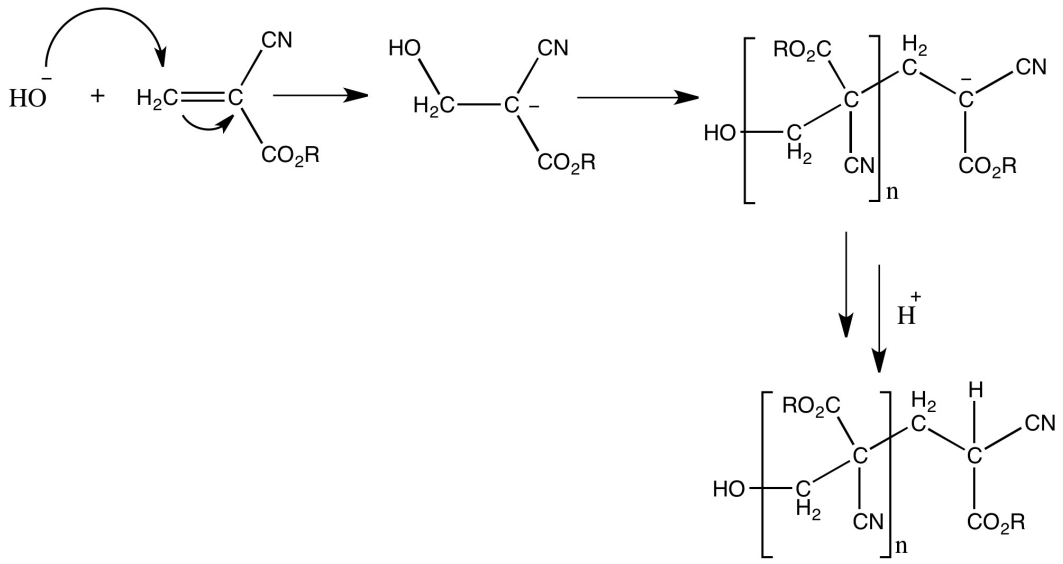

Figure 3.8: Chemical reaction showing polymerisation of PCA. The anionic polymerisation is initiated by nucleophilic attack (*e.g.*, amides, hydroxides, alkoxides *etc.*) on the activated carbon via reactive carbanion as intermediate. Further cyanoacrylate monomers are added forming a linear chain. The reaction is terminated by uptake of a proton [58].

3.3.4 Silica nanoparticles

Ordered mesoporous materials have already been reported in 1992 [59] and according to the International Union of Pure and Applied Chemistry, mesopores are pores in a size

range of 2–50 nm in diameter. The synthesis of Mobil Composition of Matter No 41, the family of mesoporous materials, is based on a cationic surfactant and self-assembling of the silica sources [60]. Mesoporous materials gained substantial interest due to their defined pore size and high surface area, which allows efficient surface modification and ability to carry high payload [43, 50, 61].

Silica is a very versatile material and nano-sized silica particles can be used as a catalyst, in optical devices, for bioimaging, as drug carriers, in theranostic systems, and more [46, 62]. These materials are now one of the most studied nanomaterials in the field of nanomedicine and offer a wide range of functionalities as they can be chemically modified regarding the desired settings and are biocompatible [11, 46].

Preparation
The two most used methods to synthesise silica nanoparticles are the sol-gel process and reverse microemulsion [63]. During reverse micro-emulsion, surfactants form spherical micelles in an organic solvent; *i.e.*, water nanodroplets are obtained [64]. The nanoparticles grow inside the droplets and the particle size can be adjusted by varying the water/oil ratio [63].

The sol-gel process is widely used due to its ability to produce homogeneous and pure products under mild conditions [64]. Mesoporous silica nanoparticles are synthetised by using a cationic surfactant (*e.g.*, cetyltrimethylammonium bromide (CTAB) [46]) as template to obtain MSNs with a high surface area, tunable pore size, and large pore volume [62]. The surfactant self-aggregates into micelles after reaching the cmc. The silica source (*e.g.*, tetraethylorthosilicate, TEOS or (3-Aminopropyl)triethoxysilane, APTES) condenses around the polar part of the surfactant as shown in Figure 3.9**A** and different mesostructures, morphologies, and dimensions can be obtained by controlling the temperature, pH, surfactant ratio, and silica source [43, 46, 62]. The process includes two main reactions **1** hydrolysis and **2** condensation of the silica source as shown in Figure 3.9**B**. This leads first to the formation of a sol, which condense then into a gel phase [46, 64]. The reaction rates (both hydrolysis and condensations) strongly depend on the charge states and can be performed under acidic or basic conditions. The obtained particle size is mostly influenced by the pH and molar ratio of silica source and surfactant [62, 43].

Stöber *et al.* discovered in 1968 [64] an effective method to synthesise spherical monodisperse particles in a size range from 5–2 000 nm using the ammonia-catalysed hydrolysis of TEOS in a water-alcohol solution (Stöber method) [46]. This method is also suitable for non-silca systems. A drawback however is the aggregation of MSNs during synthesis, which in certain cases can be irreversible. Surface protecting agents to stabilize the colloidal system, such as PEG, triethanolamine, and amino acids are used to prevent aggregation.

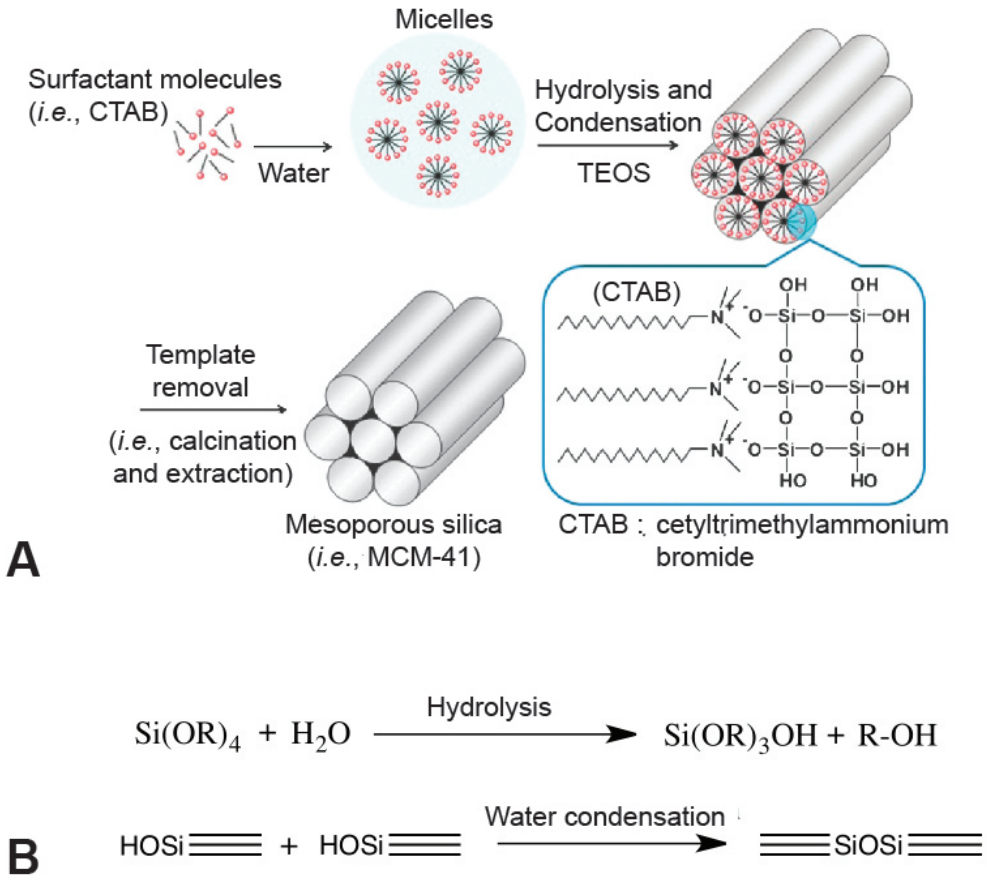

Figure 3.9: A Schematic representation of MSN preparation. The surfactant forms micelles and the silica source condeses around the surfactant. After template removal, mesoporous silica nanoparticles are obtained [65]. **B** Hydrolysis of the silica source leads to silanol groups, which form the silica structure during polymerisation. The first part of the reaction can be acid or base catalyzed [64]. At a low pH (pH 2–7) silica has a negative charge density and assembles with the cationic surfactant due to hydrogen-hydrogen and weak electrostatic interactions. Under basic conditions (pH > 7) only strong electrostatic interaction occur. The condensation reaction reaches a maximum and decrease with a pH > 7.5 due to instability of the silicates [62].

The Stöber process has been modified in the last years by using binary surfactants and dual-mesoporous materials were obtained. The particle size can be tuned using different bases and silica sources and by varying the length of the alkyl chain of the surfactant the pore size of the MSNs can be controlled. When a certain degree of condensation is reached, the surfactant needs to be removed, since common cationic and block copolymers are toxic due to slow degradation [62]. The template can be removed either

by solvent extraction or by calcination. During calcination the materials are typically heated up to at least 550 °C in air for 4 to 8 hours. Acidic ethanol is used during solvent extraction for materials prepared under basic conditions. The process can be enhanced by increasing the temperature to approximately 75 °C [60].

Silica surface chemistry and surface functionalisation
After removal of the surfactant, silanol (Si-OH) and siloxane (Si-O-Si) groups cover the surface and determine the hydrophilic and hydrophobic properties of the NPs. The surface charge of the particles results from protonation and deprotonation of silanol groups. Condensation of the silanol to siloxane groups is achieved by thermal treatment (calcination) and increases the stability of the colloidal system in aqueous solutions. This reaction is reversible and rehydroxylation creates active silanol groups [60]. Independently functionalisation of the silica framework and pores are possible and a huge variety of materials with different electrical, mechanical, optical, magnetic properties, and hydrophobicity are obtained. Active or passive groups can be incorporated by grafting methods or by co-condensation [60, 66].

Co-condensation is used to directly incorporate organic residues in a one step procedure. Mixtures of TEOS and an organosilane such as APTES, octyltriethoxysilane, and allyltrimethoxysilane can be used [66]. Furthermore, it is possible to instantly incorporate a fluorophore such as fluorescein isothiocyanate (FITC) which conjugates with a primary amine of the organosilane. Since the organic moiety is already included in the silica network, a sensitive method such as extraction is necessary to remove the surfactant [60].

During grafting, small molecules attach to the surface of prefabricated silicates as shown in Figure 3.10 [66]. There are two grafting methods: **A** "grafting to" and **B** "grafting from". Both reaction types can be described as covalent irreversible attachments. In **A** functionalised monomers react with compatible surface groups and in **B** the surface is treated to obtain radicals followed by polymerisation [67].

PEI and PEG are commonly used polymers to modify the surface of silica. PEG is used for sterical stabilisation of the NPs, to avoid rapid clearance by the immune system and to prevent protein adsorption [60]. PEI functionalisation leads to cationic nanoparticles which are preferentially uptaken by cells compared to PEGylated and unmodified silica nanoparticles as shown by Xia *et al* [68].

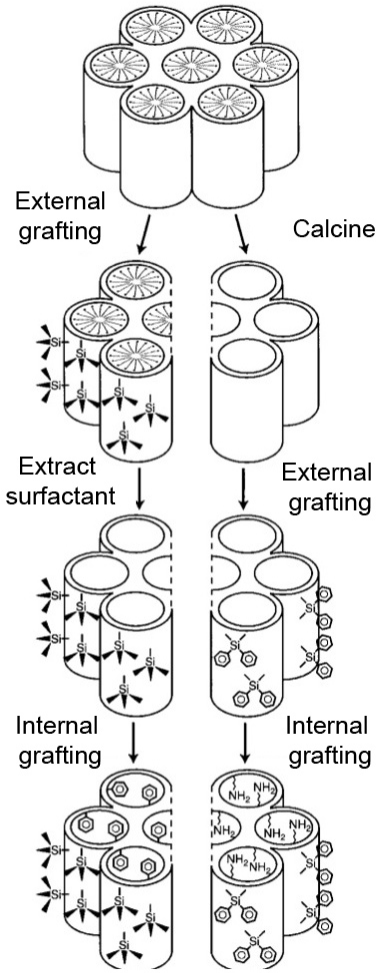

Figure 3.10: Controlled dual modification with grafting. On the left side the surfactant is removed after the external surface modification. On the right side, the pure particle is obtained after calcination and the external and internal surface are modified stepwise [66].

Biodegradation

The degradation of silica depends on the pH, temperature, and surface modification. The network will depolymerise, whereas basic conditions promote the process. The water -OH anions attack silanol groups and support degradation. Furthermore, surface functionalisation *e.g.*, amino groups on the surface, influence the dissolution of the silica. The amino group causes destruction of the Si-O-Si bond by nucleophilic attack in the presence of water as catalyst as shown in Figure 3.11 [60].

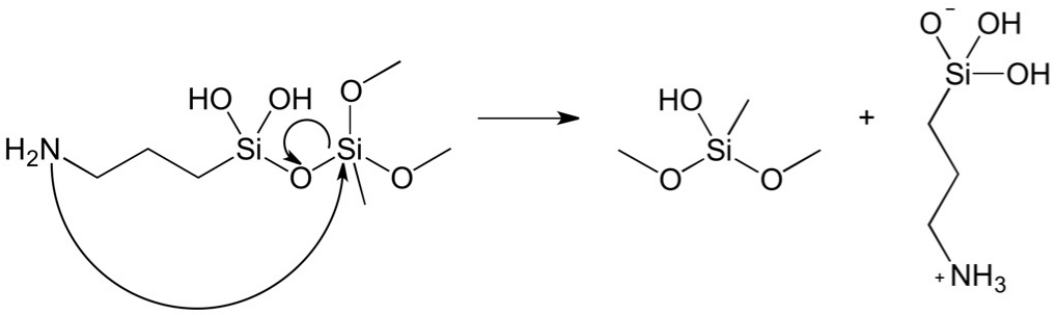

Figure 3.11: Degradation reaction of amino-functionalised MSNs. These particles degrade faster than native silica due to breakage of the bond between the aminoalkylsilane and the silicon atom [69].

3.4 Imaging probes

Nanoparticles, such as quantum dots and labeled organic or inorganic NPs, can be used in diverse imaging techniques. Accumulation of the individual contrast agent is necessary to achieve a good image quality [60]. In this thesis, a NIR dye was encapsulated-in and conjugated-to NPs, and used for optical imaging. Furthermore, gadolinium-doped MSNs were used as contrast agents for MR imaging.

3.4.1 Fluorescently labeled nanoparticles

For *in vivo* applications the optical properties of used probes are critical since light penetrates tissue in a narrow range of spectra [47]. Wavelengths between 650 nm and 950 nm (near-infrared) penetrate tissue more efficient than visible light, since less light is absorbed by hemoglobin or deoxyhemoglobin [70, 71]. Therefore, NIR probes are used as contrast agents for biomedical applications [5, 72].

NTR/CytoCy5S as a near-infrared gene reporter system was used in this work. In section two the near-infrared dye was encapsulated in polymeric micelles during a one step mini-emulsion polymerisation. Encapsulation should protect the dye for degradation.

In part three of this study, the N-hydroxysuccinimide (NHS) ester of CytoCy5S was used to covalently conjugate the dye with MSN particles. During this reaction a primary amine reacts with the NHS-ester activated dye to yield a stable amide bond as shown in Figure 3.12 [73]. This reaction is performed under physiological or weak basic conditions (ideal pH 8.3) for 0.5 to 4 hours [74].

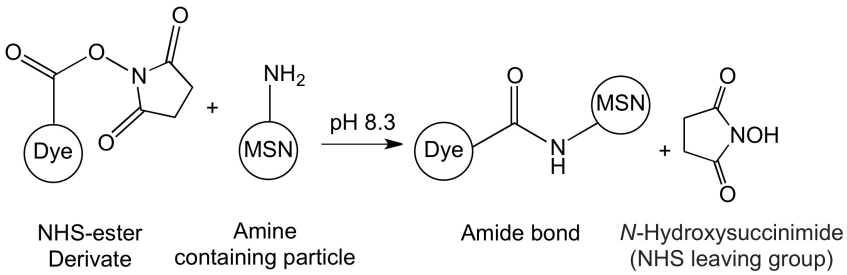

Figure 3.12: Chemical reaction of a NHS ester-activated crosslinkers with a primary amine. Aminofunctionalised MSNs react with the NHS-ester of CytoCy5S yielding a stable amide bond. The reaction takes place at pH 7–9 for 0.5 to 4 hours in 4-(2-hydroxyethyl)-1-piperazineethanesulfonic acid (HEPES) or sodium carbonate/bicarbonate buffers. Buffers with primary amines (*e.g.*, 2-Amino-2-hydroxymethyl-propane-1,3-diol (Tris)) should be avoided, since they react with the NHS-ester.

3.4.2 Contrast agent for MR imaging

Beside encapsulation and conjugation the imaging agent can also be stored in the pores of the MSNs. Due to the high surface area of MSN particles, a large amount of cargo molecules can be loaded [11]. Loading of NPs is mostly performed by soaking the particles in a cargo-solution and the molecules are adsorbed due to hydrogen-hydrogen and electrostatic interactions. The release can then be triggered by a variety of internal and external influences [46].

3.5 Characterisation techniques

Due to a complex structure of these materials the characterisation demands a combination of techniques to obtain all desired information. Gas absorption can be used to determine the pore size and surface area of mesoporous silica NPs. The morphology, size, and structural information of NPs can be studied using a scanning electron microscope and small-angle X-ray scattering [60]. The surface charge of the particles can be measured by electrophorectic light scattering methods. Flow cytometry can be used to measure the relative fluorescence intensity of labeled particles and cellular uptake of NPs can be studied using fluorescence microscopy.

Several techniques to characterise NPs were used during this project. These techniques are described in the following chapter.

4 Technical background

4.1 Electrophoretic Light Scattering

The electrophoretic mobility of particles in a dispersion can be measured using electroporetic light scattering and is converted to the ζ-potential; a physical property which any particle generates in a colloidal system [75]. The ζ-potential represents the electrochemical potential at the solid/liquid interface [76]. Knowledge of the ζ-potential can be used to predict the long-term stability of a colloidal system [75]. It also determines several electrical properties of the dispersion *e.g.*, adsorption of molecules and cellular uptake [77].

In the 1940s the scientists Derjaguin, Verwey, Landau, and Overbeek developed a theory about the stability of colloidal systems [78]. The stability depends on the total potential energy function. This function includes repulsive forces, attractive forces and a net energy. The repulsive force needs to predominate to avoid agglomeration or flocculation. Stable colloidal systems can be obtained by two fundamental mechanisms[75]:

- Steric repulsion via polymer coatings.
- Electrostatic or charge stabilisation due to interactions of the dispersed particle.

Furthermore, the charge affects ions in the suspended media and the amount of adsorbed counterbalanced ions predominates over coion adsorption. This leads to a surrounding electrical double layer [79].

A schematic illustration of the electrical double layer is shown in Figure 4.1, which contains two main layers. In the Stern layer (inner region) the ions are strongly bonded and are immobile when compared to the diffuse layer (outer region), where the ions are loosely associated. Due to electrical forces and random thermal motion, diffusion of ions is possible in this region [80]. When a particle moves *e.g.*, due to gravity or thermal motion the ions at the slipping plane move with it and ions beyond this boundary stay with the bulk solution. The potential at this boundary represents the ζ-potential and gives an indication of the stability of the colloidal system [76]. The electric potential

decreases from the particle surface to the Stern potential and decays exponentially to zero after the slipping plane, [80] as shown in Figure 4.1.

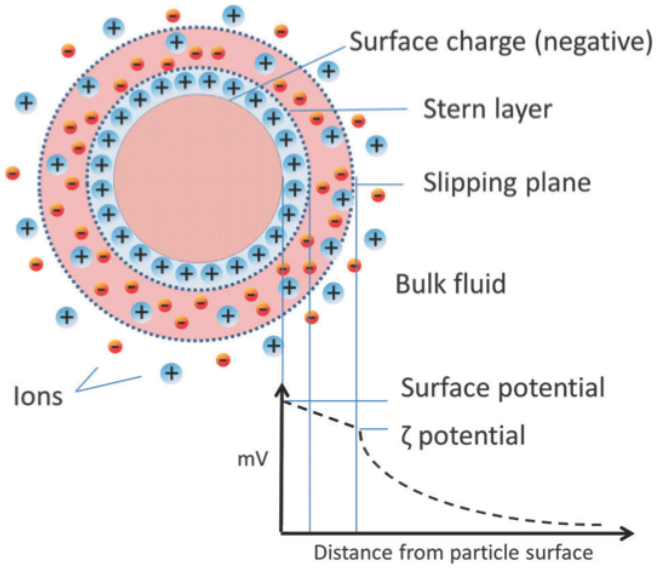

Figure 4.1: Schematic representation of the ζ-potential as a function of the charged particle suspended in aqueous solution. Diffusion of ions is only possible in the diffuse or bulk layer. The ζ-potential is the electrochemical potential at the slipping plane [81].

The particle suspension will be stable if the particles have a highly negative or positive ζ-potential. However, particles with low ζ-potential will flocculate [75]. Particles in a system with a ζ-potential greater than 25 mV or less than - 25 mV [79] stay in their dispersed state, which means the higher the absolute surface charge is, the more stable the system will be.

The ζ-potential can be obtained by measuring the velocity of the particles in an electric field using laser Doppler electrophoresis [82]. During electrophoresis an electric field is applied to the dispersion. The molecules or particles that have a ζ-potential will migrate to the opposite charged electrode of the measurement cell and the electrophoretic mobility is measured [83].

The relationship between the ζ-potential and the electrophoretic mobility (μ_E) is calculated by the Henry equation (Eqn.4.1):

$$\mu_E = \frac{2\epsilon\zeta f(\kappa a)}{3\eta}, \tag{4.1}$$

where ϵ the dielectric constant, $f(\kappa a)$ the Henry's function where a refers to the particle radius, and η is the viscosity[75].

To be able to compare ζ-potential measurements, it is important to specify the dispersion conditions under which the measurement was made, since the pH, temperature, concentration, and salinity influence the surface charge [76].

The basic method for ζ-potential measurements is shown in Figure 4.2. A laser (1) is used as light source to illuminate the particles. The beam splits into a reference and an incident laser beam. The incident laser beam goes through the sample cell (2). Subsequently, scattered light from the sample is detected (3). During an electric field the particles will move and the intensity of scattered light fluctuates with a frequency proportional to the particle velocity. This signal is passed through a digital signal processor (4) and send to a computer (5). An attenuator (6) makes sure that the detected light is in a specific range (necessary for successful measurements). Compensation optics (7) are installed for optimum alignment [75].

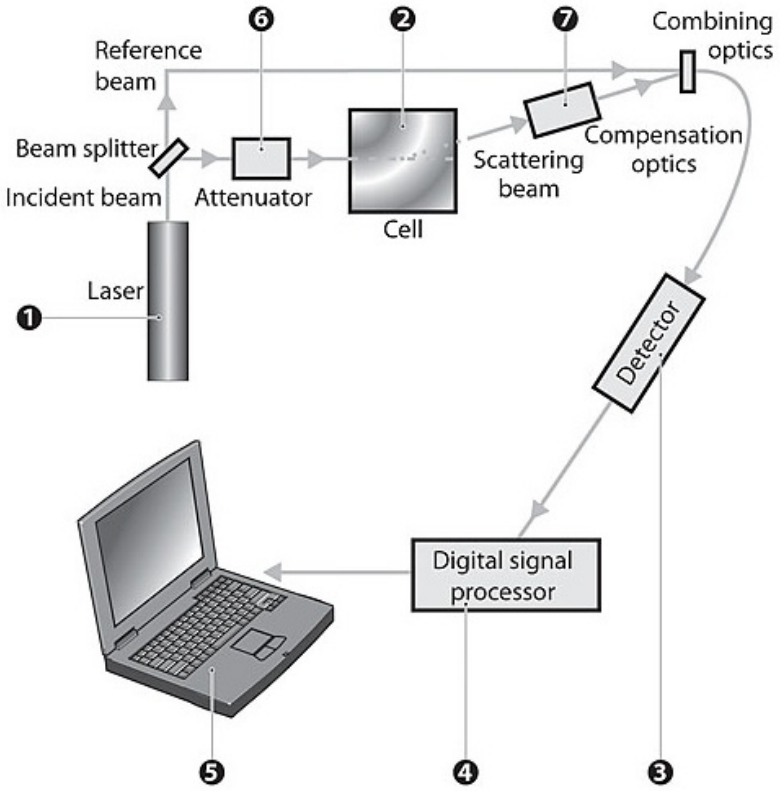

Figure 4.2: Schematic set-up for ζ-potential measurements showing essential components.

4.2 Dynamic Light Scattering

Dynamic light scattering or photon correlation spectroscopy is primarily designed to determine the size of sub-micron sized particles from 5 nm to several microns [84, 85, 86]. During the measurements a monochromatic light beam (*e.g.*, laser) shines onto a dispersion with spherical particles. Due to Brownian motion the local concentration of the particles fluctuates, resulting in inhomogeneity of the scattered light [84]. This change of the incoming light is related to the particle size [87].

The particle diffusion can be described using the Stokes-Einstein equation (Eqn. 4.2):

$$D = \frac{\kappa T}{6\pi\eta R_H}, \tag{4.2}$$

where D is the diffusion coefficient, R_H is the hydrodynamic radius, η is the shear viscosity of the solvent, T is the temperature in Kelvin, and κ is the Boltzmann's constant [86].

The hydrodynamic radius (Stokes' radius) is the hypothetical radius of a hard sphere that would have the same diffusion coefficient as the molecule itself [88, 89]. The Stokes' equation allows one to determine the hydrodynamic radius (R_H) if the sample temperature and solvent viscosity are known [90]. The diffusion coefficient is inversely proportional to the R_H of the particle. Therefore larger particles move or diffuse slower than small ones [86].

The set up of a DLS system is shown in Figure 4.3. As shown in the illustration, the laser passes through an attenuator before it hits the cell. The scattered light is then detected either by a diode array, or by two photomultipliers placed at 90 ° and/or 173 °. The alternating intensity signal is then converted into a voltage signal [87].

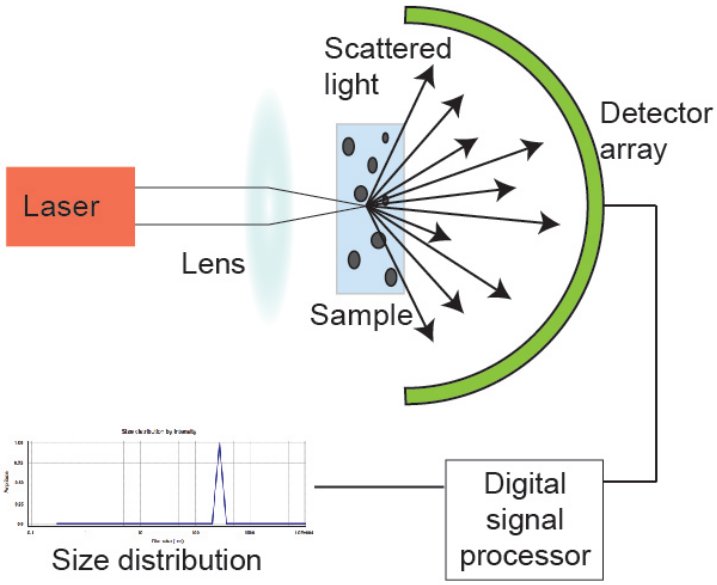

Figure 4.3: Schematic set-up for DLS measurements. The monochromatic laser light is diffracted by particles and scattered light is detected. An attenuator is used to reduce the laser light intensity. The fluctuations in light intensity are then transformed and processed to obtain a size distribution diagram. The amount of light corresponds to the size, molecular weight, and shape of the particle [86].

4.3 Spectroscopic methods

Ultraviolet (UV) and visible (Vis) spectroscopy occupies only a narrow frequency range of the electromagnetic spectra as shown in Figure 4.4. Visible light can be used to excite valence electrons of atoms and molecules [91]. When the electron drops back to the ground state, energy is released. In case of luminescence, the major part of energy is released in form of a photon with a longer wavelength.

Optical spectroscopy is based on the Bohr-Einstein frequency relationship. A molecule absorbs light with a particular frequency and discrete atomic or molecular energy states are allowed. The energy absorbed or emitted during transition and the relation between frequency and wavelength are shown in Equation 4.3:

$$\triangle E = E_2 - E_1 = \mathrm{h} \cdot \nu = \frac{\mathrm{h\,c}}{\lambda}, \tag{4.3}$$

where ν is the frequency, h is the Planck's constant, λ is the wavelength, and c is the

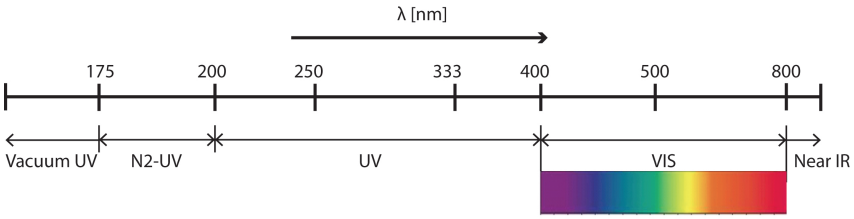

Figure 4.4: Electronmagnetic spectra and their range. Visible spectral region from 400 to 800 nm.

speed of light. Beside this relationship following rules have to be fulfilled [92]:

- Equal multiplicity for both states with $M = 2S + 1$, where S is the angular spin momentum. Changes in spin state of the molecule, such as transitions from singlet to triplet or visa versa are forbidden.
- Frank-Condon Factor $\neq 0$. If the FCF is 0, the wavefunction of the ground vibration state overlap with the wavefunction of the excited state and they cancel each other.
- Forbidden transfer for the same parity (symmetry).

Due to the absorption of a photon, an electron can rise from the ground state (S_0) to an excited state (S_n) [93]. Energetically favored electron promotion will occur from the highest occupied molecular orbital, which is usually the S_0 state to the lowest unoccupied molecular level. The resulting state is the singlet excited state, S_1 [94]. For UV–Vis spectroscopy electron transfers from π to $\pi*$ and n to $\pi*$ (*c.f.*, Figure 4.5) occur in the UV–Vis region and are therefore the most important ones [95]. Absorption bands in the visible region correspond to a needed energy of 40–80 kcal·mol^{-1} for the transition from the ground state to an excited state. Saturated hydrocarbons will not absorb in the visible region, since the lowest excited state is more than 80 kcal·mol^{-1} from the ground state [94].

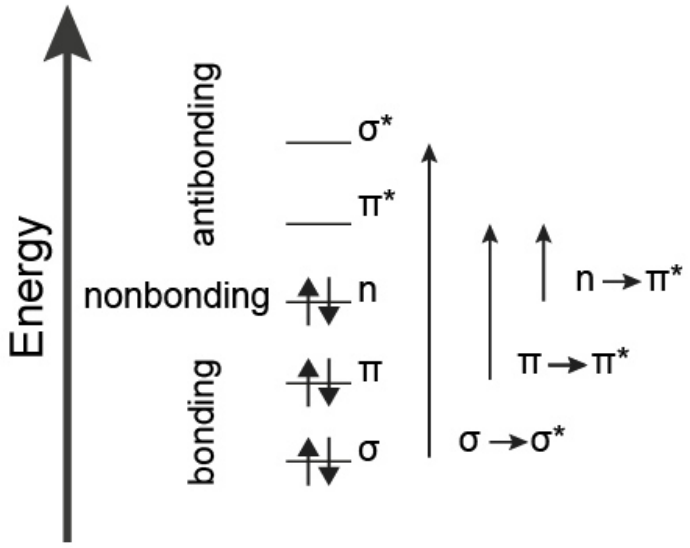

Figure 4.5: Electron transfers in an organic molecule. Transitions from n to $\pi*$: An electron from a non-bonding electron pair moves to an antibonding π* orbital. Transitions from π to $\pi*$ occur when an electron from a bonding π orbital moves to an antibonding $\pi*$ orbital. The σ to $\sigma*$ transitions will not occur, since here a photon with a wavelength, which does not fall in the UV–Vis range is necessary (far-ultraviolet region). The needed energy for electronic transitions is in the order: n to $\pi* < \pi$ to $\pi* < \sigma$ to $\sigma*$.

4.3.1 Fluorescence and phosphorescence

Photoluminescence is the emission of light after optical illumination with a specific wavelength and is subdivided in fluorescence and phosphorescence [96, 97]. Molecules which can absorb and re-emit photons with a specific energy are called fluorophores [94].

On the basics of the above mentioned frequency relationship an energy level diagram is obtained. The levels (S_1, S_2, T_1 *etc.*) correspond to different energies of electrons in singlet and triplet states. Furthermore, these energy levels are subdivided into vibrational and rotational states. With the Jablonski diagram the main basics of photochemistry, including the process of fluorescence and phosphorescence, are described. Beside energy losses due to radiation, energy loss can occur due to non-radiative transitions (*e.g.*, kinetic energy), which are known as internal conversions [91, 98].

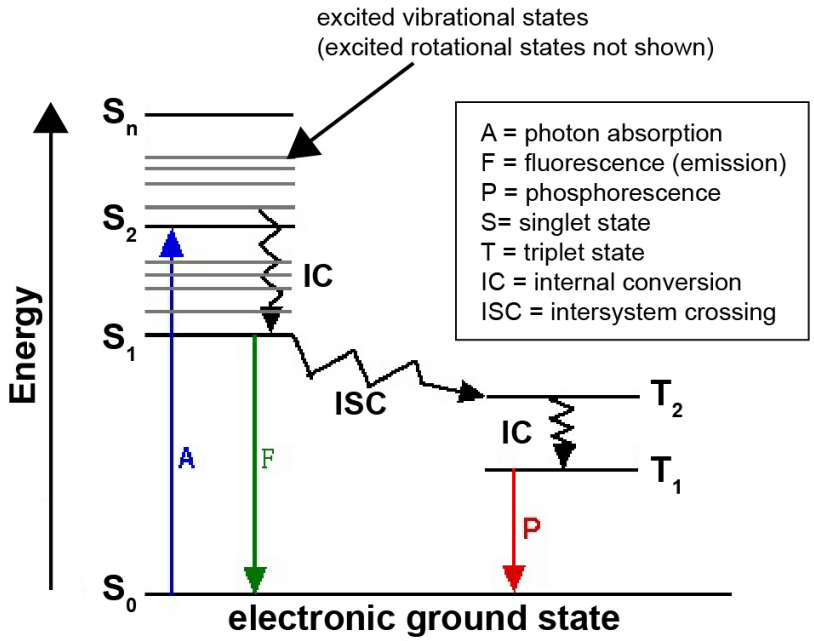

Figure 4.6: The Jablonski diagram showing the allowed transition states S_1, S_2, *etc.*. Furthermore, each state is subdivided in vibration and rotations states (rotations sates are not shown). During absorption (A) an electron is excited in a higher state as indicated with the blue arrow. The transition back to the lowest state of an excited state can occur due to internal conversion (IC, no radiation, black waved arrow). Fluorescence (F, green arrow) occurs always from the lowest excited state. Phosphorescence (P, red arrow) can only occur after intersystem crossing (ISC), which is a spin-forbidden process [99].

Fluorescence occurs in three main steps. In step one, a molecule absorbs light at a particular wavelength and a valance electron is excited from the ground state to a higher level (S_1 or S_2). This process occurs in femtoseconds [100]. In a singlet state all electrons are paired. The spin of the excited electron is also paired with the the ground state. During the excited state (step two) the fluorophore will interact with the chemical environment resulting in energy loss. Also other processes, such as resonance energy transfer [97] and intersystem crossing may occur leading to depopulation in S_1. In step three, a photon with a longer wavelength is emitted due to energy losses during the excited state. Fluorescence occurs within nanoseconds and is always the transition from $S_{1,0}$ to the ground state. Transitions between states different spins are normally forbidden, but they might occur as seen in the Jablonski diagram. Emitted radiation after transition from $T_{1,0}$ to the ground state is called phosphorescence or delayed fluorescence [97, 100]. Due to spin transition (spin of ground state and excited state are parallel) the excitation lifetime is longer and light with a higher wavelength is emitted.

The resulting difference between the absorptions- and emissions peak is known as the Stokes' shift (*c.f.*, Figure 4.7). The wavelength shift can be influenced by different solvents due to interactions and energy transfer [101].

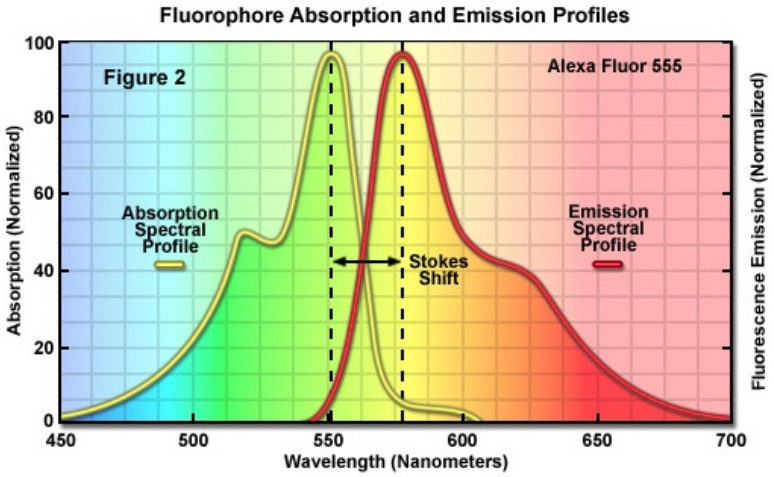

Figure 4.7: Absorption and emission spectra of Alexa Fluor 555. The emission profile mirrors the absorption profile. Due to energy losses the wavelength of the emitted light is higher. The Stokes' shift is the difference between absorptions- and emissions maximum [100].

4.3.2 UV–Vis spectroscopy

The basic principle of the construction of a spectrophotometer is shown in Figure 4.8.

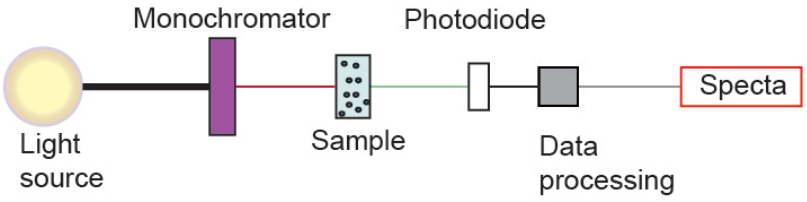

Figure 4.8: Set-up for a UV–Vis spectrophotometer: A tungsten or deuterium arc lamp are used as light source and a monochromator or prism separates different wavelengths. The light is partly absorbed and partly transmitted by the sample. The transmitted light is detected with a photodiode and analysed with a data processing unit.

If light passes through a solution, the intensity is reduced due to absorption. The absorbance can be calculated with following Equation 4.4:

$$Absorbance = -ln(\frac{I}{I_0}), \tag{4.4}$$

where I_0 is the intensity of the monochromatic light entering the sample and I the intensity of the transmitted radiation. Lambert and Bougouer correlated the pathway of a cuvette with the absorption and Beer combined the constant pathway with the concentration of an absorptive substance. The result is well-known as the Lambeert-Beer law (Eqn.4.5):

$$Absorbance = \epsilon \cdot c \cdot d, \tag{4.5}$$

where ϵ is the molar absorptivity coefficient, c the molar concentration, and d the path length. It is the linear relationship which states the that the substrate concentration is directly proportional to the amount that is absorbed [91].

The Lambeert-Beer law however is limited to following chemical and instrumental factors [102]:

- Low substrate concentrations (< 10 mM). UV–Vis absorption is an electronic phenomenon and too high concentrations lead to electrostatic interactions between molecules in close proximity.
- Scattering of light due to agglomeration of particles.
- Non-monochromatic radiation.

4.3.2.1 Spectrophotometeric monitoring

Besides determining the absorbance or emission maxima and the concentration of the analyte in solution, spectrophotometric monitoring can be used to study the kinetics of enzyme-controlled reactions. Rate studies involve measurements of the fall or rise in *e.g.*, emission at a fixed excitation wavelength over time. The obtained measurements give information of concentration changes of the reactant or the product [101].

During this work the quenched dye, CytoCy5S, was reduced by NTR in the presence of the cofactors NADH/NADPH. The nitro groups on CytoCy5S were reduced to hydroxylamines as shown in Figure 4.9. The enzymatic reaction was followed over time and a time-intensity curve was obtained.

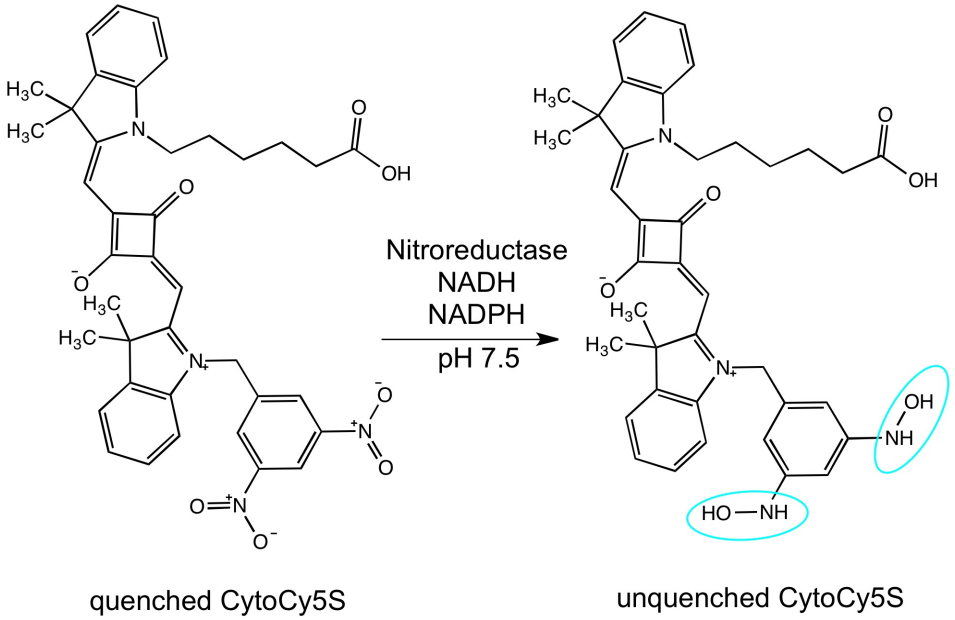

Figure 4.9: Enzymatic reduction of CytoCy5S. The kinetics of the enzyme-controlled reaction of CytoCy5S can be studied using a spectrophotometer. During this assay the fluorescence intensity is measured over a certain time period. Nitroreductase reduces the quenched dye in the presence of the cofactors NADH/NADPH and the fluorescence intensity increases till it reaches a plateau where no unqueched dye is available.

4.3.2.2 Fluorescence microscopy

Fluorescence microscopy is a common technique to study micro- and nanostructure systems, such as livings cells, polymers, or colloids. With a classical fluorescence microscopy the full-field is simultaneously viewed. During this thesis an inverted fluorescence microscope (*c.f.*, Figure 4.10) was used to verify cellular uptake of NPs labeled with a specific fluorophore.

In a conventional fluorescence microscope the sample is illuminated by selectively filtered wavelengths. The wavelength is selected either by a monochromator or by an interference filter. Compared to an optical microscope, a light source which produces UV–Vis light is used (*e.g.*, light emitting diode or xenon lamp). After interactions with the sample the resulting fluorescence signal is analysed [97]. The obtained signal is 3-6 orders of magnitude weaker than the illumination light and is isolated using a second filter. To obtain a satisfied fluorescence signal a combination of filters that coordinate excitation and emission is required [100].

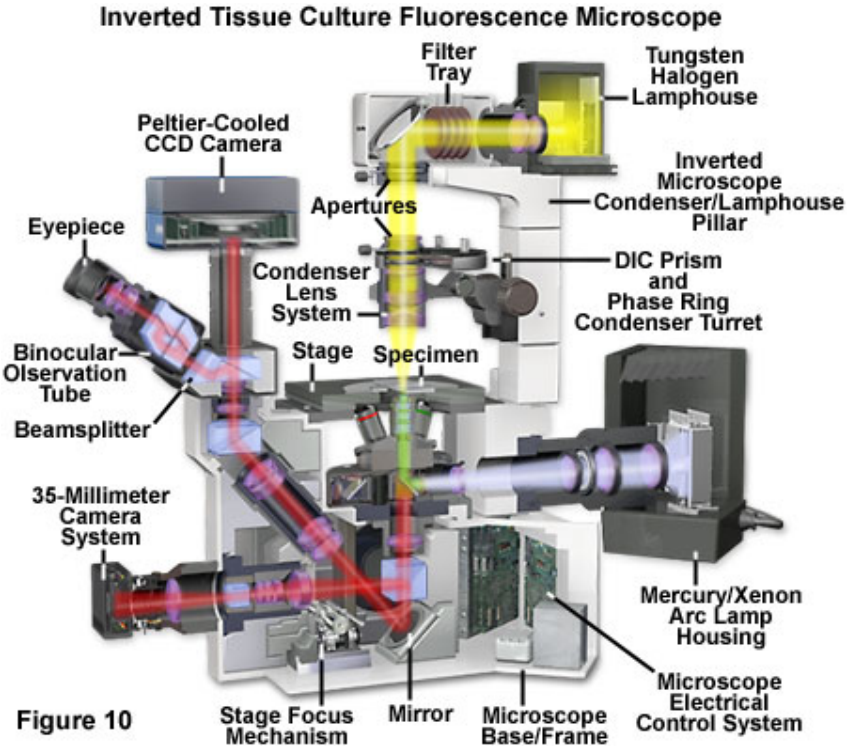

Figure 4.10: Illustration of an inverted fluorescence microscope (Olympus IX70) [103]. Illumination light from a xenon or arc lamp goes through a collector lens, which focus the beam. The light beam passes through a set of filters (interference, excitation *etc.*) and reflects off a dichroic mirror. The reflected light passes the objective and illuminates the sample. The emitted light returns through the objective and a mirror transmits the light to the detector. Additional filters to remove backscattered excitation light are used [97, 103].

4.4 Flow Cytometry

Flow cytometry is based on measuring individual cells or particles as they flow in a fluid stream through a light beam [104]. Each single cell or particle is delivered to a measurement point, where multiple physical characteristics are simultaneously measured [105, 106].

A flow cytometer is build up from three main systems: optics, electronic, and fluidics. When the sample is injected in a flow cytometer, the particles or cells are randomly distributed. Therefore they are ordered via fluidics system and transported to the laser beam as shown in Figure 4.11. The laser light then illuminates the particle. Emitted light can be detected by using separate fluorescence channels [72]. Optical filters and lenses are used to collect the scattered light. The electronic system converts the scattered and

emitted light into electronic pulses [104].

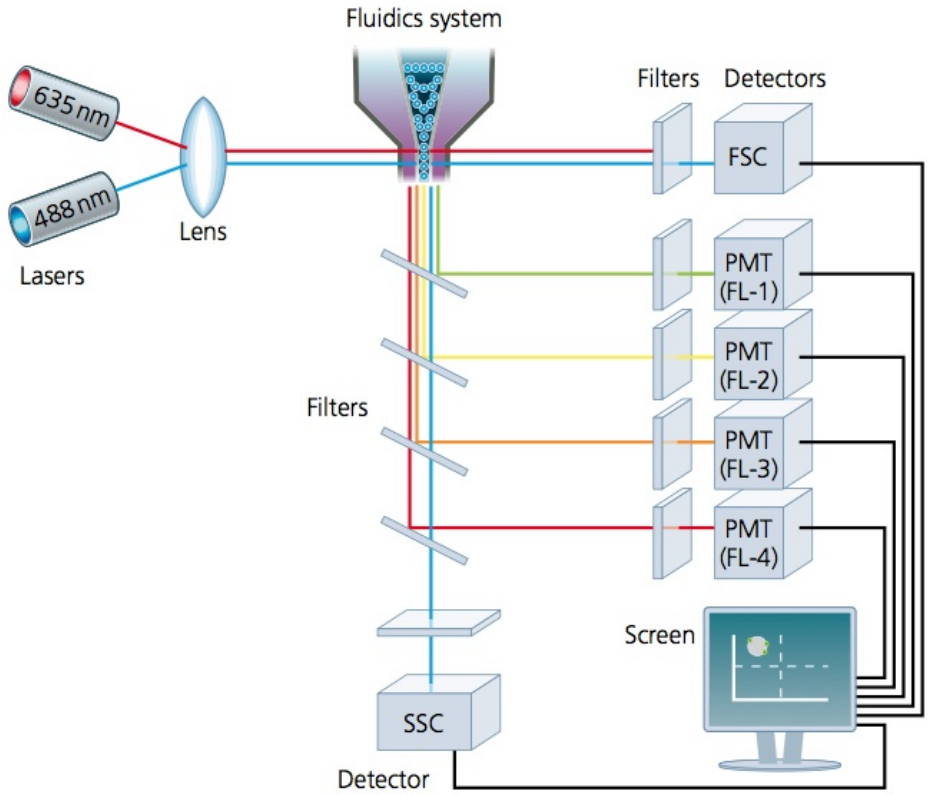

Figure 4.11: Illustration of a flow cytometry setup. The fluidics systems contains two main parts: One channel where the sample is injected and one outer channel with a faster flowing fluid. A single line of particles is obtained due to the drag of the fluid (hydrodynamic focusing). Focused cells or particles passes then the laser light. Emitted and scattered light is detected and gives information about the properties of the cell or particle [72]. CytoCy5S is detected with the photomultiplier FL-4 and the green fluorescence protein and FITC are detected with the photomultiplier FL-1.

Forward scatter (FSC) roughly equates to the cell size and can be used to differentiate between living cells and cellular debris. The side scatter (SSC) provides information on the density and granularity of the particle or cell [72]. Interactions of light with a cell are shown in 4.12.

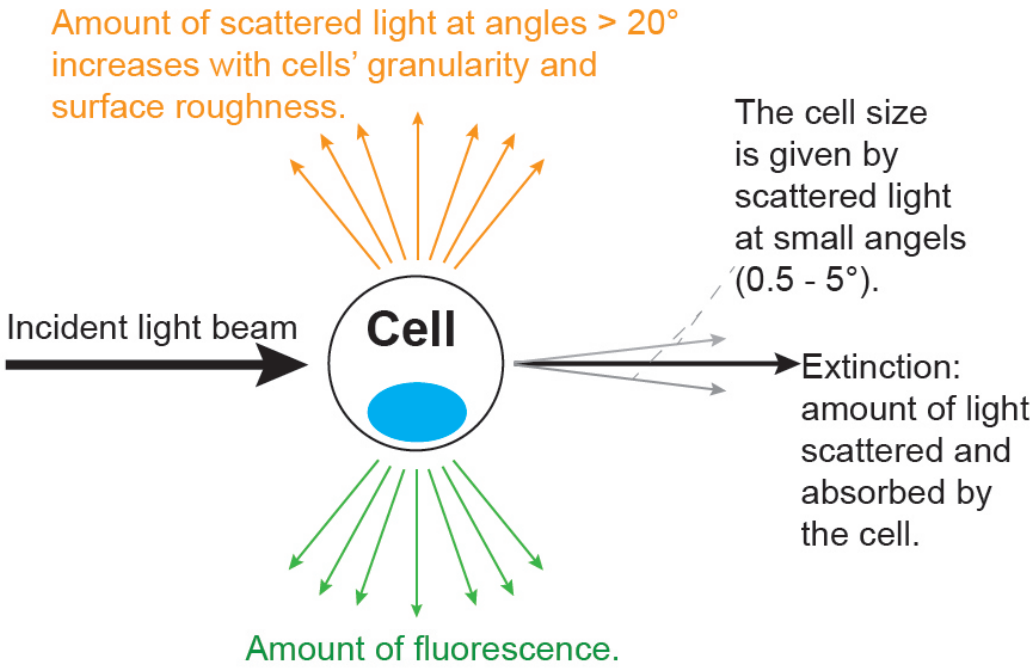

Figure 4.12: Interactions of light with a cell in terms of scattering, absorption, and fluorescence. Depending on the angle of scattered light conclusions regarding cell or particle size and granularity can be made.

4.5 Magnetic resonance imaging

MRI is based on the fundamental principles of nuclear magnetic resonance and is commonly used in clinical studies to obtain images of humans or animals [107]. The body consists of approximately 60 to 75 percent of water [108] and hydrogen atoms are used to obtain an MR signal. Also other atoms with a net nuclear spin as mentioned in Table 4.1 can be used, but ^{1}H is mostly employed since it has a high sensitivity and it occurs in a high abundance in living tissue [109, 110]. MR imaging is non-vasive and is safer compared to other imaging modalities, such as CT and PET, since no radioactive agents or ionisation radiation is used [107, 111].

An MRI system contains a set of main coils, three gradient coils (x, y, and z axis), a shim coil and a transmitter coil. The main magnetic field (B_0 in Tesla) is generated by superconducting magnets, which are cooled with liquid helium. Clinical MR systems operate at 1.5 or 3 T [113]. The animal MR system, which was used during this thesis, operates at 7 T [114]. The higher the magnetic field the better the resolution. The three coils are used to change the magnetic field along B_0 inducing a magnetic gradient, hence

Table 4.1: MR active nuclei: Isotopes, spins, and natural and biological abundance [112] .

Element	Isotope	Spin	Natural abundance [%]	Biological abundance [%]
Hydrogen	^{1}H	$\frac{1}{2}$	99.98	0.63
Carbon	^{13}C	$\frac{1}{2}$	1.11	0.094
Nitrogen	^{15}N	$\frac{1}{2}$	0.37	0.015
Phosphorus	^{31}P	$\frac{1}{2}$	100	0.0024

only a specific region will be resonant at a certain frequency at a time. These coils are to generate and receive emitted radio frequency (RF) signals (MHz range) and to transmit RF energy to the tissue. The shim coils are used to improve inhomogeneities of the magnetic field [115].

By far the most MR studies are performed using the ^{1}H nuclei. The proton (=nucleus) carries a positive electrical charge and has a spin of $\pm \frac{1}{2}$ [112]. Spinning causes a magnetic field in direction of the spin axis and protons align with or against the external applied magnetic field (B_0) as shown in Figure 4.13[116].

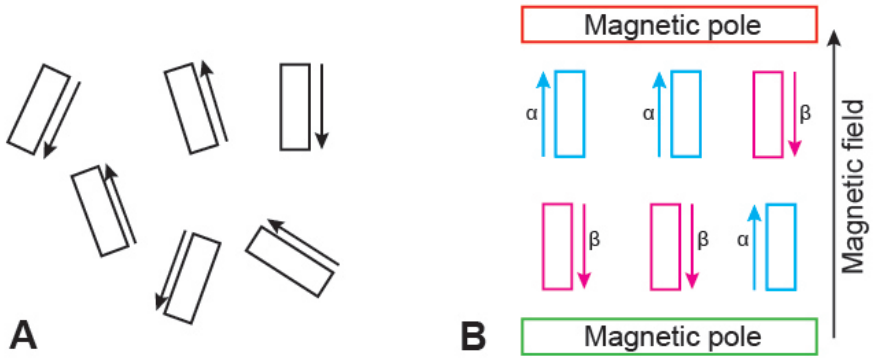

Figure 4.13: Figure representing spin orientation of hydrogen atoms with and without an external magnetic field. **A**: Hydrogen atoms shown as little bar magnets. The arrows indicate the direction of the magnetic field induced by the nuclear spins. **B**: A magnetic field is applied and the nuclei have the tendency to align parallel (α) or anti-parallel (β) to the external field [107].

More protons will align parallel to B_0, since it is the state with the lowest energy and is therefore preferred. The energy difference between the two spins determines the population status and absorption of a photon only takes place if the energy matches [109, 112]. This energy difference can be calculated with:

$$\triangle E = \frac{\gamma \mathrm{h} B_0}{2\pi}, \tag{4.6}$$

where $\triangle E$ is the energy difference between the to spin states, γ is the gyromagnetic ratio, h is the Planck's constant and, B_0 is the external magnetic field [107, 109]. The gyromagnetic constant is nuclei specific and the value for hydrogen is 42.6 MHz/T [115].

The ratio in population of N_α and N_β can be calculated using Boltzmann statistics:

$$\frac{N_\alpha}{N_\beta} = e^{\frac{-\triangle E}{\kappa T}}, \tag{4.7}$$

where N_α is the population in the lower energy level, N_β is the population in the higher energy level, E is the energy difference between the spin states, κ is the Boltzmann's constant, and T is the temperature in Kelvin.

Protons move in a particular way (precession) and the speed is determined by the Larmor equation:

$$\omega_0 = \gamma B_0, \tag{4.8}$$

where ω is the Larmor frequency, γ is the gyromagnetic constant, and B_0 is the external magnetic field.

Precessing protons cancel each other out and result in a sum magnetic field in z-direction as shown in Figure 4.14. During measurements, RF pulses are switched on and off to disturb the protons. Protons absorb RF pulses if the frequency correlates to the precessional frequency of the protons (*c.f.* Equation 4.8) [115]. Following RF excitation, the nuclei realign and emit RF energy [117]. T_1 and T_2 relaxation times define the way that nuclei need to revert back to their resting states and occur independently when the RF pulse is switched off [109]. T_1 relaxation is the spin lattice relaxation time and is the time constant which describes how the magnetisation in z-direction (M_z) returns to its equilibrium value. T_2, also called spin-spin relaxation, describes the relaxation of magnetization in x/y-direction to the equilibrium state. T_2 is always smaller or equal to T_1 [112].

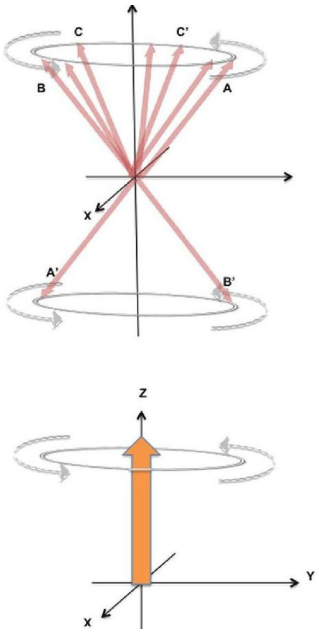

Figure 4.14: Figure showing precessing protons resulting in a sum magnetic field. Protons are shown as red arrows. A and A'(and B and B') are in opposite direction and cancel each other, resulting in a net number of protons parallel to the magnetic field. Also the spins C and C'(both parallel to B_0) start to cancel each other, resulting in a sum magnetic field (orange arrow) [115].

To increase the emitted signal, RF pulses are repeated. The generated signals are collected and the information is stored in a raw data matrix called 'k-space'. To obtain a whole image, the three magnetic coils are used to generate a gradient along the chosen axis. Protons in the gradient field precess at a different Larmor frequency depending on their location. Via Fourier transformation the stored data in k-space is converted [115]. The contrast in MR imaging is obtained due to different relaxation times of protons, which depends on the biological environment *e.g.*, protons in a cancer cell have shorter relaxation times than in healthy cells [107].

5 Materials

5.1 Chemicals

Chemicals were purchased from Sigma Aldrich and were used without further purification. Milli-Q water (18.2 MΩ·cm at 25 °C) was taken from a Q-POD® (Merck KGaA, Darmstadt, Germany).
Dublecco's Modified Eagle's Media (later referred as medium) with 10 % heat-inactivated fetal bovine serum (Thermo Fisher Scientific Inc., USA), 1 % penicillin/streptomycin, and 1 % L-glutamine was used to maintain MDA-MB-231 and mouse fibroblast cells.
2-Amino-2-hydroxymethyl-propane-1,3-diol (Tris Base, ULTROL®, Merck KGaA, Germany) was adjusted using 1 M HCl to pH 7.5 and was used as buffer (later referred as Tris-HCl) for the spectrophotometric enzymatic assay.
N,N-Dimethylformamide (DMF) and sodium bicarbonate ($NaHCO_3$, Biochrom, Merck KGaA, Darmstadt, Germany) were used as solvent/buffer for MSN-CytoCy5S conjugation.
A 25 mM HEPES buffer solution was used as dispersant for nanoparticles. The pH was adjusted with 1 mM KOH to pH 7.2 and the buffer was stored at 4 °C.

5.1.1 Mesoporous silica nanoparticles

The MSNs (*c.f.*, 5.1) (pure, FITC and PEI functionalised and Gd-doped particles) used in this thesis, were provided from Åbo Akademi University, Laboratory for Physical Chemistry, Turku, Finland. The MSN powders were stored at room temperature and dispersed particles were stored in acetone or dimethyl sulfoxide (DMSO) at 4 °C.

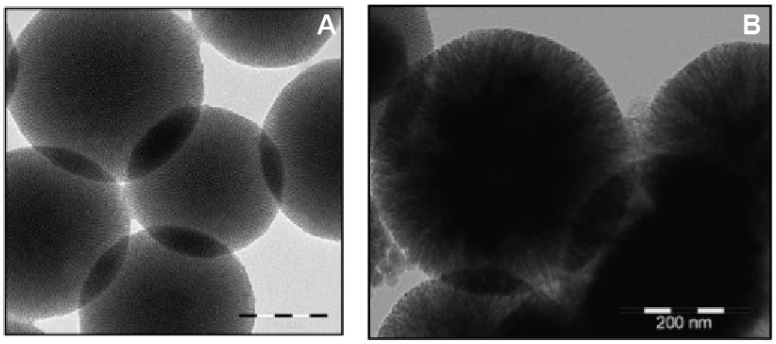

Figure 5.1: Scanning electron microsopy image of MSNs. **A** shows regular MSNs with a pore size of approximately 3 nm and **B** shows expanded particles with an estimated pore size of 6 nm. Image provided by Åbo Akademi University.

5.1.2 Poly (butyl cyanoacrylate) nanoparticles

CytoCy5S loaded and pure PBCA nanoparticles were provided by our collaborators at SINTEF Materials and Chemistry, Department of Synthesis and Properties, Trondheim, Norway. Dispersed particles in acidic water (pH 3) were stored at 4 °C.

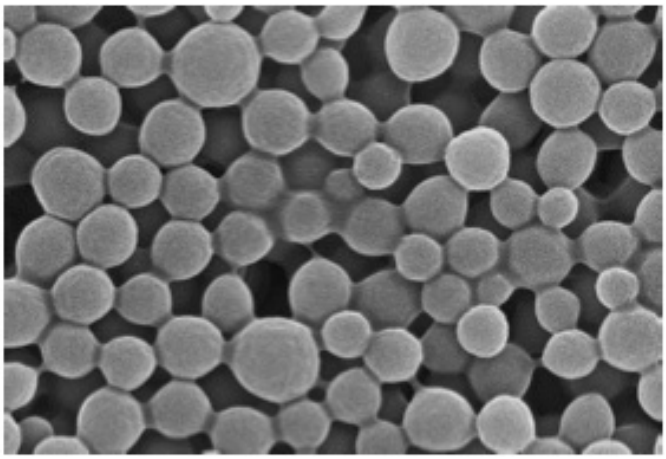

Figure 5.2: TEM picture of PBCA by SINTEF at 60 000 x magnification.

The particles have a theoretical payload of up to 50 wt% and depending on the used monomer and length of the alkyl chain, the degradation time at physiological pH may vary [1].

[1] Personal correspondence with Yrr Mørch, SINTEF Materials and Chemistry, Trondheim, Norway.

5.1.3 CytoCy5S and CytoCy5S N-hydroxysuccinimide ester

The near-infrared dye and NHS-ester were produced at the University of Bergen, Department of Chemistry, Norway. The powders were stored at 4 °C.

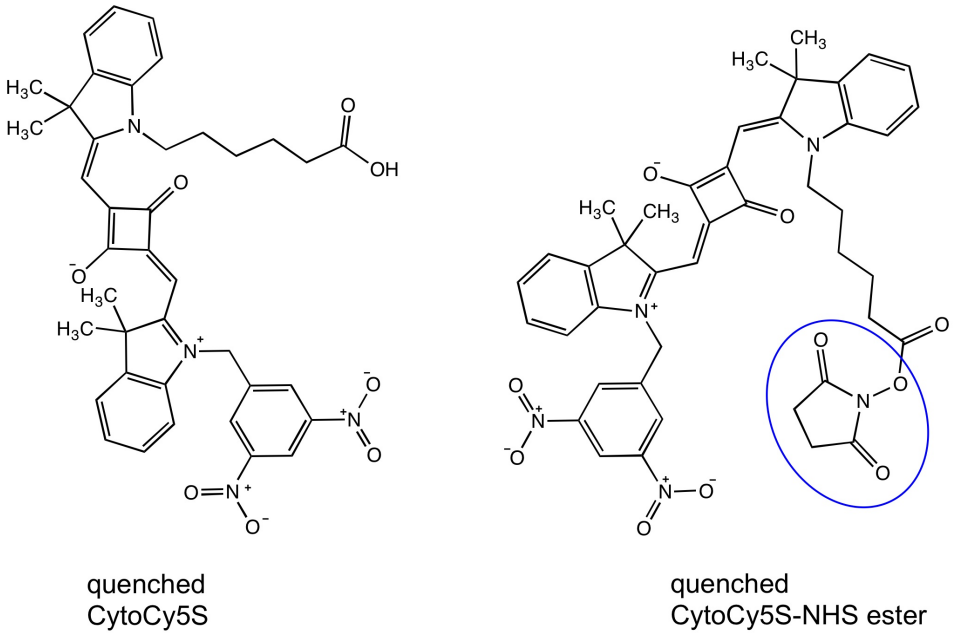

Figure 5.3: Molecular formula of CytoCy5S and the NHS-ester of CytoCy5S.

5.2 Instruments

5.2.1 Dynamic light scattering and electrophoretic light scattering

DLS and ELS measurements were performed using a Zetasiser Nano-S and analysed with Zetasiser version 7.11 software (Malvern Instruments, United Kingdom). Folded capillary cells (DTS1061 and DTS1070, Malvern Instruments, United Kingdom) were used for ζ-potential measurements. DLS measurements were carried out in clear disposable 1-cm polystyrene cuvettes. The settings (later referred as *standard conditions*) for the measurements are summerised in Table 5.1 and 0.5 mg·mL^{-1} particles were measured immediately after ultrasonic treatment. Data analysis was carried out with GraphPad Prism version 6.0c software (GraphPad Software, Inc., La Jolla, USA).

Table 5.1: Settings for DLS and ELS measurements.

Parameter	
Dispertant	Water
Temperature	25 °C
Material	SiO_2
Refractive index R_i	1.2
Absorptioncoefficient R_{abs}	0.001
Detection	Angle 173 °, backscattered

5.2.2 Ultrasonic treatment

Covaris S2
For dispersion, a high intensity acoustic transducer, Covaris S2 (Covaris, Inc., Woburn, Massachusetts, USA) was used. Different cycles as listed in Table 5.2 were applied to achieve a well-dispersed and stable colloidal system.

Table 5.2: Dispersion protocol used on a Covaris S2.

Step	**Cycles**	**Power [W]**
1	100	15
2	1000	15
3	100	75
4	1000	75

5.2.3 Spectrophotometers

NanoDrop 1000 and NanoDrop 2000c
UV–Vis measurements were performed using a NanoDrop 1000 spectrophotometer (Thermo Scientific, USA). The spectrum was measured from 250 to 700 nm. Absorption peaks at $A_{maximum}$ and A_{280} were used to compare the different samples. The sample volume was 2 µL with n=3.

Protein concentration was measured using a NanoDrop 2000c spectrophotometer (Thermo Scientific, USA) using a 1-cm glass cuvettes and Protein A280 method. With this method, purified proteins containing residues or bonds which absorb at 280 nm could be measured and the generation of a standard curve was not required. Amino acids containing aromatic rings are the main reason for absorption at 280 nm.

Synergy H1
Fluorescence and absorbance measurements were carried out with Synergy H1 and Gen5^{TM} acompaging data analysis software (BioTek Instruments, Inc., USA). Area-scans were performed to study the enzyme-catalysed reduction of CytoCy5S. Absorptions spectra were measured from 300 to 700 nm and Table 5.3 summarises the settings used. The sample volume was 100 µL with n=3.

Table 5.3: Settings for measurements with Synergy H1.

Parameter	
Excitation [nm]	631
Emission [nm]	688
Light source	Xenon Flash
Lamp energy	High
Read speed	Normal
Delay [msec]	100
Measurement/Data point	10
Read hight [mm]	7

5.2.4 Fluorescence microscope

Images were taken using a Zeiss Axio Observer Z1 inverted microscope (20× and 63× oil magnification) and analysed in ZEN 2012 (blue edition) version 1.1.0.0 software (Carl Zeiss Microscopy GmbH, Germany). The filters used are summarised in Table 5.4.

Table 5.4: Filter sets for fluorescence microscopy.

Filter Sets	Excitation [nm]	Beam splitter	Emission [nm]
CytoCy5S	BP 560/40	FT 585	BP 630/75
GFP and FITC	BP 450-490	FT 510	BP 515-565
DAPI	G 365	FT 395	BP 445/50

5.2.5 Flow Cytometer

Flow cytometry experiments were performed using a BD Accuri C6 (BD Biosciences, USA) flow cytometer and the data was analysed using FlowJo v10.5 software (Tree Star, Inc., USA). When analysed on the cytometer, 10 000 events per sample were acquired and the fluorescence intensity of CytoCy5S was determined with a 640 nm excitation laser and 675/12.5 band-pass filter. Data analysis of the median fluorescence intensity (MFI) was carried out using GraphPad Prism version 6.0c.

6 Mesoporous silica nanoparticles

6.1 Methods

Methods described in section 6.1.2–6.1.5 were performed at Åbo Akademi Univserity, Laboratory for Physical Chemistry, Finland during an interdisciplinary research stay. Other preparations, functionalisations and characterisations were carried out at the Department of Clinical Science and Building for Basic Biological research at Haukeland University Hospital and at the Department of Physic and Technology, University of Bergen, Norway.

The next pages are used to describe the methods used for particle dispersion, surface-functionalisation and particle characterisation.

6.1.1 Calcination of MSN particles

Mesoporous silica nanoparticles were calcinated at 550 °C in a furnace (Nabertherm GmbH, Lilienthal, Germany). The temperature was slowly increased until 150 °C (5 °C per minute). A temperature of 550 °C was then reached within a few minutes, held for 6 hours, and cooled down to room temperature in two hours.

6.1.2 Particles dispersion

Obtaining a well-dispersed colloidal system is challenging and in many cases particles tend to agglomerate. Therefore different methods have been tested to yield a stable particle dispersion.

Ultrasonic bath
Particles were dispersed in HEPES buffer solution using a ultrasonic-bath for 30 to 45 min. Every 5 to 10 minutes the samples were vortexed to achieve a better dispersed state and to prevent agglomeration of particles.

Sonication treatment with Covaris S2
First, an ultrasonic-bath was used for 25 minutes and the samples were vortexed every 5 to 10 minutes. The last step included sonication treatment with Covaris S2 (*c.f.*, Section 5.2).

6.1.3 Characterisation of nanoparticles

The preparation steps for DLS and ζ-potential measurements for starting and modified particles are shown in Figure 6.1. The procedure shown on the left side, was the same for starting materials and modified particles. Particles were dispersed in HEPES buffer solution at pH 7.2 with a particle concentration of 0.5 mg·mL^{-1} and each dispersion was sampled three times.

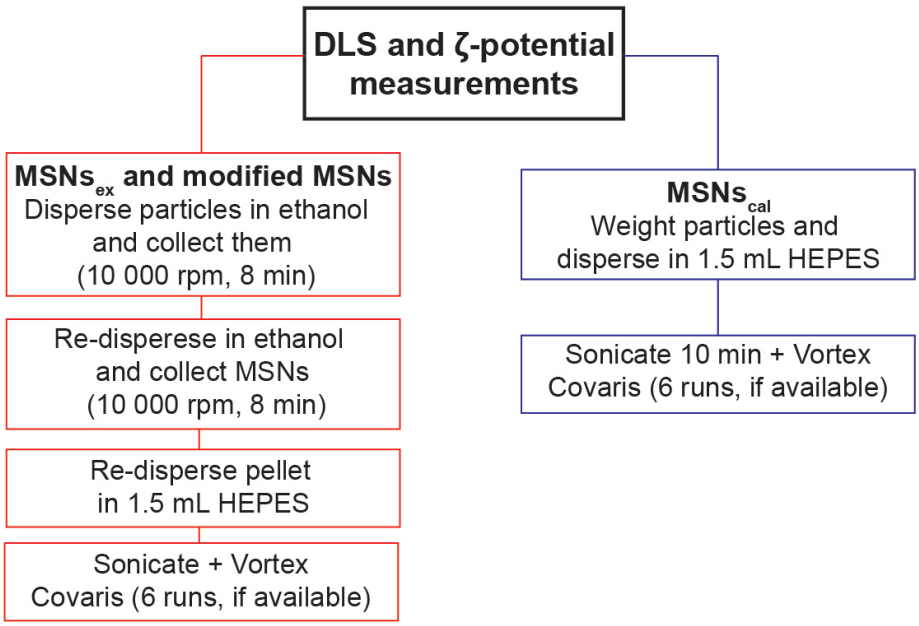

Figure 6.1: Preparation steps for hydrodynamic size and ζ-potential measurements. Particles (0.5 mg·mL^{-1}) were dispersed in 25 mM HEPES buffer solution pH 7.2 and measured with a Zetasizer Nano-S under *standard conditions*.

Figure 6.2 shows an example for obtained DLS and ζ-potential measurements with a ZetaSizer Nano-S. The obtained z-average ('cumulants mean'), is the size which is used for quality control and can only be used to compare results when the same dispersant and technique were used. Furthermore, the polydispersity index (PDI), also known as width parameter, was obtained. Smaller values for the PDI were achieved when particles

had a narrow size distribution. PDIs over 0.7 often indicate a very broad size distribution or particle agglomeration and a different method for particle size characterisation is necessary.

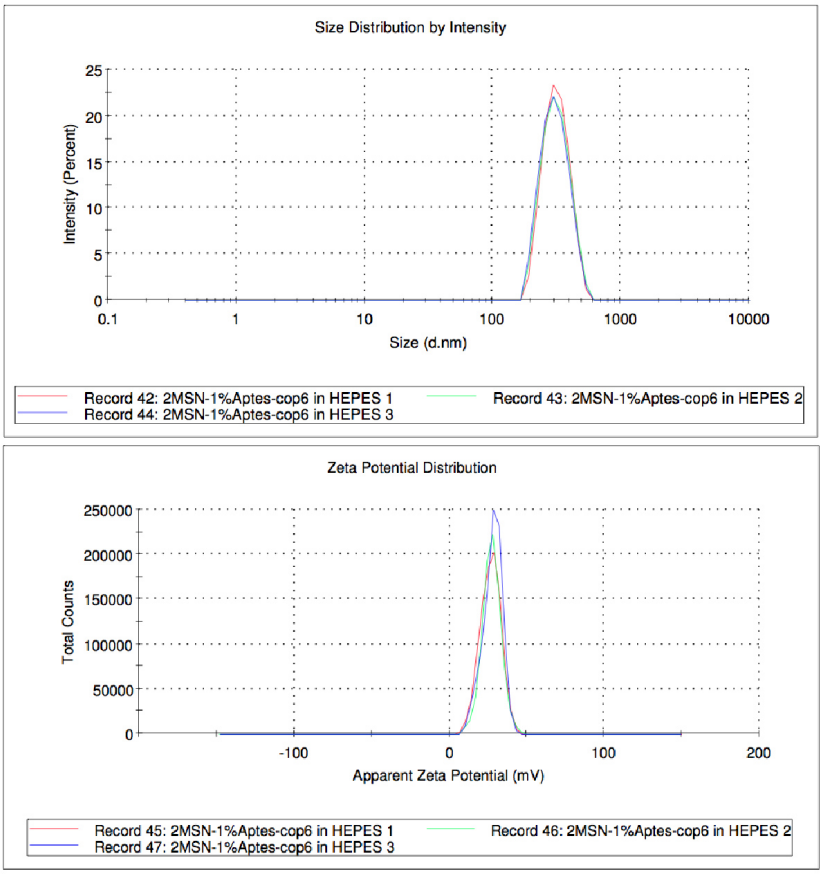

Figure 6.2: Example for three ζ-potential and three hydrodynamic size measurements of MSN 1 % APTES particles modified with a copolymer (cop 6) charachterised with a Zeta-Sizer Nano-S under *standard conditions*. If the system was well-dispersed and stable, the measurements overlapped as shown here.

6.1.4 Surface modification

MSN_{ex} 1 % APTES

For surface functionalisation three different polymers were used: PEI, PEG_{low}-PEI (cop 6), and PEG_{high}-PEI (cop 50).

The synthesis of the copolymer cop 6 is shown Figure 6.3. First, terminal hydroxyl

groups of poly(ethylene glycol) methyl ether (mPEG) were activated with hexamethylene diisocyanate (HMDI). After precipitation with diethyl ether and redissolving in chloroform, polyehtylenime was added, heated to 60 °C, and stirred over night. The numbers, 6 and 50, indicate the grafting ratio, which was used for mPEG-PEI copolymer synthesis. These ratios were based on efficiency studies from Karaman *et al.* [118].

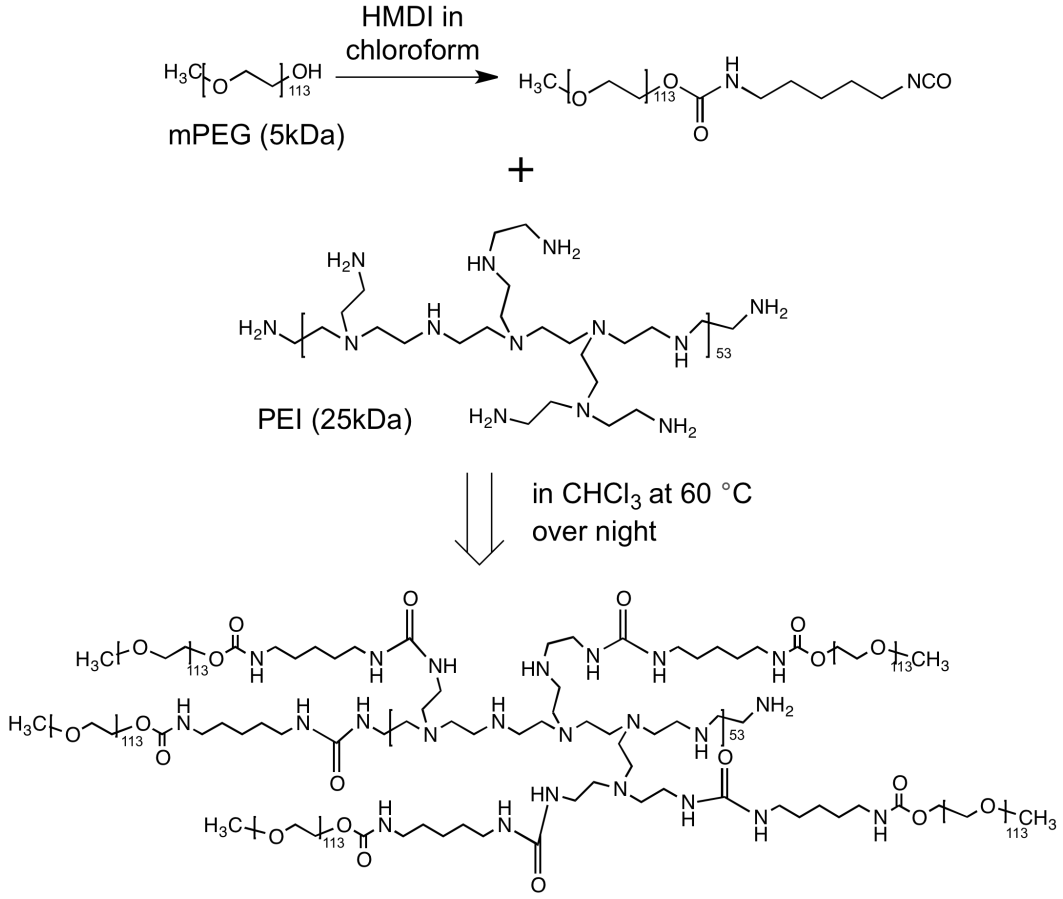

Figure 6.3: Chemical reaction of the copolymer synthesis. First, HMDI was used to activate terminal hydroxyl groups on mPEG. After precipitation and re-dissolving in chloroform ($CHCl_3$), PEI was drop-wise added to the activated mPEG-solution. The graft polymerisation was carried out in chloroform over night under reflux.

First the particle stock dispersion (31.2 mg·mL^{-1} in acetone) was sonicated/vortexed for 20 minutes and the needed amount of particles was transfered into an Eppendorf® safe-lock tube (Eppi). Particle collection was carried out by centrifugation (10 000 rpm for 10 min). Subsequently, the supernatant was removed, the particles were re-dispersed in ethanol, again collected (10 000 rpm for 10 min) and re-dispersed in ethanol before a 100 wt% polymer-ethanol mixture was added. The final concentration of particles and

polymer was 2 mg·mL^{-1} and the reaction was carried out over night at room temperature under stirring. Next, particles were collected (6 000 rmp for 10 min), the surfactant was discharged, and the pellet was re-dispersed in ethanol.

MSN_{ex} 10 % APTES
A) Drying and functionalisation
For graft polymerisation dried particles were necessary. The stock dispersion (39 mg·mL^{-1} in acetone) was first sonicated and vortexed for 15 minutes. The desired amount was transfered into an Eppi, centrifuged (13 000 rpm for 10 min), and the pellet was dried in a vacuum oven for 2 hours.

For PEGylation dried particles (50.3 mg) were weighted in a schlenk flask. $CHCl_3$ (10 mL) was filtered using a 0.2 µm PTFE filter and added to the dispersion. Subsequently the sample was sonicated for 30 minutes. Next, 5 µL N,N-diisopropylethylamine (DIPEA) and 12.5 mL of activated mPEG in $CHCl_3$ (1 mg·mL^{-1}) were added to the particles (mPEG activation via HMDI in ratio of 1 : 1 000). Lastly, the dispersion was sonicated and vortexed for 30 minutes and stirred over night at 60 °C.

For PEI modification 200.8 mg particles were weighted in a schlenk flask, stirred for 3 hours at room temperature, heated for 30 minutes at 75 °C in vacuum and another 30 min in Ar-atmosphere to obtain completely dry particles. Toluene (10 mL) was added via a 0.2 µm PTFE filter and the particles were sonicated for 10 minutes. Again 10 mL toluene was added to achieve a concentration 10 mg·mL^{-1}. Acetic acid (10.4 µL) was added in catalytic amounts and aziridine (104 µL), a 3-membered heterocycle, was used as amino-source. The dispersion was heated up to 75 °C in Ar-atmosphere and the grafting reaction was carried out over night under reflux. The ring-opening polymerisation led to primary amines on the particle surface.

After PEGylation and PEI-functionalisation the particle were separated (6000 rpm for 20 minutes), the supernatant was removed, and the remaining pellet was re-dispersed in ethanol (washing step). Functionalised MSNs were collected at 6000 rpm for 15 minutes, PEGylated particles were re-dispersed in acetone and PEI-functionalised particles in ethanol. The particles were stored at 4 °C.

B) Functionalisation of MSN-PEI particles
MSN-PEI particles were further modified with mPEG, succinic anhydride and acetic anhydride. Again, the particles were sonicated for 15 min. The necessary amount was transfered in Eppis, collected, and vacuum dried. The procedures for the graft polymerisations are shown in Figure 6.4. Next, particles were collected (6000 rpm for 15 min), washed with ethanol, collected (6 000 for 15 min), re-dispered in acetone (10 mg·mL^{-1}), and stored at 4°C.

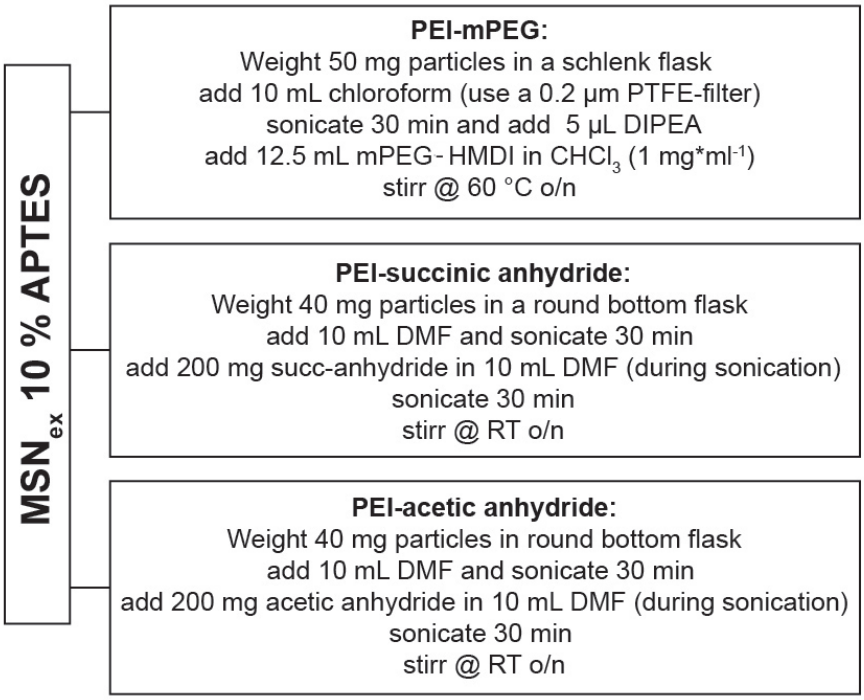

Figure 6.4: Surface functionalisation of MSN_{ex} 10 % APTES-PEI via graft polymerisation. Particles were modified with mPEG, succinic anhydride and acetic anhydride to vary the surface charge of the particle.

6.1.5 Protein adsorption

For protein adsorption different functionalised particles in HEPES with a concentration of 1 mg·mL^{-1} were prepared. The used particles are listed below:

- MSN_{cal}
- MSN_{ex} 1 % APTES
- MSN_{ex} 1 % APTES-PEI
- MSN_{ex} 1 % APTES-cop 6
- MSN_{ex} 1 % APTES-cop 50
- MSN_{ex} 10 % APTES
- MSN_{ex} 10 % APTES-PEI
- MSN_{ex} 10 % APTES-mPEG
- MSN_{ex} 10 % APTES-PEI-succinic anhydride
- MSN_{ex} 10 % APTES-PEI-acetic anhydride
- MSN_{ex} 10 % APTES-PEI-mPEG

A 400 $\mu g \cdot mL^{-1}$-protein solution in HEPES was prepared. The final concentration in each Eppi was 0.5 $mg \cdot mL^{-1}$ particles and 100 respectively 200 $\mu g \cdot mL^{-1}$ bovine serum albumin (BSA). BSA was used as serum-supplement to mimic physiological environment, since it is the major compound of fetal calf serum. The particle-protein suspensions were incubated for 3, 6 and 24 hours in a water bath at 37 °C allowing protein adsorption.

Particles were collected (10 000 rpm for 10 minutes) and the supernatant was measured using a NanoDrop 2000c to determine BSA concentration. HEPES buffer solution was used as blank sample. The amount of adsorbed protein was obtained by comparison with samples containing the respective amount of BSA in HEPES buffer solution.

The obtained pellet was re-dispersed in HEPES (0.5 $mg \cdot mL^{-1}$) and the hydrodynamic size and ζ-potential were measured using a ZetaSizer Nano-S under *standard conditions*.

6.2 Results and discussion

6.2.1 Characterisation of MSNs after calcination

The Z-average (diameter of the particle) and ζ-potential values are listed in Table 6.1. Before calcination the ζ-potential varied and showed unexpected positive values, which may be due to impurities or surfactant residues. Distorted values for the hydrodynamic size (> 2 µm) were obtained. After calicanation, the hydrodynamic size and ζ-potential showed the predicted values for pure silica particles.

Table 6.1: Hydrodynamic size and ζ-potential of MSNs before and after calcination measured with a ZetaSizer Nano-S under *standard conditions*.

Sample	Z-average [d,nm]	PDI	ζ-potential [mV]
MSN_{cal} in HEPES	3600.7 ± 563.2	0.47 ± 0.17	+18.1 ± 1.8
$MSN_{cal_{new}}$ in HEPES	303.8 ± 2.1	0.08 ± 0.02	- 32.9 ± 1.1

Silanol groups were deprotonated at pH 7.2 and the electrostatic repulsion between the negative charges led to a stable colloidal system.

6.2.2 DLS and ζ-potential measurements of MSNs and functionalised particles

After calcination the pure silica particles (MSN_{cal}) remained and the hydrodynamic radius was smaller compared to solvent extracted particles that contained amino groups

(-NH_2) on the particle surface (MSN_{ex}). Pure silica particles had only hydroxyl (–OH) groups on their surface, which led to a higher negative ζ-potential as shown in Table 6.2.

Table 6.2: Hydrodynamic size and ζ-potential of the starting materials measured under *standard conditions*.

Sample	Z-average [d,nm]	PDI	ζ-potential [mV]
MSN_{ex} 1% APTES	703.9 ± 17.6	0.29 ± 0.02	- 11.3 ± 0.5
MSN_{cal}	321.8 ± 6.5	0.34 ± 0.02	- 44.3 ± 0.9

Due to different surface modification a broad variation in ζ-potential was obtained (*c.f.*, Table 6.3). The PEI-layer contains many amino groups, which resulted in a high positive surface charge compared to non-coated particles. Cop 6 coated particles exhibited a higher ζ-potential due to an increased amount of PEI in the copolymer compared to cop 50, where the amount of PEG and therefore the total number of hydroxyl groups predominates. A higher APTES-content resulted in a more positive surface charge compared to MSNs with 1 % APTES. Again, this can be explained due to an increased amount of amino groups on the particle surface. Also MSNs 10 % APTES-PEI modified particles had a slightly higher ζ-potential compared to MSNs 1 % APTES-PEI. The hydrodynamic size for MSN_{ex} 10 % APTES-PEG and MSN_{ex} 1 % APTES-cop 50 showed distorted values. Particles agglomeration might be a reason for the increased size, since here electrostatic stabilisation of the colloidal system is minor (ζ-potentail of + 4.67 mV respectively + 2.37 mV).

Table 6.3: Hydrodynamic size and ζ-potential of PEI, cop 6, cop 50, and PEG modified MSN particles with 1 % respectively 10 % APTES content. The measurements were performed with a ZetaSizer Nano-S under *standard conditions*.

Sample	Z-average [d,nm]	PDI	ζ-potential [mV]
MSN_{ex} 1 % APTES-PEI	320.9 ± 2.6	0.20 ± 0.02	+ 44.3 ± 1.9
MSN_{ex} 1 % APTES-cop 6	296.8 ± 5.8	0.05 ± 0.03	+ 27.1 ± 0.7
MSN_{ex} 1 % APTES-cop 50	3546.3 ± 233.0	0.64 ± 0.09	+ 2.4 ± 0.1
MSN_{ex} 10 % APTES	317.3 ± 9.5	0.09 ± 0.06	+ 18.5 ± 0.9
MSN_{ex} 10 % APTES-PEI	274.7 ± 6.1	0.08 ± 0.03	+ 53.0 ± 1.8
MSN_{ex} 10 % APTES-PEG	1719.0 ± 347.0	0.18 ± 0.05	+ 4.7 ± 0.5

Further modification of the PEI-modified MSN 10 % APTES particles wit PEG decreased the surface charge from + 53.0 mV to + 10.4 mV and to - 61.5 mV for succinic anhydride modified particles (*c.f.*, Table 6.4). The hydrodynamic size showed expected values for all three functionalised particles. Steric and electrostatic effects resulted in a stable, well-dispersed colloidal system.

Table 6.4: Hydrodynamic size and the ζ-potential of MSN_{ex} 10 % APTES-PEI particles after graft polymerisation with PEG, acetic anhydride and succinic anhydride. A stable colloidal system was achieved due to electrostatic repulsion of the particle surface charges.

Sample	Z-average [d,nm]	PDI	ζ-potential [mV]
MSN_{ex} 10 % APTES-PEI-PEG	370.5 ± 12.9	0.19 ± 0.01	+ 10.4 ± 0.4
MSN_{ex} 10 % APTES-PEI-ace.a.	345.6 ± 14.2	0.20 ± 0.02	- 24.0 ± 1.4
MSN_{ex} 10 % APTES-PEI-suc.a.	293.0 ± 3.2	0.08 ± 0.02	- 61.5 ± 2.1

The high negative surface charge obtained after surface fuctionalisation with succinic anhydride can be explained due to carboxylic groups (-COOH) on the particle surface as shown in Figure 6.5.

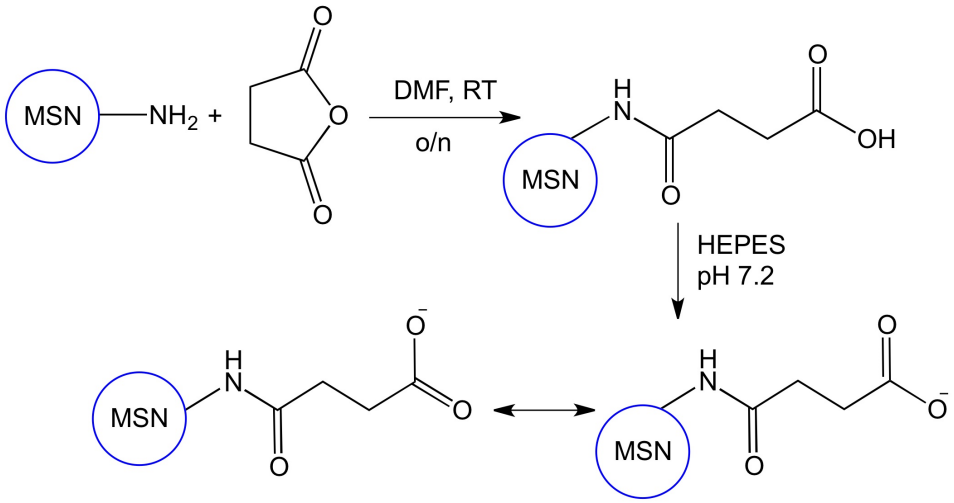

Figure 6.5: Schematic illustration of the graft polymerisation of MSN_{ex} 10 % APTES-PEI with succinic anhydride. At pH 7.2 the carboxyl groups are deprotonated and the carboxylate anion is resonance stabilized due to delocalisation of the negative charge over two oxygen atoms.

Briefly, the surface charge can easily be affected by introducing new surface groups as shown in this section and the results are summarised in Figure 6.6. Hyperbranched amino-functionalised particles had the most positive ζ-potential compared to succinic anhydride coated particles where the ζ-potential was - 61.5 mV. A high positive or negative ζ-potential resulted in stable, well-dispersed colloidal systems due to electrostatic repulsion between the charges on the particle surface. Only MSN_{ex} 1 % APTES cop 50 and MSN_{ex} 10 % APTES PEGylated particles showed an increased size. This can be explained by minor electrostatic and steric stabilisation effects.

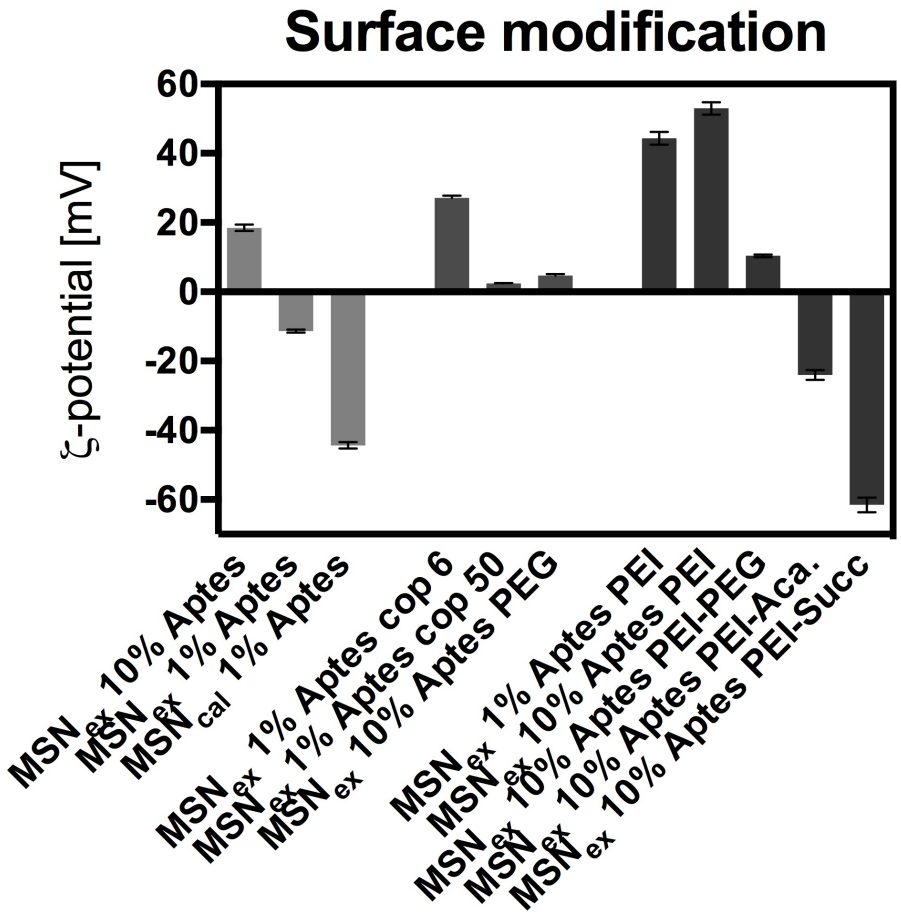

Figure 6.6: Summary of ζ-potential measured with a Zetasizer Nano-S under *standard conditions*. The ζ-potential depends on the particle surface groups. Hydroxyl- or carboxyl groups (PEGylated, acetic anhydride, and succinic anhydride functionalised particles) led to a negative surface charge compared to amino- and copolymer-functionalised particles (APTES, cop 6, cop 50, and PEI) which had a positive surface charge.

6.2.3 Protein adsorption

BSA has a negative surface charge at pH 7.2 and is electrostatically attracted to positively charged particles *e.g.,* PEI functionalised particles. This can be seen by the change of ζ-potential. Before BSA-adsorption PEI, cop 6 and cop 50 modified particles showed a positive surface charge and after incubation with BSA the ζ-potential shifted towards slightly negative values.

Variation of both adsorption time and concentration of BSA resulted in similar changes of the ζ-potential as shown in Figure 6.7 and Figure 6.8. The incubation time (3 and 24 hours) was varied for samples containing 200 $\mu g \cdot mL^{-1}$ BSA. DLS measurements showed distorted values due to agglomeration and are therefore not shown. Major changes in ζ-potential after BSA adsorption were obtained with PEI, 10 %APTES, and cop 6 modified particles as expected. Here, the particles had a high positive surface charge and interactions with the negatively charged protein were preferred. Furthermore, a surface charge close to zero (obtained via PEGylation) resulted in minor interactions with BSA and the ζ-potential slightly changed to a negative value. Minor changes in the ζ-potential were obtained with already negatively charged particles (succcinic anhydride, acetic anhydride, and calcinated), where incubation with the protein reduced the negative surface charge to a lower negative value.

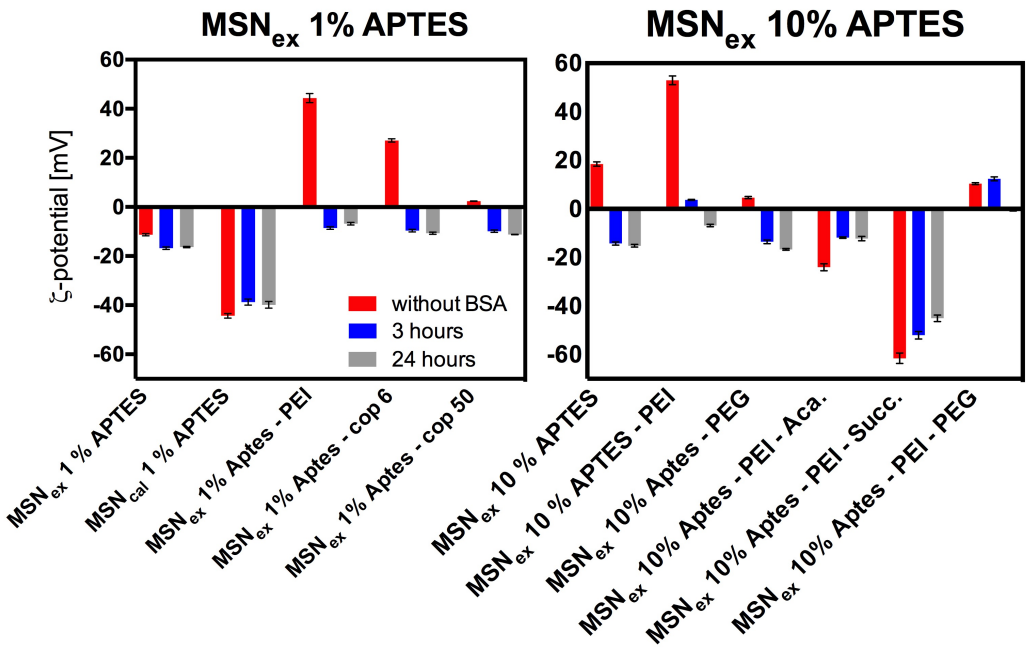

Figure 6.7: Influence of BSA adsorption on the surface charge of MSN particles. BSA was used to mimic the physiological environment. Variation of the incubation time led to almost identical changes of the ζ-potential. Positive ζ-potential values for amino- and copolymer functionalised particles shifted towards slightly negative ones, whereas minor changes for already negative charged particles occurred.

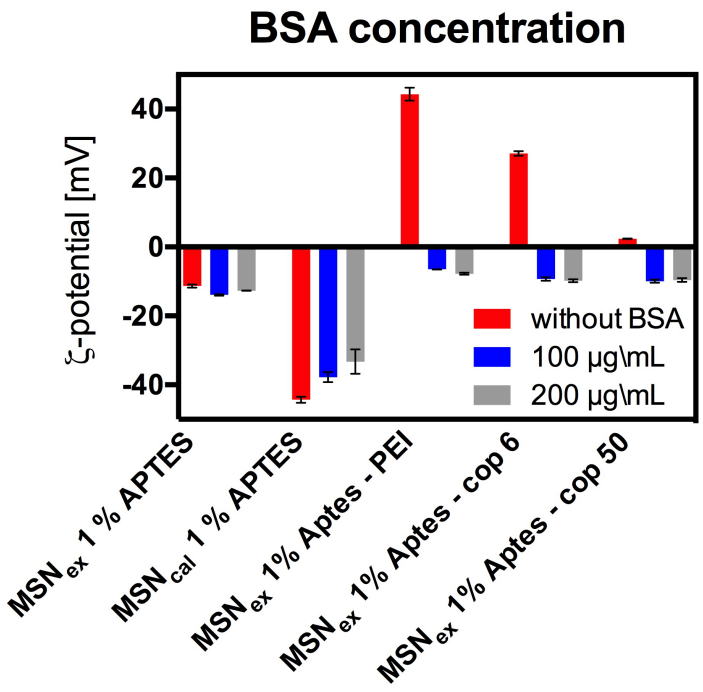

Figure 6.8: Variation of the ζ-potential of modified MSNs 1 % APTES after incubation with BSA. Different BSA-concentrations resulted in similar changes of the ζ-potential. Again, amino- and cop 6 -modification resulted in increased interactions with the negatively charged protein causing in a negative ζ-potential after BSA adsorption.

Furthermore, the amount of adsorbed protein was calculated by comparing incubated particles with samples containing 200 µg·mL^{-1} respectively 100 µg·mL^{-1} BSA in HEPES. Negative values for the protein concentrations were obtained and are not shown in this thesis. The distorted values can be explained due to scattering of light and interactions of the protein with the particles (conformation change).

7 Poly (butyl cyanoacrylate) nanoparticles

7.1 Characterisation techniques used for PBCA

Based on our group's previous work with the quenched near-infrared dye, CytoCy5S, we decided to develop a method to allow directed delivery. To achieve this, CytoCy5S was encapsulated into PBCA nanoparticles. The polymeric particles degrade at physiological pH and were therefore stored under acidic conditions (pH 3). Before usage, PBCA particles were suspended in phosphate buffered saline (PBS) or Tris-HCl (ratio 2:1) for all *in vitro* experiments, then added to medium, and added to cells. The next pages summarises the methods used for PBCA characterisation and *in vitro* experiments.

7.1.1 Nitroreductase enzymatic assay

The spectrophotometic assay was performed to evaluate encapsulation of CytoCy5S in PBCA nanoparticles. Two different UV–Vis spectrophotometers were used to find the optimal characterisation method. Tris-HCl buffer solutions (10 mM and 25 mM) were used for the enzymatic assays. The pH was adjusted with 1 M HCl to a pH 7.5.

NanoDrop 1000
To determine the necessary concentration for UV–Vis spectroscopy an enzymatic assay with pure dye (0.01 mM, 0.025 mM, 0,05 mM, and 0,1 mM) was performed. The required amount of chemicals was pipetted in Eppis and filled up with 25 mM Tris-HCl buffer to a final volume of 200 µL including 8 vol% DMSO to increase the solubility of the dye. The samples were vortexed between each step, covered with alumina foil, and incubated for 1 hour at RT. The final concentrations of NTR and NADH are summarised in 7.1. The blank sample contained Tris-HCl buffer, DMSO and NADH. For measurements (n=3), 2 µL of the samples were used and measured at room temperature.

Table 7.1: Concentration of used cofactors and enzyme for the spectrophotometric assay measured using NanoDrop 1000.

Chemical	Stock solution [μM]	Concentration in assay [μM]
NADH	500	200
NTR	1	0.01

Synergy H1

Stock solutions of 500 μM β-NADH and 7.9 mM NADPH in 10 mM Tris-HCl pH 7.5 were always newly prepared. NTR (1 mM and 10 mM) was dissolved in 25 mM Tris-HCl pH 7.5, aliquoted into 200 μL fractions and stored at -20 °C. The used chemicals for the assay and their final concentration are listed in Table 7.2.

Table 7.2: Concentration of cofactors, enzyme, and CytoCy5S used for the nitroreductase enzymatic assay with Synergy H1.

Chemical	Stock solution [mM]	Concentration in assay [μM]
NADPH	7.9	1000
NADH	0.5	60
NTR	0.01	0.2
CytoCy5S	1	2.5

The aliquot amount of each chemical was pipetted in Eppis, vortexed, and filled up to a total volume of 400 μL with Tris-HCl. CytoCy5S was used as control. NTR was added in the end, vortexed and 100 μL of each sample (n=3) were pipetted into a black 96-well plate. Measurements were performed immediately after with Synergy H1 at room temperature (settings are summarised in Section 5.3).

Absorbance and fluorescence spectra (wavelength range: 300 to 700 nm; excitation wavelength: 631 nm) were measured. Tris-HCl buffer including the two cofactors and DMSO were used as blank samples. During measurements the samples were baseline corrected, which was automatically done by the software if blank samples were defined in advance. Well-area scans were performed to determine the fluorescence intensity during the enzymatic assay. The chosen settings are listed in Table 5.3.

7.1.2 Cell lines and cell culture

Buffer preparation
PBS (10 mM) containing following salts was prepared:

Table 7.3: PBS salt concentrations.

Salt	Concentration [mmol·L^{-1}]	Concentration [g·L^{-1}]
NaCl	137	8.0
KCl	2.7	0.2
Na_2HPO_4	10	1.44
KH_2HPO_4	1.8	0.24

The pH was adjusted with 1 M HCl to pH 7.4 and the prepared buffer solution was autoclaved and stored at 4 °C.

Cell Cultering
Mouse fibroblasts cells and a breast carcinoma cell line, MDA-MB-231, were used for *in vitro* experiments. MDA-MB-231 positive cells were transduced with a Green Fluorescent Protein (GFP), firefly luciferase (Luc) and the Escherichia coli Nfsb nitroreductace (MDA-MB-231$^{GFP+Luc+NTR}$). All cell lines were cultured in Dulbecco's Modified Eagle's Medium (DMEM) with following additives:

- 10 % Heat-inactivated fetal bovine serum.
- 1 % L-glutamine.
- 1 % Penicillin-Streptomycin.

The cells were incubated in a humidified atmosphere at 37 °C and 5 % CO_2. The adherent cell lines were maintained at 70–80 % confluence in 10 x 2 cm cell culture petri dishes and split upon reaching confluence. Medium, PBS, and trypsin were always preheated to 37 °C before usage. First, the medium in the culture dish was removed and the cells were carefully washed with PBS. Next, 2.5 mL of 1X sterile Trypsin-EDTA was added and incubated at 37 °C in 5 % CO_2 for approximately 5 minutes to dissociate the cells from the culture dish. The cells were examined using an optical microscope (10× magnification) to confirm detachment. Then trypsin was neutralised with 5 mL medium (ratio 1 : 2) and the cell suspension was transfered into a falcon tube. The cells were centrifuged (280 g for 5 minutes), the supernatant was discharged, and the cell pellet was re-suspended in 1 mL medium. The appropriate volume of cell suspension was transfered into freshly prepared culture dishes.

Cell counting
A haemocytometer was used to determine the cell concentration. First, the haemocytometer was cleaned with ethanol and the cover slip was carefully fixed. Cells were collected (280 g for 5 minutes), re-suspended in 1 mL medium, 10 µL of the cell suspension were used to fill the haemocytometer, and the cells were counted using an optical microscope (10× magnification). In Figure 7.1 a haemocytometer and a 16 square area are shown. The cells were counted within 16 squares, plus all the cells on two boundary lines.

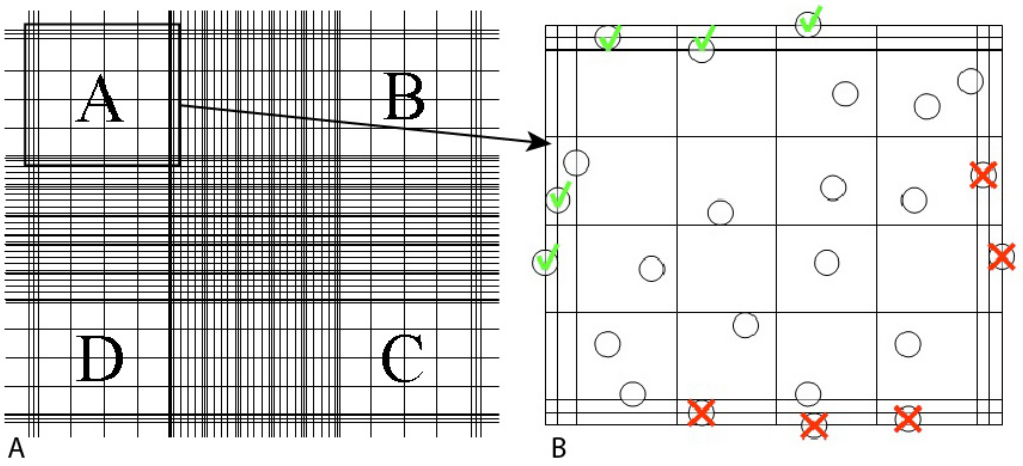

Figure 7.1: Determining the cell concentration: **A** a haemocytometer [119] and **B** a set of 16 squares [120]. Only healthy cells within these fields and along two boundary lines were counted.

The amount of cells was calculated (*c.f.*, Eqn.7.1) with:

$$\text{cells / mL suspension}\,[10^6] = \frac{\tilde{x}}{100}, \tag{7.1}$$

where $\tilde{x}$ is the mean of cells in three 16 square fields.

7.1.3 Flow Cytometry

For the experiment MDA-MB-231^{wt} (NTR$^-$) and MDA-MB-231$^{GFP+Luc+NTR}$ (NTR$^+$) cells were used. The adherent cells were cultured in 6-well plates as previously reported.

In brief, the medium was removed, cells were washed with 1 mL PBS and incubated with a nanoparticles-containing mixture at 37 °C and 5 % CO_2. NTR^- and NTR^+ cells without adds were used as reference samples and CytoCy5S (0.69 $\mu g \cdot mL^{-1}$ in medium, incubation time one hour) was used as positive control. Subsequently, the medium was removed, the cells were washed with 1 mL PBS and trypsinised (300 µL) for 3 to 5 minutes. After detaching, medium (ratio 2:1) was added to stop trypsinisation, the suspension was transfered into flow-tubes and the cells were pelleted by centrifugation (280 g for 5 minutes). The supernatant was discarded and the cell pellet was re-suspended in 1 mL PBS and collected. The cell pellet was then re-suspended in 100 µL PBS and kept on ice till measured. If the measurements did not take place within three hours, the cells were fixed with 100 µL 4 % paraformaldehyde (PFA) and stored in the fridge.

Different concentrations of PBCA particles (7.6 µg–76 µg in 1 mL medium/buffer) were used for incubation (20 hours) to find a compromise between cell-toxicity and minimal concentration, which allows optical tracking. Nanoparticles-incubation and cell-preparation was done as previously described.

After determining an appropriate concentration NTR^+ and NTR^- cells were incubated with particle-containing (38 $\mu g \cdot mL^{-1}$) medium for 1 h, 2 h, 4 h, 8 h and 24 h. Preparation and work-up was the same as earlier explained.

The amount of endcytosed particles was analysed using flow cytometry and the MFI of cells in channel FL4-A was measured. For all measurements NTR^- and NTR^+ without adds were used to determine the living cell population. A gate was set on the FSC vs SSC plot to restrict the analysis to a specific population within the sample as shown in Figure 7.2**A**. Furthermore, a threshold of 500 000 on FSC-H was set and 10 000 events within the gate were chosen.

Normalised histograms with markers were used to specify the range of events for a single parameter. An example is shown in Figure 7.2**B**. NTR^- cells incubated with CytoCy5S were used to place the marker and anything within this gate (on the right) is designate as positive events.

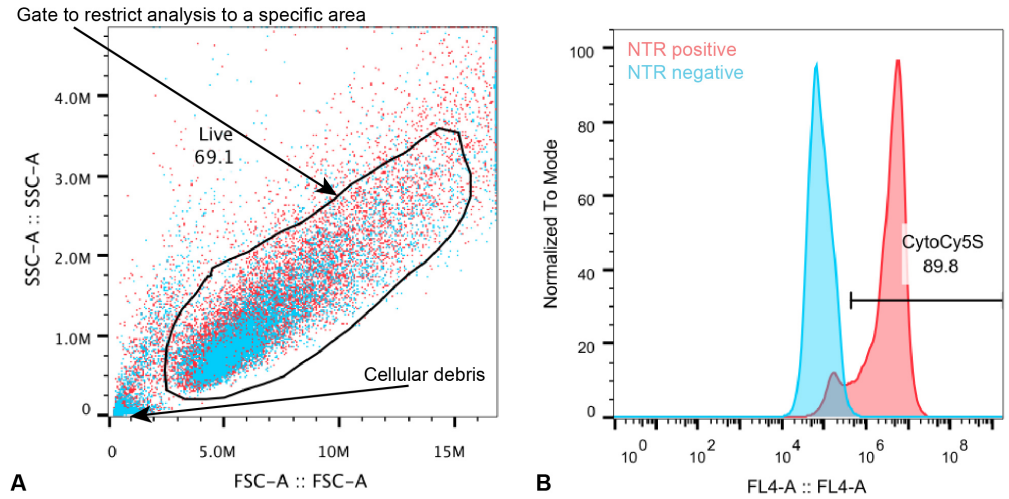

Figure 7.2: Flow cytometry analysis. 1×10^4 cells were analysed by flow cytometry with a 640 nm excitation laser and 675/12.5 nm band-pass filter. NTR^+ cells are shown in red and NTR^- in blue. **A** A FSC vs SSC plot was used to establish the gate for living cell population. Dead cells (cell debris) were beyond this gate. **B** Normalised histograms were used to set the range of positive CytoCy5S events.

7.1.4 Fluorescence microscopy

For optical imaging NTR^- and NTR^+ cells were seeded into µ-dishes with glass-bottom at a density of 5 x 10^5 cells. The cells were incubated with PBCA-containing medium (38 $\mu g \cdot mL^{-1}$) for 24 hours.

To obtain a better signal NTR^+ and NTR^- cells were also incubated with a higher amount of PBCA nanoparticles (76 $\mu g \cdot mL^{-1}$). CytoCy5S (0.69 $\mu g \cdot mL^{-1}$) was used as positive control. After incubation, cells were washed three times with PBS and fixed with 4 % PFA (15 to 20 minutes), washed again three times with PBS and after drying the cells were mounted with ProLong® Gold Antifade Mountant (molecular probes® by Life Technologies™, USA) to fluorescently label the nuclei. Afterwards, all samples were covered with sterile glass slides and charactersied using fluorescence microscopy.

7.2 Results and Discussion

7.2.1 Nitroreducatase enzymatic assay

NanoDrop 1000
A weak absorption band around 650 nm was found with a dye concentration of 0.025 mM. However, no significant results were obtained during the enzymatic assay with 0.2 mM CytoCy5S. Replication of published data [121] led to similar values for $A_{maximum}$ and A_{280} at the beginning, but the signal showed hardly any difference after incubation with NTR for 1 hour compared to the signal after 5 minutes. Limitations of the equipment, such as detection limit, can be a reason for no notable signal.

The following calculations were made to compare the amount of pure dye with encapsulated CytoCy5S in PBCA nanoparticles. First the amount of substance was calculated using (*c.f.*, Eqn.7.2):

$$n = c \cdot V, \tag{7.2}$$

where n is the amount of substance in mol, c is the concentration in mol·L^{-1}, and V is the volume in liter.

The mass can be further calculated with Equation 7.3:

$$m = M \cdot n, \tag{7.3}$$

where m is the mass of the substance in gramm, and M is the molecular weight of CytoCy5S (691,768 g·mol^{-1}) resulting in 0.69 µg for the used amount of pure CytoCy5S (1 µL of 1 mM dye solution).

This amount was then compared to PBCA with 0.45 wt% dye encapsulated. The PBCA concentration in acidic water was 7.6 mg·mL^{-1}. Therefore 20 µL contained 0.152 mg nanoparticles with 0.68 µg CytoCy5S encapsulated, which is equal to the used CytoCy5S-solution.

However, the necessary dye concentration (< 0.025 mM; equates 17 µg CytoCy5S) for NanoDrop 1000 measurements could not be achieved with 0.45% loaded PBCA nanoparticles.

Synergy H1
The quenched dye showed a weak emission at about 670 nm and pure NPs had a similar profile as shown in Figure 7.3. However, loaded PBCA naoparticles had a very high emission at about 670 nm with a relative fluorescence unit (RFU) of about 200. This suggests that the particles had CytoCy5S encapsulated but that the dye was destroyed during the mini-emulsion using a radical initiator to start the anionic polymerisation.

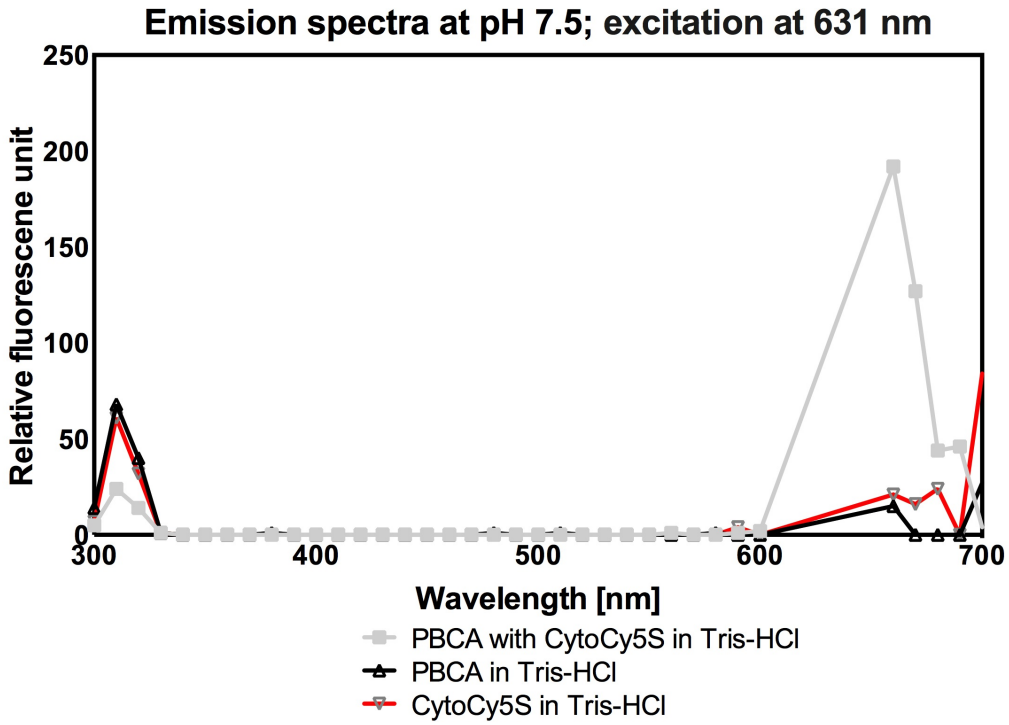

Figure 7.3: Spectrophotometric analysis at pH 7.5 showing the emissions spectra of CytoCy5S, loaded and unloaded PBCA particles. CytoCy5S, in the quenched state, had only a weak emission signal around 670 nm, whereas PBCA-CytoCy5S particles had a RFU of 200 at this wavelength.

CytoCy5S absorbed in the region of about 570 to 680 nm compared to pure NPs, which absorbed across the whole spectrum, highest at 300 nm, with an exponential decrease in absorption as shown in Figure 7.4. Dye loaded PBCA nanoparticles showed a similar profile but also had an increase in absorption at the CytoCy5S wavelengths.

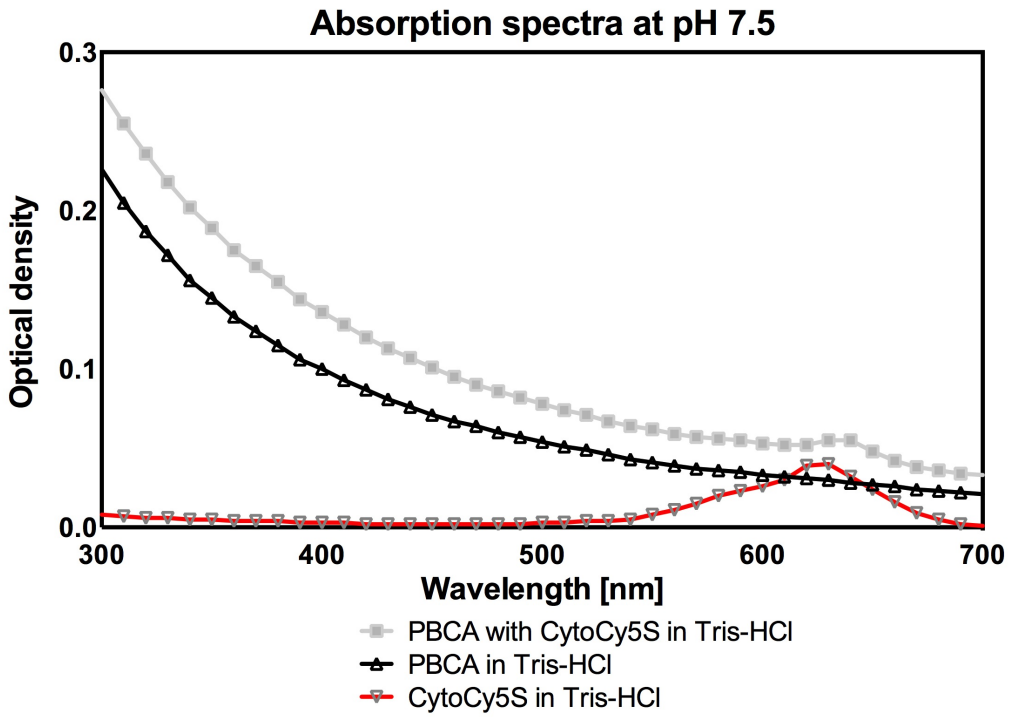

Figure 7.4: Spectrophotometric analysis at pH 7.5 viewing the absorption spectra. CytoCy5S only absorbed between 570 to 680 nm. Loaded and unloaded PBCA particles showed a similar spectra with a high absorbance around 300 nm and decreasing absorbency. Loaded particles exhibited also an increase of the optical density at the wavelength of CytoCy5S.

The enzymatic assay with CytoCy5S and NTR showed 150-fold contrast in fluorescence over the time course compared to loaded PBCA without NTR, which had already a high baseline (150 to 200). Addition of NTR increased the fluorescence to about 600 RFU (*i.e.*, 3-fold increase). This led to the conclusion that the particles had encapsulated CytoCy5S and the dye was released in the assay at pH 7.5 due to degradation of PBCA nanoparticles. The rate of release was quick and resulted in a only three times brighter signal than the background. However, the high background and high emission after excitation suggests, that there was a considerable amount of unquenched dye incorporated within the particles. The particles were synthetised by anionic polymersation involving an radical initiator, which could have interact with the dye.

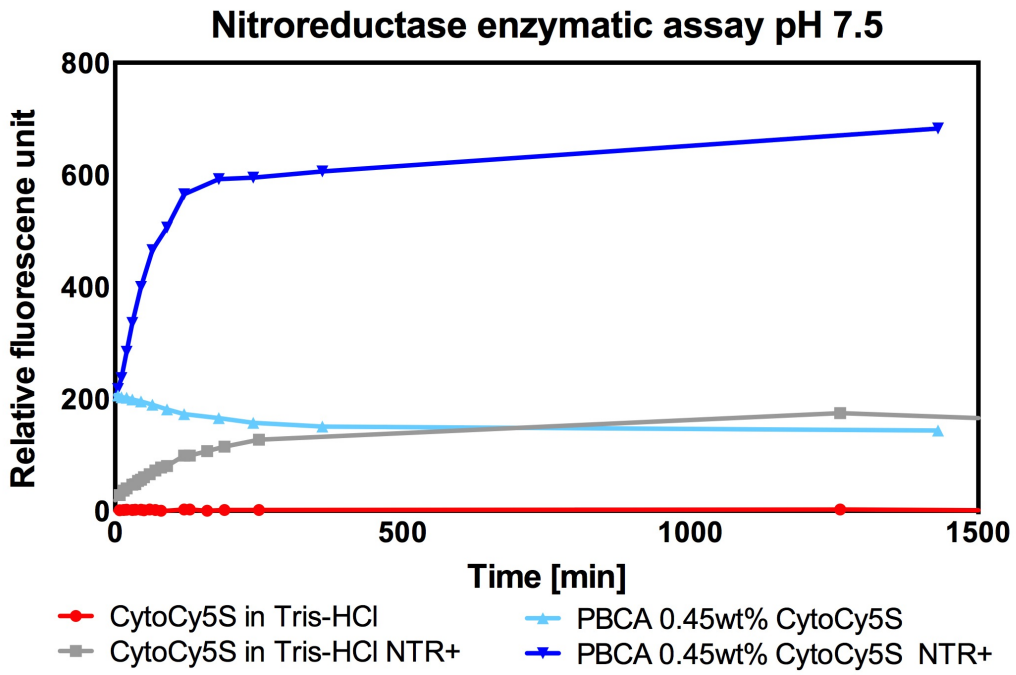

Figure 7.5: Spectrophotometic assay at pH 7.5 measured using Synergy H1. The enzymatic assay with CytoCy5S and NTR showed 150-fold increase in fluorescence over time with a minimal background signal for CytoCy5S. Loaded PBCA without NTR had already a high background signal. The fluorescence signal increased 3-times when NTR was added.

7.2.2 *In vitro* characterisation using flow cytometry

For cell viability measurements NTR^- cells were compared with NTR^+ cells. A FSC vs SSC plot (*c.f.*, Figure 7.6**A**) was used to determine the living cell population. A first experiment showed toxic effects on cells when a high amount of PCBA (152 µg·mL^{-1}) was used. Cells started to detach after incubation, when they were washed with PBS and the amount of living cells was reduced by 1/3 as shown in Figure 7.6**B**. In addition, forward- and side-scattered light can be used to roughly estimate the cell size and cell granularity, which both changed to the left side of the graph. This is a sign of increased cellular debris (leftovers when cells die).

As shown in Figure 7.7 the MFI increased with larger amounts of PBCA nanoparticles. Incubation with CytoCy5S (0.69 µg·mL^{-1}) resulted in twice the MFI compared to incubation with 76 µg·mL^{-1} PBCA (equates 0.35 µg CytoCy5S, which is half the amount as used when cells were incubated with pure dye).

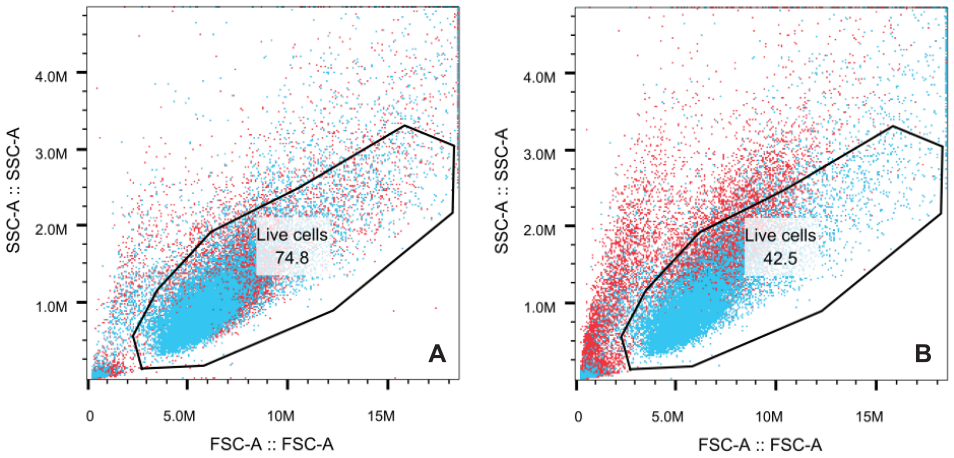

Figure 7.6: Flow cytometry results after incubation with PBCA nanoparticles. 1×10^4 cells were analysed by flow cytometry with a 640 nm excitation laser and 675/12.5 nm band-pass filter. NTR^+ cells are shown in red and NTR^- in blue. **A**: cells incubated for 1 hour with CytoCy5S (0.69 µg·mL^{-1}). A gate was set to determine living cell population, and **B**: cells after 20 hours incubation with PBCA nanoparticles. The cell viability reduced by 1/3 after incubation with 152 µg·mL^{-1} PBCA nanoparticles.

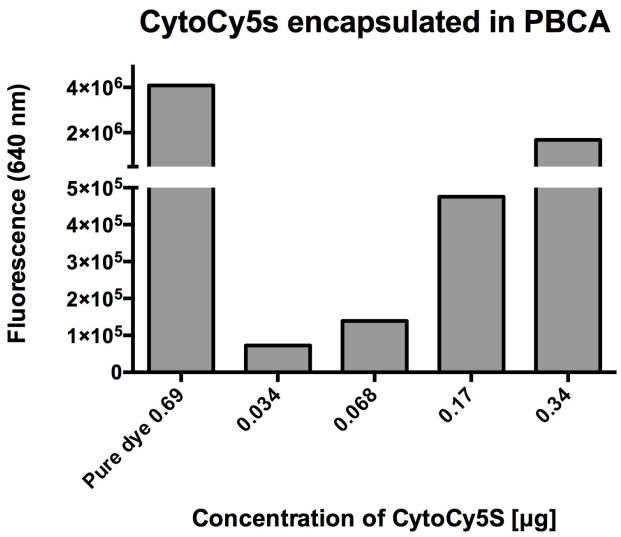

Figure 7.7: Flow cytometry analysis. Comparison of the MFI (median in FL4-A channel) of cells incubated with pure dye and dye encapsulated in PBCA nanoparticles. Pure dye showed twice the fluorescence intensity in contrast to PBCA particles, which can be explained by twice the amount of pure dye used.

Figure 7.8 shows the obtained MFI after several timepoints. NTR^+ cells were incubated with 38 $\mu g \cdot mL^{-1}$ PBCA particles, equates 0.17 µg CytoCy5S. NPs were uptaken within one hour and a significant increase in fluorescence intensity was achieved during the first four hours. Even after 8 hours a high fluorescence signal was obtained, which decreased afterwards.

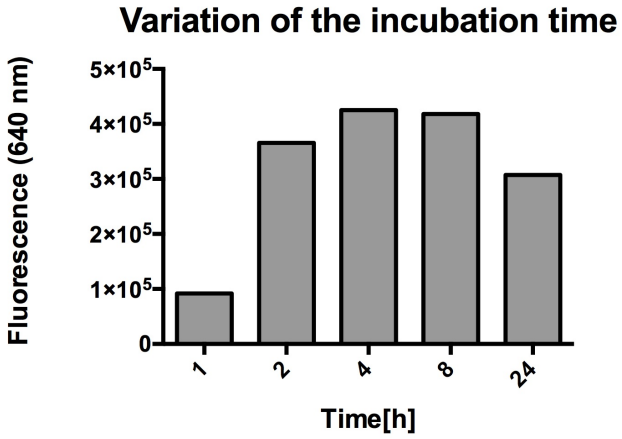

Figure 7.8: Flow cytometry analysis. The fluorescence signal was measured at different timepoints. Cells were incubated with 38 $\mu g \cdot mL^{-1}$ PBCA nanoparticles (roughly 0.17 µg CytoCy5S). The highest signal was obtained after 4 hours and the signal decreased afterwards.

7.2.3 Fluorescence microscopy

Figure 7.9 shows fluorescence images taken with an inverted fluorescence microscope using a 20× objective. Fluorescence microscopy of the DAPI stained nuclei (blue), GFP (green), NTR/CytoCy5S (red) resulted in bright fluorescence in all channels (supplementary Figure 7.9 **DAPI, GFP, CytoCy5S**). Overlay and magnification of GFP, CytoCy5S and DAPI showed good correlation (*c.f.*, 7.9 **combined**).

No fluorescence signal with the NTR^- cells and CytoCy5S and a minimal background noise in the GFP channel was seen. NTR^- cells cannot reduce the dye and therefore no signal was obtained. The positive control sample, CytoCy5S incubated with NTR^+ cells, showed a bright red fluorescence signal after 1 hour. This indicates that the dye was unquenched as expected.

These results show that in the NTR^+ cells, the dye was unquenched, whilst in the NTR^- cells, no dye was unquenched. These results are positive as they indicated that the PBCA nanoparticles were uptaken by the cells and the dye was successfully released. Specifically, after 1 hour incubation, low CytoCy5S florescence was observed, as a longer

time is needed for the PBCA nanoparticles to be uptaken. After 24 hours, an increased CytoCy5S signal was observed in the NTR^+ cells, whilst no signal was seen in the NTR^- cells.

These results also correlate to flow cytometry analysis (*c.f.*, Section 7.2.2), where a maximum fluorescence intensity was obtained after 4 hours.

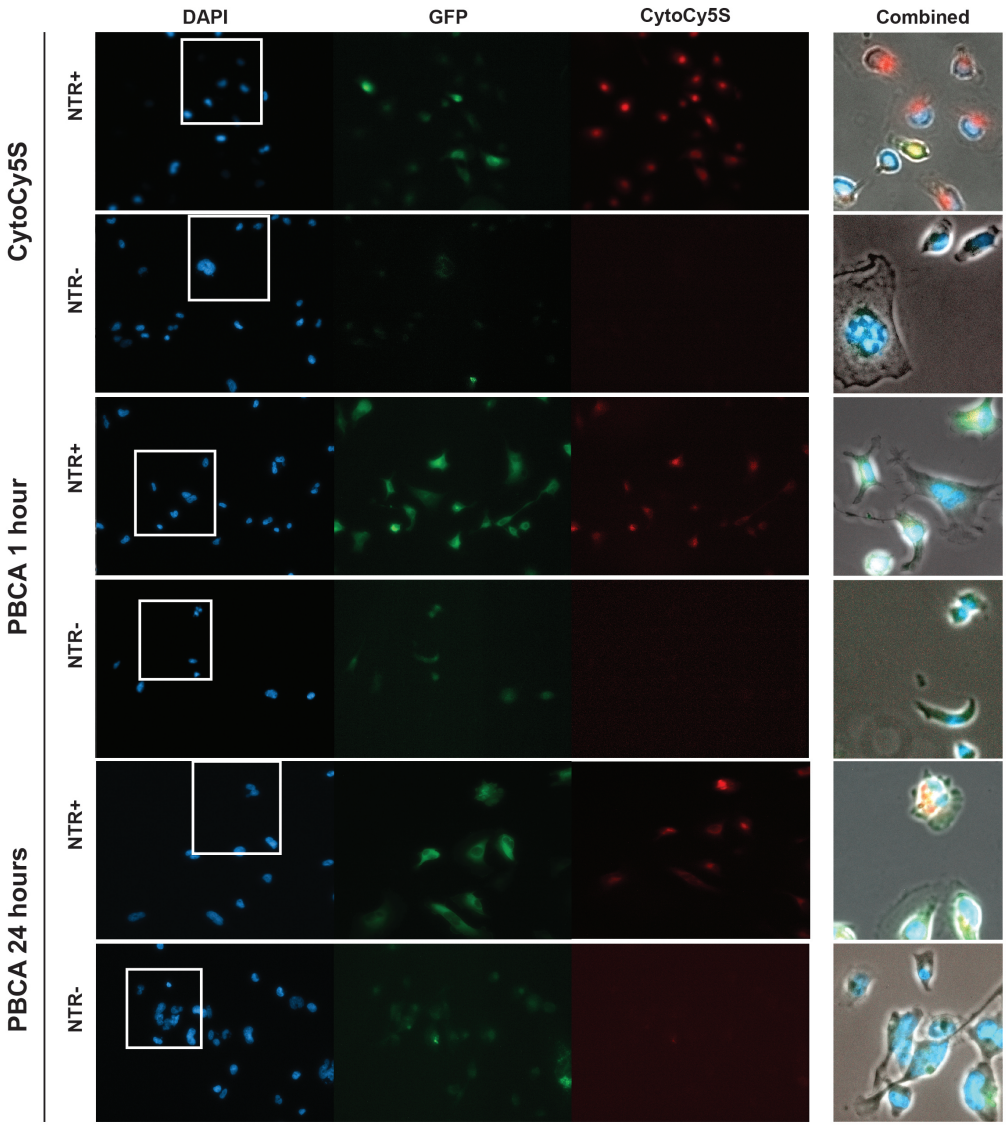

Figure 7.9: Images via fluorescence microscopy using 20× magnification. The nuclei (blue) was stained with DAPI to simplify visualisation. NTR^- and NTR^+ cells incubated with CytoCy5S (1 h) and PBCA nanoparticles (1 h and 24 h). White frame in DAPI-images indicate ROI chosen for combined-images. NTR^+ cells showed positive results for GFP and CytoCy5S. The control sample (CytoCy5S incubated with NTR^+) showed a bright red fluorescence signal. In all three cases no signal for CytoCy5S and NTR^- was obtained as expected. Incubation with PBCA for 1 hour led to a weak fluorescence signal, which increased after 24 hours (yellow/red).

8 MSNs as imaging agents *in vitro* and *in vivo*

8.1 Methods

On the following pages the methods for particles characterisation in *in vitro* and in *in vivo* are described.

8.1.1 MR imaging

Particle preparation
MSNs doped with $Gd(aca)_3$ ($4\,mg{\cdot}mL^{-1}$ in DMSO) were sonicated and vortexed for 15 minutes, the aliquot amount was transfered in an Eppi and collected (10 000 rpm for 10 minutes). The pellet was washed once with ethanol and re-dispersed (15 min ultrasonic-bath and vortex) in ethanol. Subsequently, a cop 6 solution ($4\,mg{\cdot}mL^{-1}$) in ethanol was prepared and sonicated for 15 to 20 minutes. The copolymer (100 wt%) was added to the particle suspension, sonicated and vortexed for 15 minutes and then stirred at RT for 2.5 hours to allow electrostatic adsorption onto the MSNs. The final concentration of copolymer and particles in suspension was $2\,mg{\cdot}mL^{-1}$. The coated particles were separated (10 000 rpm for 10 minutes), washed with 25 mM HEPES buffer solution and re-dispersed (15 to 20 minutes sonication treatment) in HEPES.

Undoped MSNs were used as reference and were prepared in the same way as Gd^{3+}-doped particles.

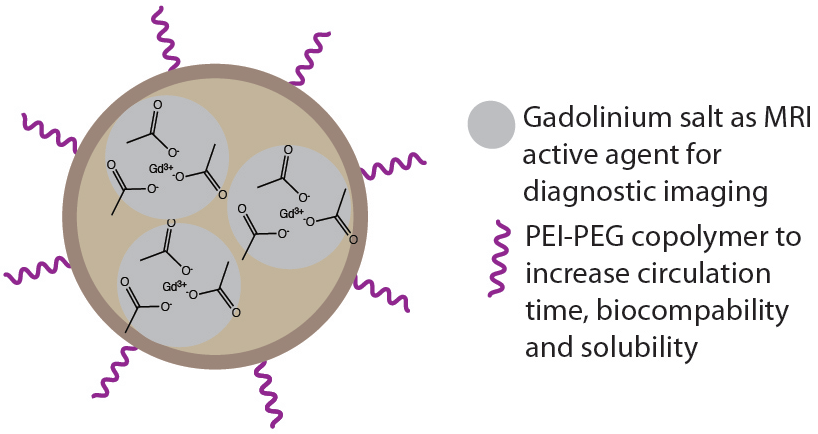

Figure 8.1: Schematic representation of a gadolinium-doped MSN particle. Gadolinium is used as contrast agent for MR imaging *in vivo*. Surface coating with the copolymer increases the stability of the colloidal system, blood circulation time, and biocompatibility.

MR imaging *in vivo*

This pilot study was done to test the feasibility of Gd-doped MSNs. All experiments were approved by The Norwegian Animal Research Authority and conducted according to The European Convention for the Protection of Vertebrates Used for Scientific Purposes. Utilized mice were strained with an Il2rgtm1Wjl targeted mutation leading to severe combined immunodeficiency (University of Bergen, Norway). These NOD-*scid* γ-mice were originally a generous gift of Prof. Leonard D. Schultz (Jackson Laboratories, USA). The animals were housed in individually ventilated cages (Techniplast, Italy) in groups of four or less and kept on a 12-hour dark/light schedule at a constant temperature of 21 °C and 50 % relative humidity. The animals had continuous access to food and autoclaved water.

For subcutaneous tumor model, ARN8 melanoma cells (1×10^6 cells mixed with matrixgel 1:0.5) were injected in the right flank of NOD-*scid* γ-mice and grouped into: Gd-doped MSNs ($Gd(aca)_3$-cop 6), non-doped MSNs (MSN-cop 6), and Dotarem®. Gadolinium and 1,4,7,10-tetraazacyclododecane-1,4,7,10-tetraacetic acid form a macrocyclic structure as shown in Figure 8.2. This chelat-complex, known as Dotarem®, is EMA approved and used as clinical MRI contrast agent.

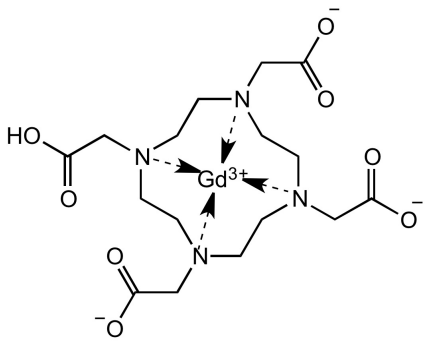

Figure 8.2: Molecular structure of gadolinium^{+3} cation; 2-[4,7,10-tris(carboxymethyl)-1,4,7,10-tetrazacyclododec-1-yl]acetate or gadoteric acid (Dotarem®).

The agents were introduced via injector in the tail vein of the mice (n=2 for Gd-doped MSNs, n=1 undoped MNSs, and n=2 for Dotarem®), with a catheter connected in advance. The total volume injected for each mouse was 200 µL. Gd-doped and non-doped MSNs were used at a dose of 20 mg·kg^{-1} body weight (BW), corresponding to approximately 8 µmol Gd·kg^{-1} BW and Dotarem® was used at a dose of 250 µmol Gd·kg^{-1} BW.

Tumor-bearing mice were anaesthetised with 3 % isofurane (IsoFlo, Abbot Labor Ltd, UK.), which was reduced to 1.5 % when they were asleep. MR properties were characterised using a 7 T horizontal-bore preclinical scanner (Pharmascan 70/16, Bruker Coorporation, Germany). T_1-weighted images for Gd-doped MSNs were acquired before injection, immediately after, and after 24, 48, 72, 96 and 168 hours. Non-doped and Dotarem® injected mice were scanned before injection, immediately after, and after 24 hours and the signal intensity of tumor, kidney, muscle and background region were measured within a defined region of interest (ROI).

8.1.2 Verification of cellular uptake of MSNs

MSNs with lipophilic dyes as model drug

To verify and analyse the potential of MSNs to deliver poorly water-soluble agents to cells, particles loaded with two lipophilic dyes were incubated with a mouse fibroblast cell line. The hydrophobic fluorophores are shown in Figure 8.3 and were used as 'model drugs'.

Nanoparticles in medium (20 µg·mL^{-1}) were incubated with mouse fibroblast cells for 24 hours at 37 °C and 5 % CO_2. Next, the free nanaoparticles were aspirated, the cells were washed three times with PBS, trypsinated, neutralised with medium, and collected

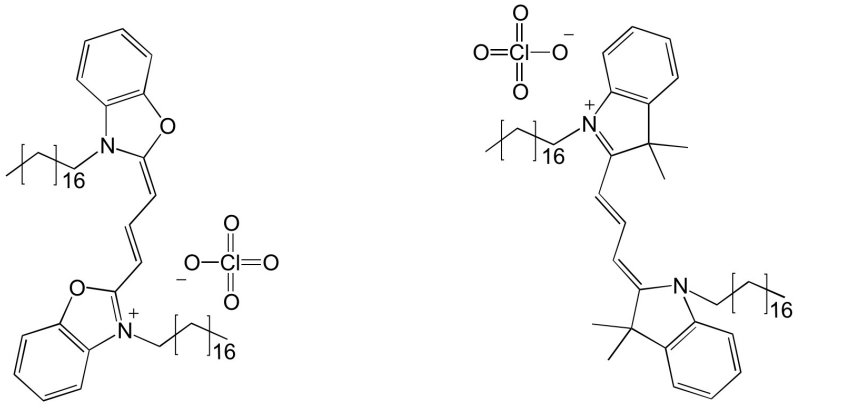

Figure 8.3: 3,3'-Dioctadecyloxacarbocyanine perchlorate (DiO) and 1,1'-Dioctadecyl-3,3,3'3'-tetramethylindocarbocyanine perchlorate (DiI) incorporated in MSNs. The hybrid carrier system was studied using fluorescence microscopy.

(1500 rpm for 5 min). Subsequently, the medium was removed, the particles were re-dispersed in 4 mL medium and 1 mL medium-cell suspension was transfered into a µ-dish with glass-bottom (ibidi GmbH, München, Germany). After cell attachment the medium was removed, the cells were washed again three times with PBS and fixed with 4 % PFA solution for 15 to 20 minutes. Then washed three times with PBS, dried (20 to 30 min) and mounted with ProLong® Gold Antifade Mountant with DAPI to fluorescently label the nuclei. A sterile cover slide was added and the samples were covered in alumina foil. Cells were then viewed using an inverted fluorescence microscope as described in Section 5.2.4.

8.1.3 CytoCy5S-NHS-ester conjugation

Another promising way to use CytoCy5S as NTR reporter gene system was to conjugate the NHS-ester onto amino-functionalised MSNs. For this experiment MSNs-PEI-FITC and MSNs-PEI particles were used.

A 1 mg·mL^{-1} dye-solution in anhydrous DMF was prepared. For the particle conjugation 0.1 wt%, 1 wt%, and 5 wt% of the NHS-ester were used.

The particles were weight in Eppis and dried over night at room temperature in a vacuum chamber (0.5 mbar). Various experiments with different solvents were performed. The particles were either dispersed (20 to 30 min sonication treatment) in HEPES buffer solution at pH 7.2, in $NaHCO_3$ buffer solution at pH 8.3, in DMF with 10 vol% $NaHCO_3$ pH 8.3 or in DMF. The NHS-ester was then added to the particles and the mixture was sonicated and vortexed for another 20 min. Subsequently, the particle-dye dispersion was stirred at room temperature for 1 to 4 hours when using an aqueous buffer and 1 to 24 hours when DMF-$NaHCO_3$ or DMF was used. After the conjugation the particles were separated (2 500 rpm for 15 minutes), re-dispersed in ethanol, centrifuged (6 500 rpm for 15 minutes) and re-dispersed in HEPES buffer solution. The washing step with ethanol was done twice when DMF was used and particles were re-dispersed in Tris-HCl pH 7.5.

Characterisation *in vitro*
NTR^- and NTR^+ cells were seeded in 6-well plates (1×10^5 cells per well) for flow cytometry experiments and in µ-dishes with glass bottom for optical characterisation. The medium was replaced after cell attachment with a freshly prepared MSNs-containing medium (20 $\mu g \cdot mL^{-1}$) and incubated for 1 and 24 hours. CytoCy5S in medium was used as control (0.69 $\mu g \cdot mL^{-1}$) and incubated with cells for 1 hour. During incubation all samples were covered with alumina foil to avoid contact with ambient light. After incubation, the supernatant was removed and the samples were carefully washed with PBS (1 mL). For flow cytometry samples were trypsinated, collected, re-supsended in 1 mL PBS, separated, re-supsended in 100 µL PBS and stored on ice. If the samples were not measured within a few hours, cells were fixed with 100 µL 4 % PFA.

For staining and visualisation, the cells were washed two times with PBS, fixed with 4 % PFA (15 to 20 min), washed three times with PBS and dried for 20 to 30 min on a flow bench. Subsequently, cells were mounted with ProLong® Gold Antifade reagent for nuclear labeling. A sterile glass slide was put on top and the samples were characterised using fluorescence microscopy.

Spectrophotometric enzymatic assay
The used chemicals and sample preparation are described in Section 7.1.1 and Table 7.2. The aliquot amount of each chemical was pipetted in Eppis, vortexed, and filled up to a total volume of 400 µL with Tris-HCl respectively Tris-HCl-nanoparticles. CytoCy5S was used as control. NTR was added in the end, vortexed and 100 µL of each sample (n=3) were pipetted into a black 96-well plate and measured immediately with Synergy H1 at room temperature (settings are summarised in Section 5.3).

8.2 Results

8.2.1 MR imaging *in vivo*

The anatomical body of a mouse and regions of interest are shown in Figure 8.4. Here, the mouse was treated with Dotarem® and the tumor tissue was brighter compared to muscle tissue.

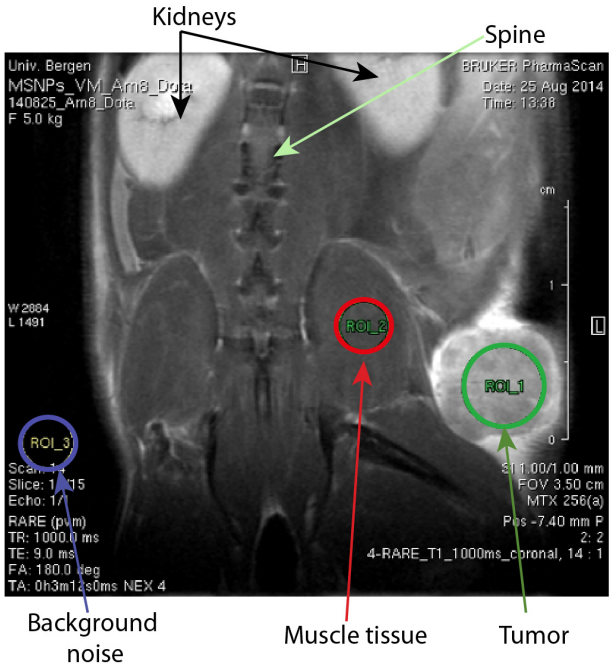

Figure 8.4: Anatomical MR image of a tumor-bearing mouse. The signal intensity of the muscle tissue (red), tumor (green) and background noise (blue) were measured.

Figure 8.5**A** shows MRI images of a mouse treated with Gd-doped MSN particles over a four-day period. In these figures, two regions of interest (ROI) have been chosen; ROI 1 is a sample area of healthy muscle tissue, and ROI 2 is a sample area of the subcutaneous tumor. Similar regions have been chosen of the time course. Tumor growth can be seen over this four-day period.

The average signal intensities (SI) within the tumor, muscle tissue, kidney and background noise were evaluated (*c.f.*, Figure 8.5**B**). Due to day-to-day natural variations in SI, the SI in the tumor was normalised by using the muscle tissue as the control sample. This was done to compensate heterogeneities in the magnetic field (B_0) and inhomogeneities in MSNs concentrations. Figure 8.5**C** shows the tumor tissue-to-

muscle tissue SI-ratio. A minor increase in SI-ratio can be seen after 24 h. This increase was expected due to the EPR effect. Nevertheless, the small sample size (n=2 for Gd-doped MSNs and n=2 for Dotarem®) resulted in a large standard deviation (error-bars). From 24 to 96 hours the SI-ratio progressively decreases as predicted.

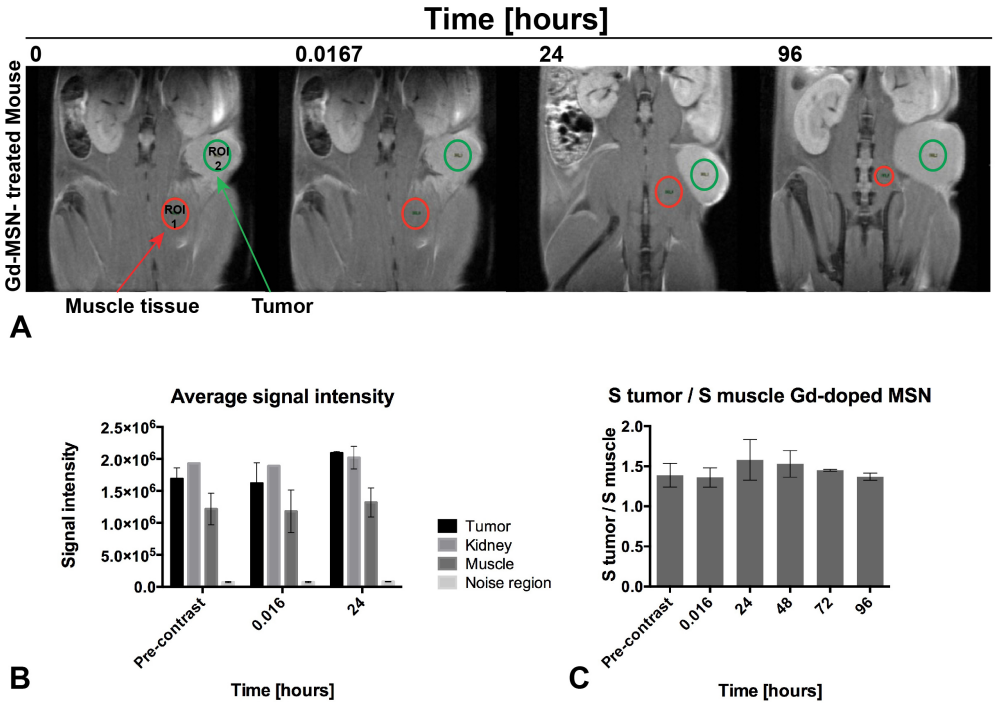

Figure 8.5: MR images. **A** T_1-weighted images of ROIs (green and red labeled) before and immediately after injection, and after 24 and 96 hours of a melanoma-bearing and Gd-MSNs treated mouse. **B** Average SI were evaluated in tumor, kidneys, muscle and noise region. Only the SI of tumor tissue changed over time. **C** The SI of the tumor was normalised with the SI of normal muscle tissue to compensate heterogeneities in Gd-dose and magnetic field.

The contrast in T_1-weighted images for Dotarem® treated mice showed a maximum SI immediately after injection and decreased afterwards drastically (*c.f.*, Figure 8.6**A**). Gd-treated mice showed nearly constant changes of the SI in examined ROIs as shown in Figure 8.6**B**. There was no change in the SI with non-doped MSNs over time as expected.

There was no significant change in the MR signal over the four-days period with Gd-doped mice (*c.f.*, Figure 8.6**C**). This could be due to a significantly lower used Gd-dose (8 µmol for Gd-doped MSNs compared to 250 µmol for Dotarem®). Nevertheless, these particles show a minor increased SI compared to unloaded MSNs, which seems promising.

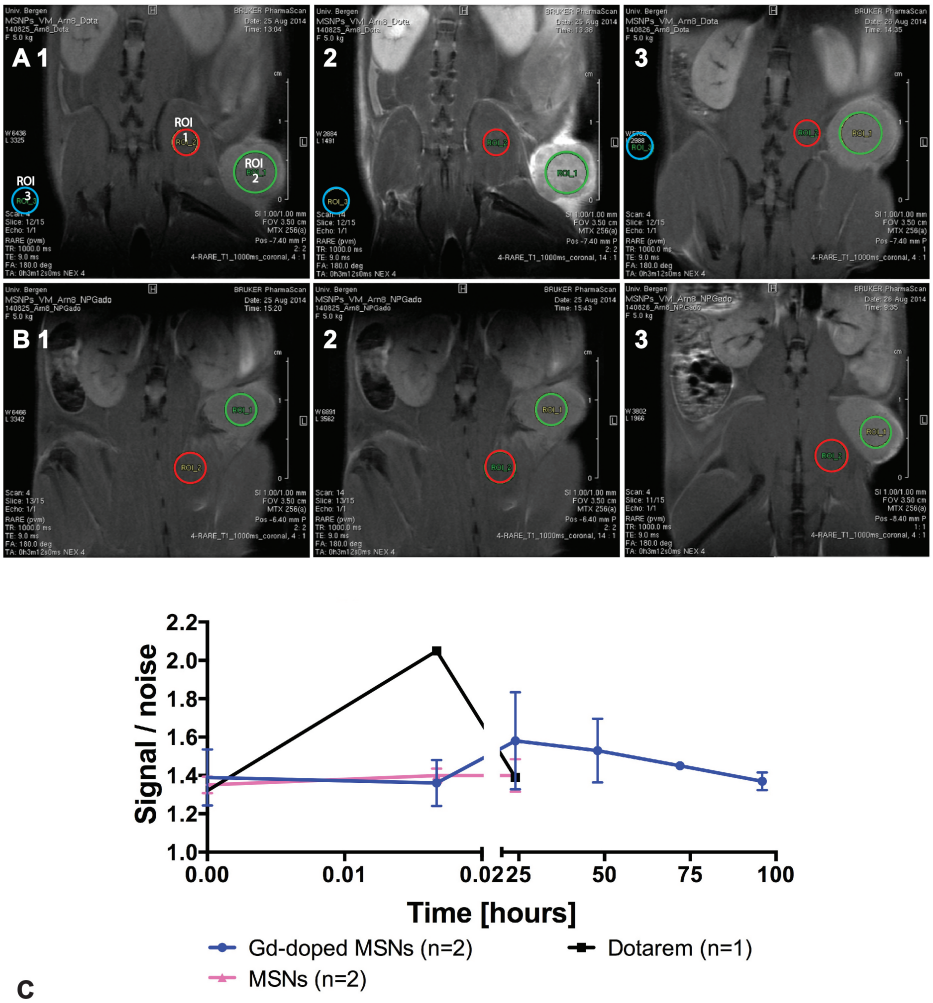

Figure 8.6: MR images of a mouse injected with Gd-doped particles and a mouse injected with Mouse injected with Dotarem®. **A** Mouse injected with Dotarem®: **1** pre-contrast, **2** post-contrast, and **3** after 24 hours. **B**: Gd-doped MSNs **1** pre-contrast, **2** immediately after injection (post-contrast), and **3** after 24 hours. **C** Singal/noise over time for Gd-doped MSNs, non-doped MSNs, and Dotarem® injected mice. Dotarem® (black line) showed the highest signal immediately after injection and decrease afterwards rapidly. No signal change was obtained with unloaded MSNs (pink line) and minor changes in SI were obtained for Gd-doped MSNs (blue).

Nevertheless, this pilot study shows the potential for MSNs for theranostics applications with MRI based visualisation. The lower Gd-dose reduces toxicity and long-term imaging may be possible. However, the slow excretion (long-term accumulation in tissue) of Gd^{3+}-doped MSNs, could results in toxicological issues.

8.2.2 Cellular uptake of labeled MSN particles

Intracellular delivery of cargo loaded MSNs was studied using fluorescence microscopy and a 63× oil immersion objective to increase resolution and brightness. After 24 hours incubation, dye-loaded particles were localised in the endosomes around the nuclei (blue) as shown in Figure 8.7.

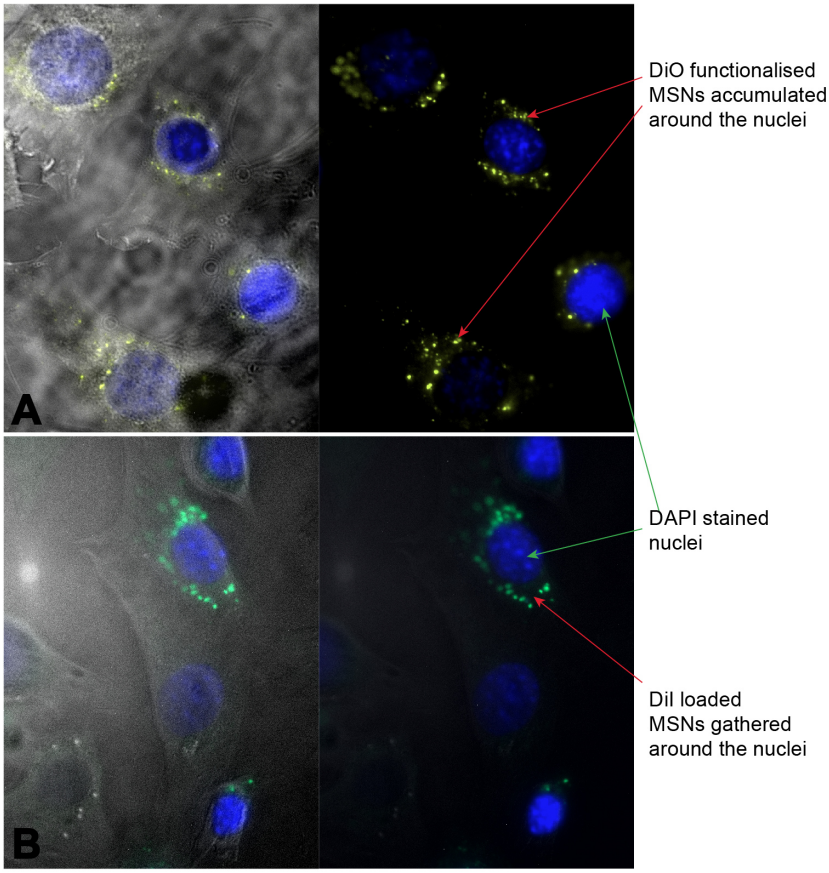

Figure 8.7: Fluorescence microscope images of labeled MSNs after 24 hours with a 63× oil immersion objective. Nuclear deoxyribonucleic acid was stained with DAPI to simplify visualisation (blue) **A** shows cells incubated with DiO loaded particles. The particles (yellow) gathered in the endosomes around the nuclei and **B** shows cells with DiI labeled MSNs (green).

Particles were endocytosed and intracellular delivery and accumulation in the endosomal area of two hydophobic dyes was successfully demonstrated. Many anticancer drugs are hydrophobic and MSNs are promising carrier systems for drug delivery in cancer treatment.

8.2.3 Characterisation of CytoCy5S conjugated MSN particles

Conjugations in HEPES, $NaHCO_3$ and DMF with MSN-PEI-FITC were unsuccessful. Here, blue colored particles were obtained whilst white particles were obtained when pure DMF was used. However, *in vitro* experiments showed negative results, since no signal of CytoCy5S (MSN-PEI-FITC,CytoCy5S) was obtained and images are therefore not shown. Nevertheless, cellular uptake could be confirmed, since a signal for FITC could be seen.

Conjugation in DMF with 10 vol% $NaHCO_3$ and MSNs-PEI seems promising. Again blue particles were obtained and a spectrophotometric enzymatic assay was performed. The fluorescence signal over time was measured to approve particle-dye conjugation as shown in Figure 8.8. The pure dye reached a fluorescence maxima after 24 hours and decreased afterwards rapidly compared to CytoCy5S conjugated NPs. The NPs had a low background signal (similar to pure dye) and showed a slow increase of the RFU with a maximum after 23 hours (approximately 50-fold increase). The RFU kept afterwards nearly constant for another three days.

During the assay CytoCy5S (0.272 µg per well) was used as reference. For the conjugation 1 wt% of NHS-ester was used, which equals approximately 2.8 µg per well if the conjugation would have been 100 % successful. This was not the case, since CytoCy5S conjuncted particles showed an increase of fluorescence over time, but it was five times lower when compared to pure dye. The conjugation was only partial successful and the amount of conjugated dye could not be quantified yet. Nevertheless, first positive results for the conjugation were obtained and CytoCy5S conjuagted MSNs showed even after three days a fluorescence signal, which could be used for long-term monitoring.

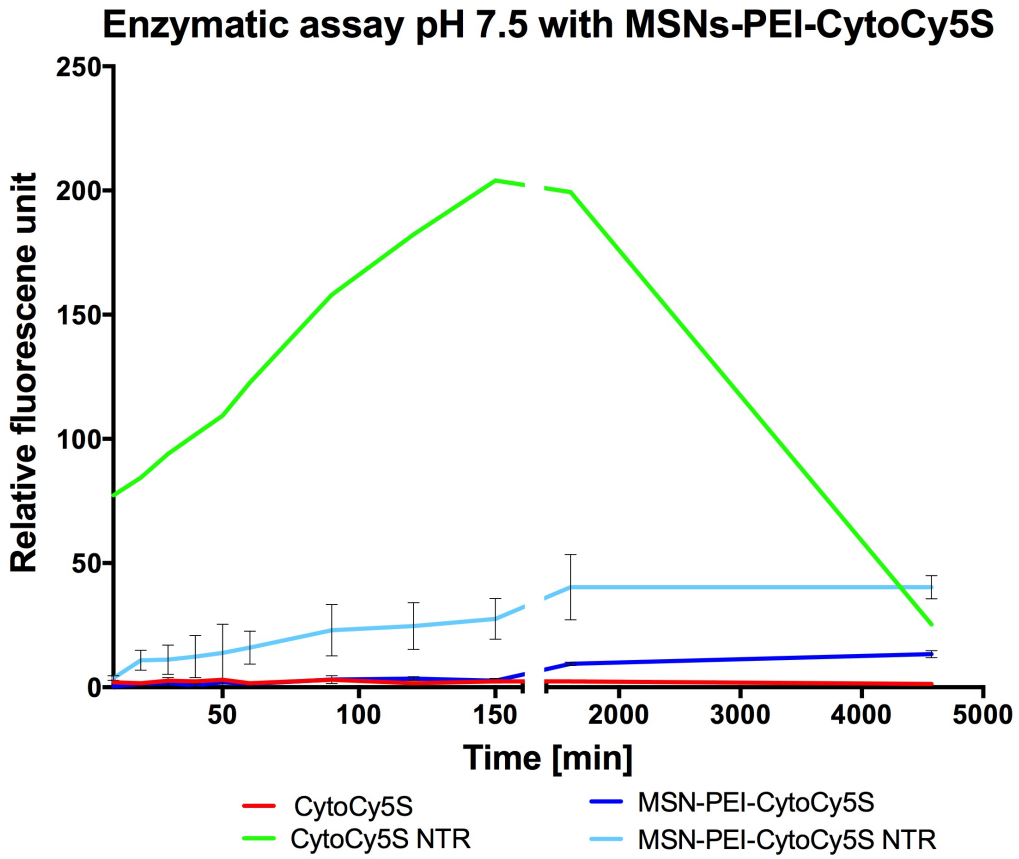

Figure 8.8: Spectrophotometric assay at pH 7.5 with CytoCy5S and CytoCy5S-MSN-PEI particles. Pure dye reached a maximum RFU after 150 min (200-fold increase), had a high fluorescence until 23 hours and decreased drastically afterwards. Conjugated MSNs showed a slow decrease of the signal over time and reached their maximum (50-fold increase) after 23 hours. The fluorescence signal kept even after 3 days constant.

9 Conclusion and Outlook

In conclusion, obtained results demonstrated that MSNs can be modified with different polymers, and loaded or conjugated with imagining agents. The surface chemistry is crucial for NP interaction with cells. For clinical applications, the size and surface charge play a key role and nanomaterials have to fulfill several requirements, such as chemical stability, high target sensitivity, good image contrast, non-specific binding to serum proteins, and sufficiently circulation time. MSNs can satisfy all these criteria depending on their functionalisation. It was shown that PEGylation 'camouflages' particles and protein adsorption was minimised. On the other hand, a positive surface charge (*e.g.*, amino-functionalised MSNs) led to higher interactions with the negatively charged protein. Stable colloidal systems were obtained with a high positive or negative surface charge (ζ-potential $> \pm 20$ mV), which can be achieved by -amino, -carboxyl, or -hydroxyl surface modification.

Furthermore, it was shown that MSNs can be used as drug carriers. Cellular uptake was demonstrated using MSNs loaded with two hydrohpobic dyes, as model drugs. After 24 hours the particles were endocytosed and accumulation around the nucleus was observed.

In addition, NPs may be used as contrast agents for optical imaging *in vivo*. During the pilot study, Gd-doped MSNs were used for MR imaging with a 30-fold lower concentration compared to a standard contrast agent Dotarem®. The lower used Gd-dose might lead to reduced toxicological effects. A minor increase of the MR signal was seen after 24 hours for mice treated with the Gd-doped MSNs. However, long-term consequences of accumulated MSNs are unclear and more experiments need to be performed to verify obtained results and to study long-term behavior of the nanoparticles.

The MSNs and polymeric nanoparticles were evaluated as carrier systems by loading them with a NIR-infrared fluorescent probe. Results from a spectrometric assay showed a high background signal suggesting that the dye was unquenched during particles synthesis. In addition, PBCA particles were not stable at pH 7.5 resulting in dye-release and a 3-times increase of the fluorescence signal over time during the enzymatic assay. Furthermore, *in vitro* experiments confirmed cellular uptake of these particles which

seems promising. Fluorescence was observed in NTR^+ cells using flow cytometry with a maximum fluorscence signal after 4 hours. However, PBCA nanoparticles had a cytotoxic effect on cells if used in high concentrations. Nevertheless, investigation in CytoCy5S-loaded PBCA nanoparticles is desirable, especially with the new PBCA-formulation (without initiator) and a higher payload of CytoCy5S.

The conjugation of the NHS-ester with MSNs was partially successful. The spectrophotometric enzymatic assays showed an increase (50-fold) of the fluorescence intensity over time but also a very low background signal. In addition, a minor decrease in the fluorescence signal was seen over three days; this is promising for long-term imaging. Further conjugations with different surface functionalised MSNs (cop 6, PEI, *etc.*) and different solvents should be carried out to improve the CytoCy5S conjugation. In the future, CytoCy5S conjugated MSNs should be studied in *in vitro* with triple-negative breast cancer cells, to characterise cellular uptake and fluorescence intensity.

In summary, these nanomaterials have a great potential for theranostic applications. The particles can be easily modified depending on the required application. Moreover, polymeric nanoparticles degrade at physiological pH and the degradation can be tuned using different polymers. CytoCy5S modified particles can be as used novel imaging probes targeting nitroreductase.

List of Tables

List of Figures

Bibliography

[1] World Health Organization, "WHO | Cancer," 2014. http://www.who.int/mediacentre/factsheets/fs297/en/ [Accessed: 16/10/2014]

[2] R. C. Petersen, "Free-radical polymer science structural cancer model: a review." *Scientifica*, vol. 2013, Jan. 2013.

[3] Cancer Research UK, "Cancer incidence by age," 2014. http://www.cancerresearchuk.org/cancer-info/cancerstats/incidence/age/#Adults6 [Accessed: 18/10/2014]

[4] G. Cooper, *Elements of Human Cancer*, 1992.

[5] M. Yu, J. Park, and S. Jon, "Targeting strategies for multifunctional nanoparticles in cancer imaging and therapy," *Theranostics*, vol. 2, pp. 3–44, 2012.

[6] Cancer Registry of Norway, "Cancer in Norway 2012 - Cancer incidence, mortality, survival and prevalence in Norway." Cancer Registry of Norway, Oslo, Tech. Rep., 2014.

[7] P. Singh, S. Joshi, P. Russell, N. Verma, X. Wang, and A. Khatri, "Molecular chemotherapy and chemotherapy: a new front against late-stage hormone-refractory prostate cancer," *Clinical cancer research : an official journal of the American Association for Cancer Research*, vol. 17, no. 12, pp. 4006–18, Jun. 2011.

[8] J. Bhosle and G. Hall, "Principles of cancer treatment by chemotherapy," *Surgery (Oxford)*, vol. 27, no. 4, pp. 173–177, Apr. 2009.

[9] C.-H. Heldin, K. Rubin, K. Pietras, and A. Ostman, "High interstitial fluid pressure - an obstacle in cancer therapy." *Nature reviews. Cancer*, vol. 4, no. 10, pp. 806–13, Oct. 2004.

[10] I. Brigger, C. Dubernet, and P. Couvreur, "Nanoparticles in cancer therapy and diagnosis," *Advanced Drug Delivery Reviews*, vol. 54, pp. 631–651, 2002.

[11] D.-E. Lee, H. Koo, I.-C. Sun, J. Ryu, K. Kim, and I. Kwon, "Multifunctional nanoparticles for multimodal imaging and theragnosis," *Chemical Society Reviews*, vol. 41, pp. 2656–72, 2012.

[12] J. Xie, S. Lee, and X. Chen, "Nanoparticle-based theranostic agents." *Advanced drug delivery reviews*, vol. 62, no. 11, pp. 1064–79, Aug. 2010.

[13] N. Sanvicens and M. Marco, "Multifunctional nanoparticles -properties and prospects for their use in human medicine." *Trends in biotechnology*, vol. 26, no. 8, pp. 425–33, Aug. 2008.

[14] H. Kobayashi, R. Watanabe, and P. Choyke, "Improving conventional enhanced permeability and retention (EPR) effects; what is the appropriate target?" *Theranostics*, vol. 4, no. 1, pp. 81–9, Jan. 2013.

[15] X. Chao, Z. Zhang, L. Guo, J. Zhu, M. Peng, A. Vermorken, W. Van de Ven, C. Chen, and Y. Cui, "A novel magnetic nanoparticle drug carrier for enhanced cancer chemotherapy," *PloS one*, vol. 7, no. 10, p. e40388, Jan. 2012.

[16] V. Torchilin, "Tumor delivery of macromolecular drugs based on the EPR effect," *Advanced Drug Delivery Reviews*, vol. 63, pp. 131–135, 2011.

[17] M. Perfézou, A. Turner, and A. Merkoçi, "Cancer detection using nanoparticle-based sensors," *Chemical Society Reviews*, vol. 41, p. 2606, 2012.

[18] T. Reya, S. Morrison, M. Clarke, and I. Weissman, "Stem cells, cancer, and cancer stem cells." *Nature*, vol. 414, no. 6859, pp. 105–11, Nov. 2001.

[19] N. Bhowmick, E. Neilson, and H. Moses, "Stromal fibroblasts in cancer initiation and progression." *Nature*, vol. 432, no. 7015, pp. 332–7, Nov. 2004.

[20] American Cancer Society, "Acute Myeloid Leukemia (Myelogenous)," 2013. http://www.cancer.org/cancer/leukemia-acutemyeloidaml/detailedguide [Accessed: 15/10/2014]

[21] D. Chiras, *Human Body Systems: Structure, Function and Environment*. Jones & Bartlett Learning, 2003.

[22] B. Bonavida, *Molecular Mechanisms of Tumor Cell Resistance to Chemotherapy: Targeted Therapies to Reverse Resistance*. Springer Science & Business Media, 2013.

[23] European Medicines Agency, "Medicines." http://www.ema.europa.eu/ema/ [Accessed: 11/11/14]

[24] DIANE Publishing Company, *Bone Marrow Transplantation and Peripheral Blood Stem Cell Transplantation*. DIANE Publishing, 1996.

[25] C. Springer and I. Niculescu-Duvaz, "Approaches to gene-directed enzyme prodrug therapy (GDEPT)." *Advances in experimental medicine and biology*, vol. 465, pp. 403–9, Jan. 2000.

[26] Z. Karjoo, V. Ganapathy, and A. Hatefi, *Gene Therapy of Cancer*. Elsevier, 2014.

[27] G. W. Both, "Gene-directed Enzyme Prodrug Therapy for Cancer: A Glimpse into the Future?" *Discovery Medicine*, vol. 8, no. 42, pp. 97–103, Oct. 2009.

[28] D. Thurston, *Chemistry and Pharmacology of Anticancer Drugs*. CRC Press, 2006, vol. 22.

[29] H. McCarthy, A. Yakkundi, V. McErlane, C. Hughes, G. Keilty, M. Murray, L. Patterson, D. Hirst, S. McKeown, and T. Robson, "Bioreductive GDEPT using cytochrome P450 3A4 in combination with AQ4N," *Cancer gene therapy*, vol. 10, no. 1, pp. 40–8, Jan. 2003.

[30] F. McCormick, "Cancer gene therapy: fringe or cutting edge?" *Nature reviews. Cancer*, vol. 1, no. 2, pp. 130–41, Nov. 2001.

[31] C. J. Springer, *Suicide Gene Therapy: Methods and Reviews*. Springer Science & Business Media, 2004.

[32] E. McCormack, E. Silden, R. West, T. Pavlin, D. Micklem, J. Lorens, B. Haug, M. Cooper, and B. T. Gjertsen, "Nitroreductase, a near-infrared reporter platform for in vivo time-domain optical imaging of metastatic cancer," *Cancer Research*, vol. 73, pp. 1276–1286, 2013.

[33] W. Denny, "Nitroreductase-based GDEPT," *Current Pharmaceutical Design*, vol. 8, no. 15, pp. 1349–1361, Jul. 2002.

[34] I. Oliveira, D. Bonatto, J. a. Antonio, and P. Henriques, "Nitroreductases : Enzymes with Environmental , Biotechnological and Clinical Importance," pp. 1008–1019, 2010.

[35] Cleveland Clinic, "Image Guided Radiation Therapy," 2014. http://my.clevelandclinic.org/services/cancer/treatments-procedures/radiation-therapy/image-guided-radiation-therapy [Accessed: 19/10/2014]

[36] H. Liang, J. Tang, M. Halliwell, and P. Wells, "Sonoporation, drug delivery, and gene

therapy," *Proceedings of the Institution of Mechanical Engineers, Part H: Journal of Engineering in Medicine*, vol. 224, no. 2, pp. 343–361, Feb. 2010.

[37] V. Kagan, H. Bayir, and A. Shvedova, "Nanomedicine and nanotoxicology: two sides of the same coin." *Nanomedicine : nanotechnology, biology, and medicine*, vol. 1, no. 4, pp. 313–6, Dec. 2005.

[38] B. Haley and E. Frenkel, "Nanoparticles for drug delivery in cancer treatment." *Urologic oncology*, vol. 26, no. 1, pp. 57–64, Jan. 2008.

[39] J. Rosenholm, E. Peuhu, J. Eriksson, C. Sahlgren, M. Lindén, and M. Linden, "Targeted intracellular delivery of hydrophobic agents using mesoporous hybrid silica nanoparticles as carrier systems," *Nano letters*, vol. 9, no. 9, pp. 3308–11, Sep. 2009.

[40] C. Giordano, D. Albani, A. Gloria, M. Tunesi, S. Rodilossi, T. Russo, G. Forloni, L. Ambrosio, and A. Cigada, "Nanocomposites for neurodegenerative diseases: hydrogel-nanoparticle combinations for a challenging drug delivery." *The International journal of artificial organs*, vol. 34, no. 12, pp. 1115–27, Dec. 2011.

[41] S. Krol, R. Ellis-Behnke, and P. Marchetti, "Nanomedicine for treatment of diabetes in an aging population: state-of-the-art and future developments." *Maturitas*, vol. 73, no. 1, pp. 61–7, Sep. 2012.

[42] M. Ferrari, "Cancer nanotechnology: opportunities and challenges." *Nature reviews. Cancer*, vol. 5, pp. 161–171, 2005.

[43] F. Tang, L. Li, and D. Chen, "Mesoporous silica nanoparticles: synthesis, biocompatibility and drug delivery." *Advanced materials (Deerfield Beach, Fla.)*, vol. 24, pp. 1504–34, 2012.

[44] G. Sahay, D. Alakhova, and A. Kabanov, "Endocytosis of nanomedicines." *Journal of controlled release : official journal of the Controlled Release Society*, vol. 145, no. 3, pp. 182–95, Aug. 2010.

[45] E. McCormack, "Formulation of Drugs for Cancer Therapy," 2014.

[46] Z. Li, J. Barnes, A. Bosoy, J. Stoddart, and J. Zink, "Mesoporous silica nanoparticles in biomedical applications," *Chem Soc Rev*, vol. 41, no. 7, pp. 2590–2605, 2012.

[47] T. Doane and C. Burda, "The unique role of nanoparticles in nanomedicine: imaging, drug delivery and therapy," *Chem Soc Rev*, vol. 41, no. 7, pp. 2885–2911, 2012.

[48] M. Swierczewska, G. Liu, S. Lee, and X. Chen, "High-sensitivity nanosensors for biomarker detection," *Chemical Society Reviews*, vol. 41, p. 2641, 2012.

[49] T. Allen and P. R. Cullis, "Liposomal drug delivery systems: from concept to clinical applications." *Advanced drug delivery reviews*, vol. 65, no. 1, pp. 36–48, Jan. 2013.

[50] A. Faraji and P. Wipf, "Nanoparticles in cellular drug delivery," *Bioorganic & medicinal chemistry*, vol. 17, no. 8, pp. 2950–62, Apr. 2009.

[51] H.-C. Huang, S. Barua, G. Sharma, S. Dey, and K. Rege, "Inorganic nanoparticles for cancer imaging and therapy." *Journal of controlled release : official journal of the Controlled Release Society*, vol. 155, pp. 344–57, 2011.

[52] S. Jain, D. Hirst, and J. O'Sullivan, "Gold nanoparticles as novel agents for cancer therapy," *The British journal of radiology*, vol. 85, no. 1010, pp. 101–13, Feb. 2012.

[53] M.-C. Jones and J.-C. Leroux, "Polymeric micelles – a new generation of colloidal drug carriers," *European Journal of Pharmaceutics and Biopharmaceutics*, vol. 48, no. 2, pp. 101–111, Sep. 1999.

[54] S. Holder and N. Sommerdijk, "New micellar morphologies from amphiphilic block copolymers: disks, toroids and bicontinuous micelles," *Polymer Chemistry*, vol. 2, pp. 1028–1028, 2011.

[55] D. Balazs and W. Godbey, "Liposomes for use in gene delivery," *Journal of drug delivery*, vol. 2011, p. 326497, 2011.

[56] K. Soppimath, T. Aminabhavi, A. Kulkarni, and W. Rudzinski, "Biodegradable polymeric nanoparticles as drug delivery devices," *Journal of Controlled Release*, vol. 70, no. 1-2, pp. 1–20, Jan. 2001.

[57] J. Rao and K. Geckeler, "Polymer nanoparticles: Preparation techniques and size-control parameters," *Progress in Polymer Science*, vol. 36, no. 7, pp. 887–913, Jul. 2011.

[58] L. Halliwell, "Investigation and synthesis of alkyl cyanoacrylates and modification of x-ray contrast agents for incorporation into alkyl cyanoacrylate for use in medical devices," PhD, University of Warwick, Mar. 2013.

[59] C. Kresge, M. Leonowicz, W. Roth, J. Vartuli, and J. Beck, "Ordered mesoporous molecular sieves synthesized by a liquid-crystal template mechanism," *Nature*, vol. 359, no. 6397, pp. 710–712, Oct. 1992.

[60] L. Bergman, "Influence of suface functionalization on the behavior of silica

nanoparticles in biological systems," Academic dissertation, Abo Akademi University, 2014.

[61] S. Svenson and R. Prud'homme, *Multifunctional Nanoparticles for Drug Delivery Applications: Imaging, Targeting, and Delivery*. Springer Science & Business Media, 2012.

[62] S.-H. Wu, C.-Y. Mou, and H.-P. Lin, "Synthesis of mesoporous silica nanoparticles." *Chemical Society reviews*, vol. 42, pp. 3862–75, 2013.

[63] M. Qhobosheane, S. Santra, P. Zhang, and W. Tan, "Biochemically functionalized silica nanoparticles." *The Analyst*, vol. 126, pp. 1274–1278, 2001.

[64] I. Rahman and V. Padavettan, "Synthesis of Silica Nanoparticles by Sol-Gel: Size-Dependent Properties, Surface Modification, and Applications in Silica-Polymer Nanocomposites—A Review," *Journal of Nanomaterials*, vol. 2012, 2012.

[65] P. Yang, S. Gai, and J. Lin, "Functionalized mesoporous silica materials for controlled drug delivery," *Chem Soc Rev*, vol. 41, no. 9, pp. 3679–3698, May 2012.

[66] A. Stein, B. Melde, and R. Schroden, "Hybrid Inorganic-Organic Mesoporous Silicates—Nanoscopic Reactors Coming of Age," *Advanced Materials*, vol. 12, no. 19, pp. 1403–1419, Oct. 2000. http://onlinelibrary.wiley.com/doi/10.1002/1521-4095(200010)12:19<1403::AID-ADMA1403>3.0.CO;2-X/abstract

[67] A. Bhattacharya, J. Rawlins, and P. Ray, *Polymer Grafting and Crosslinking*. John Wiley & Sons, 2009.

[68] T. Xia, M. Kovochich, M. Liong, H. Meng, S. Kabehie, S. George, J. Zink, and A. Nel, "Polyethyleneimine coating enhances the cellular uptake of mesoporous silica nanoparticles and allows safe delivery of siRNA and DNA constructs," *ACS nano*, vol. 3, no. 10, pp. 3273–86, Oct. 2009.

[69] M. Etienne and A. Walcarius, "Analytical investigation of the chemical reactivity and stability of aminopropyl-grafted silica in aqueous medium," *Talanta*, vol. 59, no. 6, pp. 1173–88, May 2003.

[70] A. M. Smith, M. Mancini, and S. Nie, "Bioimaging: second window for in vivo imaging." *Nature nanotechnology*, vol. 4, no. 11, pp. 710–1, Nov. 2009.

[71] S. Prahl, "Optical Absorption of Hemoglobin," 1999. http://omlc.org/spectra/hemoglobin/ [Accessed: 14/12/14]

[72] M. Rahman, "Introduction to Flow Cytometry," Oxford, UK, 2014.

[73] G. T. Hermanson, *Bioconjugate Techniques*. Academic Press, 2013.

[74] D. Hayworth, "Chemistry of Crosslinking." http://www.piercenet.com/method/chemistry-crosslinking#nhsester [Accessed: 01/11/2014]

[75] Malvern Instruments Ltd., *Zeta Potential - An Introduction in 30 Minutes*.

[76] A. Revil, P. Pezard, and P. Glover, "Streaming potential in porous media: 1. Theory of the zeta potential," *Journal of Geophysical Research: Solid Earth*, vol. 104, no. B9, pp. 20 021–20 031, 1999.

[77] S. Honary and F. Zahir, "Effect of Zeta Potential on the Properties of Nano-Drug Delivery Systems - A Review (Part 1)," *Tropical Journal of Pharmaceutical Research*, vol. 12, no. 2, pp. 255–264, May 2013. http://www.ajol.info/index.php/tjpr/article/view/88554

[78] G. Gözke, *Electrofiltration of Biopolymers : Spatially Distributed Process Analysis*. KIT Scientific Publishing, 2012.

[79] Colloidal Dynamics LLC, "The Zeta Potential," 1999. http://www.colloidal-dynamics.com/docs/CDElTut1.pdf [Accessed: 12/10/2014]

[80] Particle Sciences, "An Overview of the Zeta Potential," 2012. http://www.particlesciences.com/news/technical-briefs/2012/overview-of-zeta-potential.html [Accessed: 28/09/2014]

[81] A. Liese and L. Hilterhaus, "Evaluation of immobilized enzymes for industrial applications," *Chem Soc Rev*, vol. 42, no. 15, pp. 6236–6249, 2013.

[82] Malvern Instruments Ltd., "Measuring Zeta Potential - Laser Doppler Electrophoresis." http://www.pct.hu/wsp_images/zetalde.pdf

[83] E. Kissa, *Dispersions: Characterization, Testing, and Measurement*. CRC Press, 1999.

[84] C. Hoo, N. Starostin, P. West, and M. Mecartney, "A comparison of atomic force microscopy (AFM) and dynamic light scattering (DLS) methods to characterize nanoparticle size distributions," *J Nanopart ResJournal of Nanoparticle Research*, vol. 10, no. 1, pp. 89–96, 2008.

[85] W. Goldburg, "Dynamic light scattering," *American Journal of Physics*, vol. 67,

no. 12, pp. 1152–1160, 1999.

[86] Particle Sizing Systems, "Dynamic Light Scattering," San Diego. http://pssnicomp.com/definitions/dynamic-light-scattering/ [Accessed: 28/09/2014]

[87] M. Sartor, "Dynamic Light Scattering to determine the radius of small beads in Brownian motion in solution," University of California, San Diego, Tech. Rep. http://pssnicomp.com/definitions/dynamic-light-scattering/

[88] S. Podzimek, *Light Scattering, Size Exclusion Chromatography and Asymmetic Flow Field Flow Fraction*. John Wiley and Sons, Inc., 2011.

[89] M. Deza and E. Deza, *Encyclopedia of Distances*. Springer Science & Business Media, 2012. http://www.springer.com/new+%26+forthcoming+titles+(default)/book/978-3-642-00234-2

[90] W. Schärtl, *Light scattering from polymer solutions and nanoparticle dispersions*. Springer Berlin Heidelberg, 2007.

[91] H.-H. Perkampus, *UV-VIS spectroscopy and its applications*. Berlin: Springer-Verlag, 1992.

[92] P. Atkins and J. De Paula, *Physikalische Chemie*. Wiley-VCH Verlag GmbH & Co. KGaA, 2006.

[93] M. Hesse, H. Meier, and B. Zeech, *Spektroskopische Methoden in der organischen Chemie*. Georg Thime Verlag Stuttgart, 2005.

[94] M. Sauer, J. Hofkens, and J. Enderlein, *Handbook of Fluorescence Spectroscopy and Imaging*. Wiley-VCH Verlag GmbH & Co. KGaA, 2011.

[95] M. Otto, *Analytische Chemie*. Wiley-VCH Verlag GmbH & Co. KGaA, 2011.

[96] T. H. Gfroerer, "Photoluminescence in Analysis of Surfaces and Interfaces," *Encyclopedia of Analytical Chemistry*, pp. 9209–9231, 2000.

[97] B. Valeur, *Molecular Fluorescence: Principles and Applications*. Wiley-VCH Verlag GmbH, 2001.

[98] J. Lakowicz, *Principles of fluorescence spectroscopy*, 3rd ed. Baltimore: Springer Science+Business Media, LLC, 2006.

[99] T. G. Chasteen, "Jablonski Diagram," 2013. http://www.shsu.edu/ chm_tgc/chemilumdir/JABLON.GIF [Accessed: 28/09/2014]

[100] R. Rottenfusser, E. Wilson, and M. Davidson, "Education in Microscopy and Digital Imaging." http://zeiss-campus.magnet.fsu.edu/articles/basics/fluorescence.html [Accessed: 05/09/2014]

[101] Thermo Spectronic, "Basic UV-Vis Theory, Concepts and Applications," p. 28. http://www.molecularinfo.com/MTM/UV.pdf

[102] G. David, *Analytical Chemistry*. Universities Press, 2001. https://books.google.com/books?id=-dTfQ4m8ZK4C&pgis=1

[103] W. Fester, M. Abramowitz, and M. Davidson, "Olympus IX70 Fluorescence Microscope Cutaway Diagram," 2012. goo.gl/7qzj9O [Accessed: 23/09/2014]

[104] BD Biosciences, *Introduction to Flow Cytometry: A Learning Guide*, Apr. 2000.

[105] H. M. Shapiro, *Practical Flow Cytometry*, 4th ed. John Wiley & Sons, Inc., 2003.

[106] M. G. Ormerod, *Flow Cytometry*, 3rd ed. Oxford University Press Inc., 2008.

[107] K. Vollhardt and N. Schore, *Organische Chemie*, 4th ed. Weinheim: Wiley-VCH, 2005.

[108] J. McDowell, *Encyclopedia of Human Body Systems*. Greenwood, 2010.

[109] N. Lee and T. Hyeon, "Designed synthesis of uniformly sized iron oxide nanoparticles for efficient magnetic resonance imaging contrast agents," *Chem Soc Rev*, vol. 41, no. 7, pp. 2575–2589, 2012.

[110] A. Bizzi and N. D. Stefano, *Clinical MR Spectroscopy: Techniques and Applications*. Cambridge University Press, 2009, vol. 12. https://books.google.com/books?id=gX2hYNyBYJgC&pgis=1

[111] MR Solutions, "Preclinical Imaging," 2014. http://www.mrsolutions.com/applications/preclinical-imaging/ [Accessed: 06/11/14]

[112] J. P. Hornak, "Basics of MRI," 2014. http://www.cis.rit.edu/htbooks/mri/inside.htm [Accessed: 23/09/2014]

[113] T. Le, "High-field, high-performance magnetic resonance: Technical challenges and clinical applications," 2004.

[114] Molecular Imaging Center -Department of Biomedicine, "Bruker Pharmascan 70/16." https://wikihost.uib.no/mriwiki/index.php/Main_Page [Accessed: 06/11/14]

[115] S. Currie, N. Hoggard, I. Craven, M. Hadjivassiliou, and I. Wilkinson, "Understanding MRI: basic MR physics for physicians," *Postgraduate Medical Journal*, pp. 209–223, 2013.

[116] M. Puddephat, "Principles of magnetic resonance imaging," 2014. http://www.mikepuddephat.com/Page/1603/Principles-of-magnetic-resonance-imaging [Accessed: 01/10/2014]

[117] W. Hendee and C. Morgan, "Magnetic resonance imaging. Part I–physical principles." *The Western journal of medicine*, vol. 141, no. 4, pp. 491–500, Oct. 1984.

[118] D. Sen Karaman, T. Gulin-Sarfraz, G. Hedstrom, A. Duchanoy, P. Eklund, and J. Rosenholm, "Rational evaluation of the utilization of PEG-PEI copolymers for the facilitation of silica nanoparticulate systems in biomedical applications," *J Colloid Interface Sci*, vol. 418, pp. 300–310, 2014.

[119] University of Manitoba, "Haemocytometers procedure." http://home.cc.umanitoba.ca/ adam/lab/Haemocytometer.htm [Accessed: 25/11/14]

[120] Culture Collections, "Cell Counting Using a Haemocytometer." https://www.phe-culturecollections.org.uk/technical/ccp/cellcounting.aspx [Accessed: 25/11/14]

[121] K. Lund, E. Stigen, A. Midtveit, E. McCormack, E. Sliden, and B. Haug, "Immuno-conjugate of CytoCy5S; a contrast reagent in nitroreductase directed reporter strategy for in vivo time-domain optical imaging of Immuno-conjugate of CytoCy5S, a contrast reagent in nitroreducatase directed reporter strategy for in vivo time-domain."

Appendix

Variable	Name	Unit
c	Speed of light	$m \cdot s^{-1}$
d	Path length	cm
D	Translational diffusion coefficient	
h	Planck's constant	$6.626 \cdot 10^{-34}$ J· s
R_H	Hydrodynamic radius	m
T	Thermodynamic temperature	273.16 K
ϵ	Dielectric constant	
ϵ	Molar absorptivity coefficient	$L \cdot mol^{-1} \cdot cm^{-1}$
$\triangle$ E	Energy difference	J
ζ	Zeta potential	m·V
η	Viscosity	Pa·s
κ a	Henrys function	
κ	Boltzmann's constant	$1.3806 \cdot 10^{-23}$ J· K^{-1}
λ	Wavelength	m
μ_E	Electrophoretic mobility	V·m
ν	Frequency	s^{-1}

Table 9.1: Table of mathematical variables used throughout this thesis.